Variability of the Mozambique Channel Throughflow

Petra van der Werf

ISBN 978-90-393-5251-9

A digital version of this thesis is available at http://members.casema.nl/p.m.vanderwerf

Institute for Marine and Atmospheric research Utrecht (IMAU)
Faculty of Science, Department of Physics and Astronomy
Utrecht University, The Netherlands

Cover: LOCO mooring buoy with ADCP in the Mozambique Channel

Variability of the Mozambique Channel Throughflow

Variabiliteit van de stroming door het Mozambique Kanaal

(met een samenvatting in het Nederlands)

PROEFSCHRIFT

ter verkrijging van de graad van doctor aan de Universiteit Utrecht
op gezag van de rector magnificus, prof.dr. J.C. Stoof,
ingevolge het besluit van het college voor promoties
in het openbaar te verdedigen op

maandag 18 januari 2010 des middags om 2.30 uur

door

Piety Martha van der Werf

geboren op 19 mei 1981 te Zwolle

Promotoren: **Prof.dr. W. P. M. de Ruijter**
Prof.dr. P. J. van Leeuwen

Dit proefschrift werd mogelijk gemaakt door financiële steun van de Nederlandse organisatie voor Wetenschappelijk Onderzoek (NWO), sectie Aard- en Levenswetenschappen (ALW) onder contract nr. 854.00.016.

Μεταβάλλον ἀναπαύεται.
While changing it rests.[1]

Heraclitus of Ephesus
± 535 – ± 475 BC

[1] Fragment 84a of: Heraclitus, *Fragments, a text and translation with a commentary by T. M. Robinson*, University of Toronto Press, Toronto, 1996

Contents

1

Introduction

1.1 The role of the South West Indian Ocean in the global ocean circulation

It is not that long ago that our knowledge about the circulation of the South West Indian Ocean (SWIO) was rather scarce (see *Lutjeharms*, 2006, for an overview). The ocean was mainly studied to obtain knowledge about the fastest shipping routes and most productive fisheries. Moreover, the oceanographic research was (and still is) mostly carried out by countries in the Northern Hemisphere, as they have the financial resources. As a result, the SWIO generally used to be beyond the reach of oceanographic research. In the 1970s, when the focus of many oceanographers shifted to the understanding of the climate system and the role of the ocean in it, the Indian Ocean with its strong monsoon signal started attracting more attention. It was in this decade that the first estimates of the volume transport through the Mozambique Channel were published (*Duncan*, 1970; *Harris*, 1972). These studies did not give a consistent view of the circulation in and around the Mozambique Channel. Volume transport estimates lay in a huge range, from 5 Sv northward to 26 Sv southward (1 Sv = $10^6\, m^3/s$), partly because they were based on hydrographic data that were taken in different seasons, at different latitudes and that used different depths as reference level (*DiMarco et al.*, 2002). The structure of the flow in the Mozambique Channel was under debate as well. On the one hand, there was the classical view of the circulation with the existence of a continuous southward 'Mozambique Current' flowing along the Mozambican coast (*KNMI*, 1952). On the other hand, others observed large gyres covering the Channel and questioned the concept of a Mozambique Current (*Harris*, 1972;

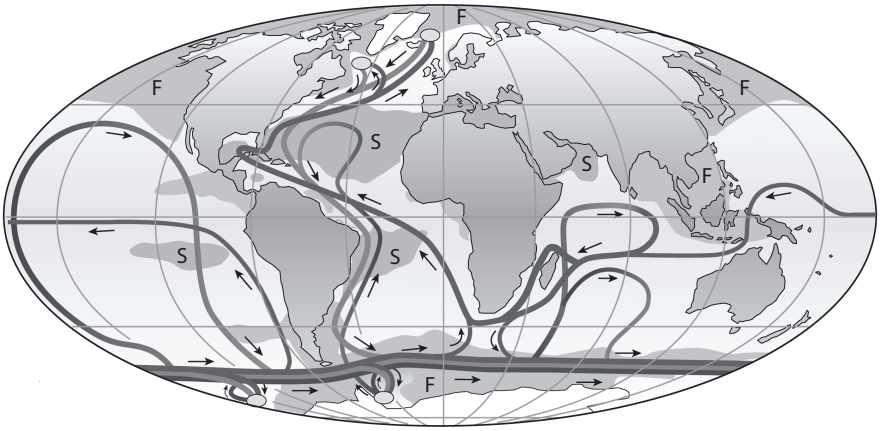

Figure 1.1: *Cartoon of the global ocean overturning circulation. Deep water formation takes place near the poles (ellipses), from where the water spreads out into the deep ocean (lighter lines). Upwelling occurs in the Pacific and Indian Oceans and in the Antarctic Circumpolar Current. Part of the water flows towards the deep water formation areas via the South West Indian Ocean. This surface flow is drawn with the darker lines. Areas where the sea surface salinity is higher (lower) than 36 PSU (34 PSU) are shaded and marked with the letter S (F). This figure was adapted from Rahmstorf (2002).*

Saetre and Jorge da Silva, 1984). Also, there were not enough data to study variability patterns of the flow and water masses.

The poor knowledge of the SWIO was regarded as a problem, because of increasing evidence that the South West Indian Ocean is playing an important role in the global ocean circulation, which in its turn is an important part of the climate system. The global ocean circulation is mainly driven by wind stress and buoyancy forcing. The latter drives the so-called thermohaline circulation (θερμός = warm / hot; ἁλυκός = salty). Oversimplified, surface ocean water is transformed to deep water near the poles, largely in the north Atlantic Ocean, where it has become very dense due to cooling and evaporation. The dense water spreads out in the deep ocean and rises in the Pacific and Indian Ocean and the Antarctic Circumpolar Current due to mixing (*Gordon*, 1986; *Van Aken*, 2007, Figure 1.1). The thermocline and intermediate water flow towards the locations of deep water formation via two paths. The first is the warm water path, via the Indonesian archipelago and around the southern tip of Africa. The second path is called the cold water path, and flows via Drake Passage. The SWIO is thus part of the warm water path in the global ocean circulation and links the Indian Ocean to the Atlantic Ocean. In addition, the South West Indian Ocean is more saline than the South East Atlantic Ocean. A transport

increase of waters from the Indian to the Atlantic Ocean will therefore increase the salinity in the Atlantic, and intensify its overturning circulation (*Gordon*, 1986; *Weijer et al.*, 1999; *Van Sebille and Van Leeuwen*, 2007; *Biastoch et al.*, 2008a).

The transport from the Indian to the Atlantic Ocean is not via a continuous current. Instead, the Agulhas Current, which flows southwestward following the southern African coast, turns almost 180° to return to the Indian Ocean. Four to six times per year, this retroflection occludes and rings with Indian Ocean water are shed into the Atlantic Ocean (*Gordon*, 1985; *Lutjeharms and Van Ballegooyen*, 1988; *Feron et al.*, 1992; *De Ruijter et al.*, 1999; *Biastoch et al.*, 2008b; *Van Sebille et al.*, 2009a). Studies suggest that the shedding of Agulhas rings is controlled upstream. Eddies, coming from the region around Madagascar roughly five times per year, trigger the occlusion of the Agulhas Current (*Van Leeuwen et al.*, 2000; *Schouten et al.*, 2002a). However, the eddies are not a necessary condition to form Agulhas rings, but they do make the formation and path of Agulhas rings more irregular (*Dijkstra and De Ruijter*, 2001b; *Penven et al.*, 2006; *Biastoch et al.*, 2008b). Moreover, in a numerical model, a negative correlation was shown between the Agulhas Current strength and the amount of water flowing from the Indian to the Atlantic Ocean (*Van Sebille et al.*, 2009b).

The understanding of the Agulhas region requires therefore the study of its source areas: the Mozambique Channel throughflow, the East Madagascar Current and a recirculation gyre (*Stramma and Lutjeharms*, 1997; *Feron et al.*, 1998; *De Ruijter et al.*, 1999). Since 2000, a Dutch research program is dedicated to observe the Mozambique Channel transport: the Long-term Ocean Climate Observations (LOCO) program (*Ridderinkhof and De Ruijter*, 2003). In this project, an array of moored current, salinity and temperature meters has been placed in the Mozambique Channel at its narrowest section (around 17°S; its location is shown as the white line in Figure 1.3). The Mozambique Channel was chosen because it is relatively easier to measure the flow through a channel than in an unbounded current. Also, it was suspected that the Mozambique Channel throughflow had more influence on the global circulation as it transports tropical water to subtropical regions (*Ganachaud et al.*, 2000). The program started with a 19-months pilot project in 2000 – 2001. Since November 2003, the mooring array has been operational continuously, and has yielded a lot of data. In this dissertation, this data is used as a starting point to study the Mozambique Channel throughflow. In line with the above, focus will be on flow and water mass variability, as they influence the characteristics of the interocean exchange. The main questions of the dissertation are:

What is the spectrum of variability of the Mozambique Channel throughflow in the range from eddy to interannual time scales? And what is the origin of this variability?

In recent years, quite some knowledge has been gathered of the SWIO and the Mozambique Channel, which is used as a base for the dissertation. In the next sections, an overview will be given on the time-mean circulation of the Indian Ocean and on the variations to this mean. Finally, the outline of this dissertation is presented.

1.2 The general circulation of the Southern Indian Ocean

An overview of the bathymetry of the Southern Indian Ocean is sketched in Figure 1.2. Three important ridges divide the basin. They influence the direction of currents in the ocean, as water has to flow through gaps in the ridges. Also, they block barotropic signals travelling from east to west. In the west lies the Madagascar Ridge, which consists of the island Madagascar and a plateau to the south. The Mascarene Ridge is found northeast of Madagascar. Part of this ridge are islands such as Reunion, Mauritius and the Seychelles archipelago. The easternmost ridge, the Ninety East Ridge, has an almost meridional orientation. The Mozambique Channel is the body of water between Madagascar and Mozambique, Africa. At its narrowest section, it is about 350 km wide and 2.7 km deep. In the Channel, small islands are found, such as the Comoros island group in the north and the island Juan de Nova close to the LOCO section.

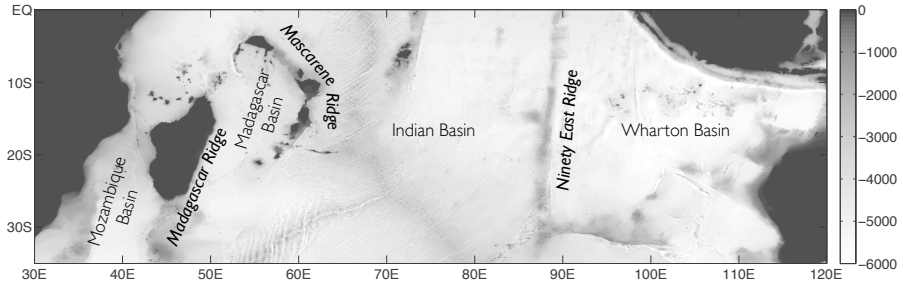

Figure 1.2: *Bathymetry of the Southern Indian Ocean in meters, with the main basins and ridges.*

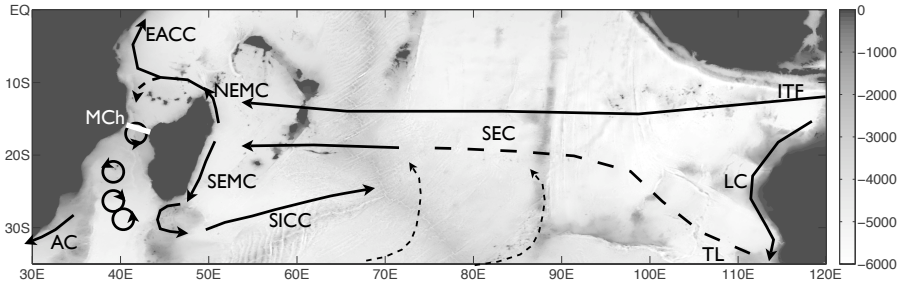

Figure 1.3: *Main currents of the Southern Indian Ocean: Indonesian Throughflow (ITF), Leeuwin Current (LC), Tasman Leakage (TL), South Equatorial Current (SEC), Northeast and Southeast Madagascar Currents (NEMC and SEMC), East African Countercurrent (EACC), South Indian Ocean Countercurrent (SICC) and Agulhas Current (AC). The Mozambique Channel (MCh) and the LOCO mooring section are drawn in white. The circulation in the Mozambique Channel is dominated by anticyclonic eddies, while at the southern tip of Madagascar, dipoles are formed.*

The main flow of water towards Madagascar and the Mozambique Channel is the South Equatorial Current (SEC, Figure 1.3), which has an estimated volume transport of 39 Sv (*Schott et al.*, 1988a) and separates the tropical from the subtropical gyre. The SEC is fed by four important sources (see *Schott et al.*, 2009, for an overview): the tropical and subtropical gyres, the Indonesian Throughflow (ITF) and the Tasman Leakage (*Speich et al.*, 2001, 2007). The ITF connects the tropical Pacific Ocean with the tropical Indian Ocean and is characterized by relatively fresh waters. Its characteristics have been found far into the Indian Ocean, up to the waters around Madagascar (*Gordon et al.*, 1997; *You and Tomczak*, 1993; *You*, 1997; *Gordon et al.*, 1999; *Song et al.*, 2004; *Talley and Sprintall*, 2005; *Valsala and Ikeda*, 2007). The ITF transport is estimated to be 15 Sv $\pm$ 4 Sv (*Sprintall et al.*, 2009).

In addition to this almost horizontal circulation, a meridional overturning circulation exists in the Indian Ocean basin (*Ganachaud et al.*, 2000; *Karstensen and Tomczak*, 1997; *Karstensen and Quadfasel*, 2002a; *Schott et al.*, 2002; *Lee*, 2004; *Schott*, 2005). Two overturning cells can be distinguished, of which one is confined to the southern hemisphere and the other crosses the equator. For both cells, subduction occurs dominantly in the southeastern subtropical Indian Ocean. Upwelling takes place off the coast of Somalia and Arabia for the cross-equatorial cell, and in the 'upwelling dome' for the southern cell. The upwelling dome is a region northeast of Madagascar ($5° - 12°$S and $50° - 70°$E, *Murtugudde et al.*, 1999), in which the upwelling is driven by the curl of Southeast trade winds. The mean strength of the southern cell is about 8 Sv (*Lee*, 2004).

The SEC impinges upon the island between 10°S and 20°S and bifurcates into the Northeast and Southeast Madagascar Current (NEMC and SEMC, respectively). The southward transport in the SEMC was estimated to be 21 Sv at 23°S (*Schott et al.*, 1988a; *Swallow et al.*, 1988) and 32 Sv at 25°S (*Nauw et al.*, 2008). South of Madagascar, this current partly retroflects. There is debate about its connection to the South Indian Ocean Counter Current (SICC *Palastanga et al.*, 2007; *Siedler et al.*, 2006), as the water mass characteristics of the SEMC and SICC are not compatible (*Nauw et al.*, 2008). At the retroflection, eddies and dipoles are shedded that propagate towards the African coast (*De Ruijter et al.*, 2004; *Quartly and Srokosz*, 2004).

The NEMC (30 Sv, *Schott et al.*, 1988a; *Swallow et al.*, 1988) rounds the northern tip of Madagascar and bifurcates again at the African coast. The waters that flow through the Mozambique Channel meet with the waters from the SEMC and join into the Agulhas Current.

A first estimation of the transport through the Mozambique Channel based on a Sverdrup model is about 10 – 15 Sv (*Godfrey*, 1989). Transport estimates by using hydrographic measurements of the Mozambique Channel range from 5 Sv northward to 26 Sv southward (*DiMarco et al.*, 2002). This large range is partly due to the different locations of the measurements and different assumptions about the level of no motion. But as hydrographic measurements are snapshots in time, this range also indicates that the transport time series has a large variability.

Two estimates of the mean transport were obtained by the LOCO project: 14 Sv southward in the pilot project (April 2000 to November 2001, *Ridderinkhof and De Ruijter*, 2003) and 8.6 Sv southward for the period November 2003 – February 2006 (*Harlander et al.*, 2009). The continuous measurements confirmed the high variability of the transport in the Mozambique Channel (section 1.3).

The flow pattern of the Mozambique Channel is neither a continuous Mozambique Current nor a pattern of steady anticyclonic gyres filling the Channel. Instead, a train of anticyclonic eddies was observed propagating southward (*De Ruijter et al.*, 2002; *Schouten et al.*, 2003). This reflects also on the mean velocity profile at the LOCO section (Figure 1.4). At the upper west corner the mean flow is strongly southward, whereas at the upper east corner, the mean velocity is northward but weaker. These two cores are interpreted as the combination of southward propagating eddies with a non-continuous western boundary current (*Harlander et al.*, 2009).

At the African continental slope, an undercurrent flows northward (*De Ruijter et al.*, 2002; *Ridderinkhof and De Ruijter*, 2003; *Harlander et al.*, 2009). It has cores around 1500 m and 2500 m depth (these are not visible in Figure

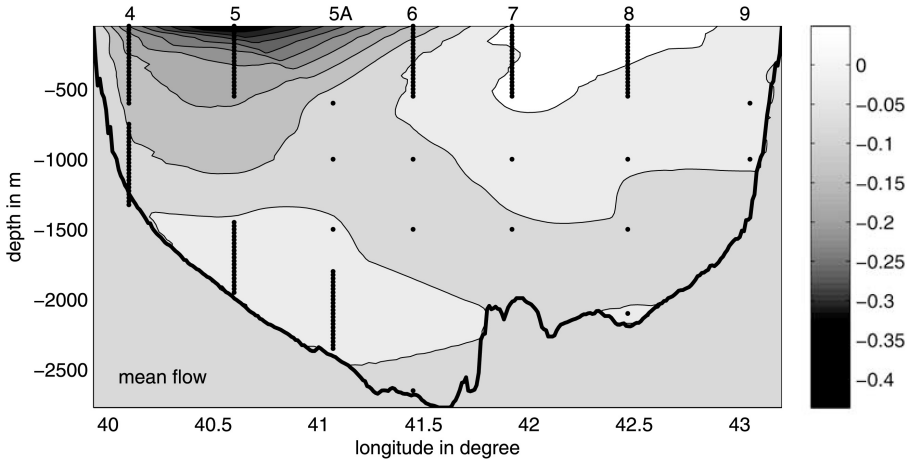

Figure 1.4: *Mean velocity measured at the LOCO section for the period November 2003 to February 2006. Contours are drawn every 5 cm/s, darker colors mean southward flow. The dots and lines represent the locations of the velocity measurements. From: Harlander et al. (2009).*

1.4) and a mean velocity of 5 cm/s. *Ridderinkhof and De Ruijter* (2003) suggested that this current might be a continuation from the Agulhas Undercurrent (*Beal and Bryden*, 1997), bringing deep waters from the Atlantic Ocean to the SWIO. However, studies to water mass characteristics and numerical models found that the connection between the Agulhas Undercurrent and the undercurrent found in the Mozambique Channel is probably very weak (*Van Aken et al.*, 2004; *Biastoch et al.*, 2009).

1.3 Variability at a range of time scales

The previous section showed that the transport through the Mozambique Channel is highly variable and that eddies and dipoles have been observed in the Mozambique Channel and near the southern tip of Madagascar. In this section, this variability will be discussed in more detail, and a connection to the large-scale ocean circulation will be made.

Many aspects of the variability in the Southern Indian Ocean are visible in Figure 1.5. A clear path of high sea surface height variability leads from the Mozambique Channel and the Southeast Madagascar Current into the Agulhas Current. This pattern largely originates from propagating eddies and dipoles. Approximately four to six eddies per year propagate through the LOCO section (*Schouten et al.*, 2003; *Ridderinkhof and De Ruijter*, 2003) and 3–4 dipoles per year are shed south of Madagascar (*De Ruijter et al.*, 2004). Next, two

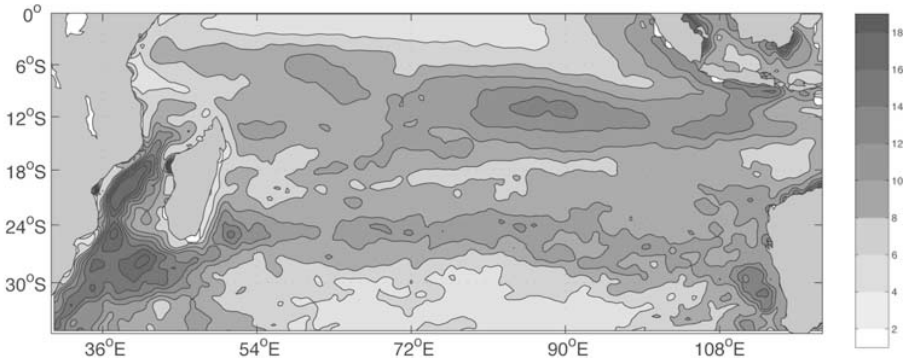

Figure 1.5: *Root mean square of the sea surface height variability from weekly data of satellite altimetry in the period October 1992 to January 2004. Units are in cm. East of Madagascar, two zonal bands of enhanced variability are visible at* $8° - 12°S$ *and* $24°S$*. From: Palastanga et al. (2007).*

zonal bands of enhanced variability are visible east of Madagascar leading from the west coast of Australia and Java/Sumatra towards Madagascar. Also in these bands, intra-annual variability has been observed (*Schouten et al.*, 2002b; *Palastanga et al.*, 2007; *Zhou et al.*, 2008). In addition, interannual signals have been found to propagate via the northern band towards the Mozambique Channel (*Schouten et al.*, 2002b; *Palastanga et al.*, 2006). Patterns of sea surface height variability on the seasonal time scale have also been observed in the Indian Ocean (e.g. *Matano et al.*, 2008), but their signal is too weak to be visible in Figure 1.5.

Often in this dissertation, variability is studied by filtering the time series in the frequency domain. In this way, the processes that we choose to study are isolated from processes at other time scales. In this section, the variability is therefore discussed in the three frequency bands used, starting with higher frequency variability at eddy time scales, then discussing time scales larger than a year and ending at the seasonal time scale.

1.3.1 Intra-annual variability

The most important coherent structures on the intra-annual time scale in the Mozambique Channel are anticyclonic eddies. Mozambique Channel eddies propagate through the LOCO mooring section four to six times per year (*Schouten et al.*, 2003; *Harlander et al.*, 2009). One of the first well-documented eddies (*De Ruijter et al.*, 2002) is shown in Figure 1.6. This eddy occupies almost the entire section, both in width and in depth. It has a strong barotropic component, reaching speeds of 10 cm/s close to the bottom. *Ridderinkhof and*

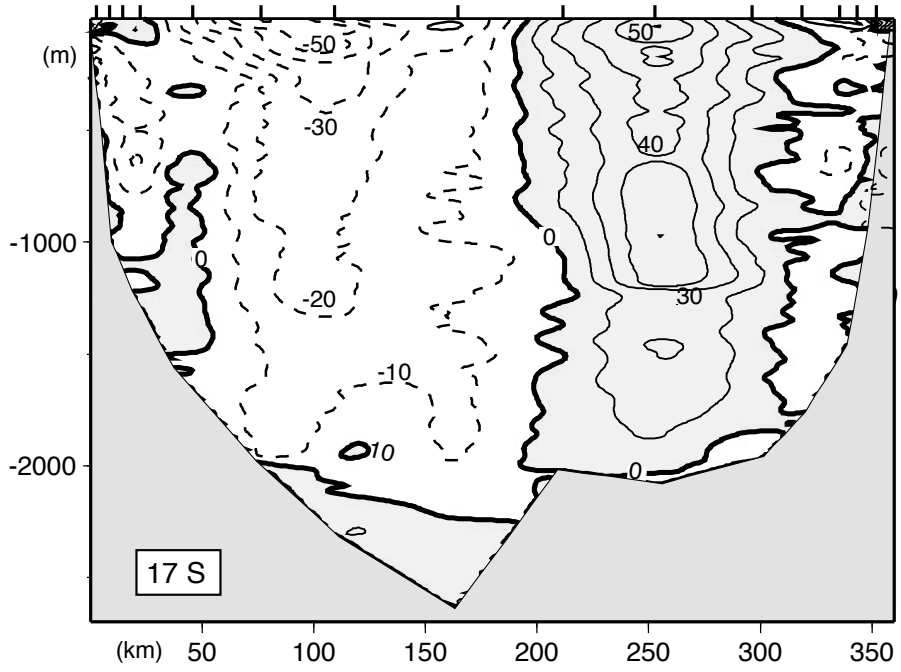

Figure 1.6: *An anticyclonic eddy, measured by a Lowered Acoustic Doppler Current Profiler (LADCP) at 17°S in the Mozambique Channel. Shown are the meridional velocities (cm/s). Positive values denote northward flow. From: De Ruijter et al. (2002).*

De Ruijter (2003) and *Harlander et al.* (2009) suggested that the eddies are formed close to the narrowest section of the Mozambique Channel (near the LOCO transect). They described the following sequence of events around their formation. Prior to the development of an eddy, a strong southward current is observed at the eastern side of the Channel. This current is moving westward, which is interpreted as part of a Rossby normal mode, becomes unstable and an anticyclone develops. The eddy then migrates southward.

The dominant frequency of the sea surface height variability decreases southward in the Mozambique Channel (*Schouten et al.*, 2003). At the northern entrance of the Mozambique Channel, the dominant mode has a frequency of 7 per year, which decreases to 4–6 per year near the LOCO section and 4 per year south of Madagascar. *Schouten et al.* (2003) observed that the frequency decreases due to the dissipating and merging of eddies, which they relate to Rossby waves coming in from the east.

Rossby waves thus play an important role in the variability in the Mozambique Channel, as they affect the formation of eddies and their reduction in frequency. Rossby waves reach the island from upstream via the two latitudinal bands of enhanced sea surface height variability (Figure 1.5).

Schouten et al. (2002b) suggested that the northern band originates from monsoonal variability in the Equatorial Indian Ocean. During the transitions between the monsoons, monsoonal winds force strong semi-annual equatorial Kelvin waves (*Wyrtki*, 1973). Upon reaching Sumatra, part of the energy of this signal doubles in frequency (*Cane and Moore*, 1981). The four per year signal might also be resonant for the sub-basin in between the Indonesian archipelago and the Maldives island chain (*Schouten et al.*, 2002b). The signal then splits into a north- and southward propagating coastal Kelvin wave. The southward propagating coastal Kelvin wave emits Rossby waves that propagate via the northern band towards Madagascar with a four-per-year frequency. In 1994 and 1997–1998, this 'teleconnection' was disrupted. The cause of these interannual fluctuations in variability will be discussed later.

Zhou et al. (2008) studied the northern variability band in a numerical model. In contrast to *Schouten et al.* (2002b), they related the variability to baroclinic instability. The waves of the South Equatorial Current in their study had periods of 40–80 days (4.5 – 9 times per year) and wavelengths of 650 km. These oscillations were stronger in boreal winter and spring. The different estimates of the mean frequency in the northern band by *Schouten et al.* (2002b) and *Zhou et al.* (2008) may lie in the filtering techniques used by *Schouten et al.* (2002b) and the model used by *Zhou et al.* (2008).

In the southern band, waves with dominant frequencies of 3.5 – 6 times per year and wavelengths of 290–470 km were observed (*Palastanga et al.*, 2007).

This Rossby wave variability is generated locally in the Subtropical Indian Ocean, by baroclinic instability between the westward flowing SEC and the overlying eastward flowing SICC.

Upon reaching Madagascar, the energy of the variability in the two bands is converted to a coastal Kelvin wave that encircles the island. In the Mozambique Channel, this energy is then shedded as a Rossby wave (a mechanism described by *Liu et al.*, 1999a,b).

In addition to the intra-annual variability coming from upstream, *Harlander et al.* (2009) also noted that the Rossby normal modes at the LOCO section have a five-per-year frequency. They deduced this both from a Principal Oscillation Pattern analysis and from a quasi-geostrophic channel model.

Another mechanism for high frequency variability in the Mozambique Channel originates from the northern tip of Madagascar. Measurements from *Swallow et al.* (1988) showed a very strong shear of the flow at a section perpendicular to the coast. This flow becomes unstable and an oscillation arises with a period of 50 days and a wavelength of 400 km (*Quadfasel and Swallow*, 1986). *Quadfasel and Swallow* (1986) interpreted these oscillations as a barotropic Rossby wave. In numerical models (*Biastoch and Krauss*, 1999; *LaCasce and Isachsen*, 2007) this instability was found to produce eddies in the northern Mozambique Channel.

1.3.2 Interannual variability

Interannual variability is less observed, due to the short length of many time series. Nevertheless, some variability patterns have been identified. Also, trends have been observed, that may be identified as part of an oscillation in a longer time series.

As remarked in the previous section, the intra-annual variability in the northern band has fluctuations on interannual time scales. In 1994 and 1997–1998, large events of the Indian Ocean Dipole and El Niño led to a disruption of the variability in the northern band and thereby to less Mozambique Channel eddies (*Schouten et al.*, 2002b). *Palastanga et al.* (2006) found a similar relation between the Indian Ocean Dipole and the eddy kinetic energy in the Mozambique Channel.

The Indian Ocean Dipole (IOD, also named the Indian Ocean Zonal Mode, *Saji et al.*, 1999; *Webster et al.*, 1999), is most often diagnosed by the IOD index, which is the difference in sea surface temperature anomaly between a box in the western tropical Indian Ocean ($50° - 70°$E; $10°S - 10°$N) and the eastern tropical Indian Ocean ($90° - 110°$E; $10°$S – EQ). When the IOD index exceeds (is less than) the (negative) standard deviation of the index time series, the

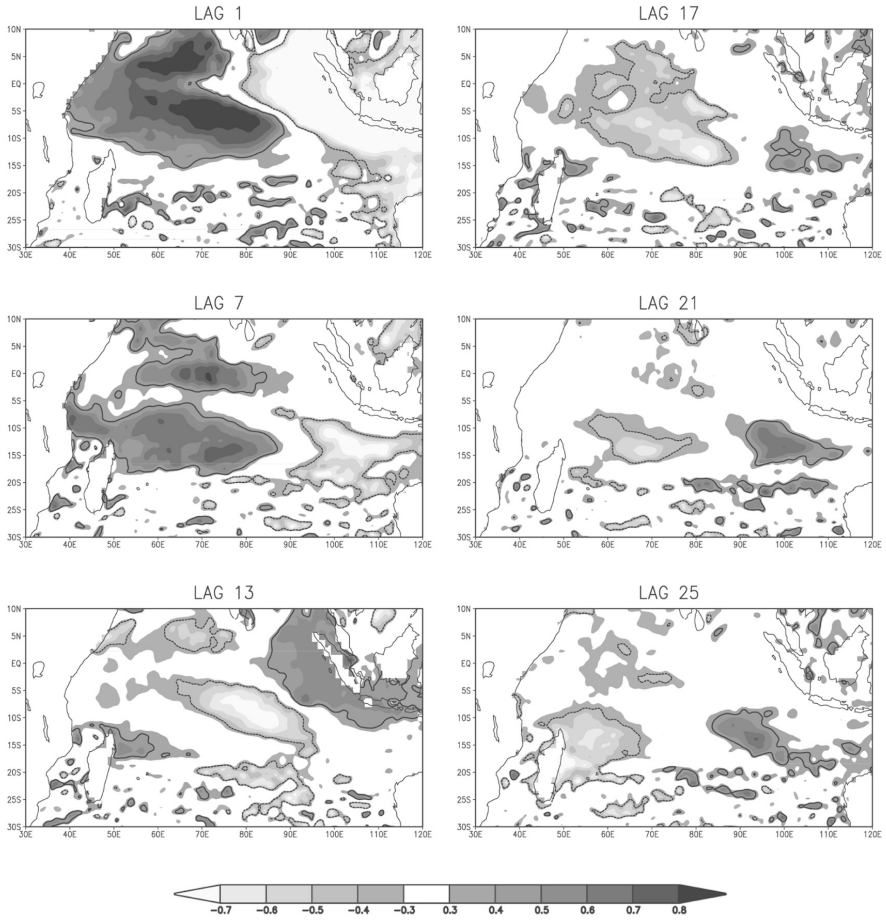

Figure 1.7: *Correlation patterns between the IOD index and sea surface height (SSH) fields. The SSH was obtained from satellite altimetry and low-pass filtered with a cutoff frequency of 8 months. In each frame, the correlation of each point of SSH with the IOD index was calculated with the SSH lagging the IOD index by the number of months above the frame. The contour denotes the areas which are significantly correlated at the 90% confidence level. The pattern in the panel with LAG 1 thus shows the SSH pattern associated with a positive IOD event: a positive anomaly in the western tropical Indian Ocean and a negative anomaly in the east. This pattern moves southward and the positive anomaly interacts with the island (LAG 7 and LAG 13). Meanwhile, the negative phase of the IOD evolves in the tropics (a negative SSH anomaly in the west and a positive anomaly near Indonesia). From: Palastanga et al. (2006).*

IOD is in a positive (negative) phase. In a positive IOD phase, the sea surface temperature in the western tropical Indian Ocean is thus higher than normal, while in the eastern tropical Indian Ocean it is lower than normal. Atmospheric convection over these regions causes an anomalous westward wind over the tropical ocean. This leads to an increase (decrease) of the sea surface height in the west (east) (panel 1 of Figure 1.7) and the downwelling (upwelling) of the thermocline, resulting in the increase of the sea surface temperature anomalies. The anomalous sea surface height also affects local currents (*Palastanga et al.*, 2006; *Horii et al.*, 2008; *Masumoto et al.*, 2008). In the negative phase, a similar sequence of events occurs. The IOD was found to be quasi-biennial, due to wave dynamics and the interplay with the subsurface layers (*Rao et al.*, 2002). However, recently, the IOD was in a positive phase three years in a row (2006 – 2008, *Vinayachandran et al.*, 2007; *Behera et al.*, 2008; *Horii et al.*, 2008; *Cai et al.*, 2009).

Palastanga et al. (2006) studied the relation of the IOD and the circulation in the Mozambique Channel in more detail. They showed that the sea surface height pattern related to the IOD propagates southwestward (Figure 1.7, see also *Rao et al.*, 2002), and reaches the island after approximately six months. At the same time, the strength of the SEC is reduced, and therefore less water flows towards Madagascar. Also, they found a positive correlation between the IOD index and the eddy kinetic energy in the Mozambique Channel. At a lag of approximately a year, the correlation of the sea surface height with the IOD index is opposite to the correlation with zero lag (Figure 1.7, LAG 1 and LAG13), but this is probably caused by the quasi-biennial nature of the IOD.

A similar dipole pattern originates in the Pacific Ocean: the El Niño / Southern Oscillation (ENSO). A positive ENSO (*El Niño*) results in less inflow of the ITF (*Gordon et al.*, 1999). In addition, the ITF water during a positive ENSO is colder (*Susanto et al.*, 2001; *Vranes et al.*, 2002) and saltier due to less rainfall in the Indonesian region (*Phillips et al.*, 2005). A negative ENSO (*La Niña*) triggers the opposite. Also, ENSO influences the atmospheric conditions over the Indian Ocean (*Reason et al.*, 2000).

The interaction between the IOD and ENSO is still unclear (see e.g. *Drbohlav et al.*, 2007; *Feng and Meyers*, 2003; *Meyers et al.*, 2007; *Yamanaka et al.*, 2009). In general, a positive (negative) phase of one of the dipoles coincides with a neutral or positive (negative) phase of the other (over the last century, the only two exceptions were in 1930 (*Meyers et al.*, 2007) and in 2007 (*Behera et al.*, 2008)).

Many studies indicate trends in the Indian Ocean over the last decades. At least two of these trends are important for the Mozambique Channel. *Bryden et al.* (2003) and *McDonagh et al.* (2005) reported on a salinity fluctuation in

the subtropical gyre. At 32°S, they observed a freshening in the upper thermocline between 1965 and 1987 and a salinity increase afterwards. In contrast, the salinity decreased in the lower thermocline over the whole observational period (1936–2002). As the study was based on only a few time slots, it is not possible to draw any more conclusions on the properties of the oscillation.

Secondly, a trend has been observed in the meridional overturning circulation of the Southern Indian Ocean. *Lee* (2004) and *Lee and McPhaden* (2008) derived from satellite altimetry and wind products that both overturning cells decreased in strength from 1992 to 2000 and strengthened from 2000 to 2006. This was partly confirmed by *Karstensen and Quadfasel* (2001, 2002b), who found an increase of the subtropical water masses above the thermocline from 1965 to 2000.

1.3.3 Seasonal variability

The seasonal variability of the ocean is caused by the seasonal cycle of the atmosphere. In the austral winter (July – August), the intertropical convergence zone is shifted to the north, and as a result, the SEC flows slightly north of its mean latitude. Similarly, in the austral summer (January – February), the intertropical convergence zone and the SEC are shifted somewhat southward. These latitudinal oscillations of the wind stress and the SEC are most probably influencing the volume transport through the Mozambique Channel. *Matano et al.* (2002, 2008) have shown by analyzing a numerical model and satellite data, that the seasonal cycle induced by wind forcing is mainly barotropic, and can not cross the ridges in the basin. The variance of the transport in the Mozambique Channel should therefore be caused by wind stress variations west of the Mascarene Ridge (Figure 1.2).

In numerical models, a yearly cycle in the volume transport is indeed simulated (*Biastoch et al.*, 1999; *Matano et al.*, 2002). However, no clear seasonal cycle has been observed in observations (*Swallow et al.*, 1988; *Schott et al.*, 1988a; *Ridderinkhof and De Ruijter*, 2003; *Schouten et al.*, 2003). *Schouten et al.* (2005) did describe a seasonal variation in the northern part of the Mozambique Channel, which is characterized by an oscillation of the main water source between the tropical and subtropical gyre.

1.4 Outline of the dissertation

As the lengths of the observational time series increase, more information on the variabililty in the Mozambique Channel becomes available. It has become clear from the above overview, that some data records for periods longer than a year

have already been available, but these are mostly from satellite observations, giving only insight in variability at the ocean surface, or obtained from numerical model simulations. In the LOCO data on the other hand, observations are available at depth. LOCO therefore provides information on variability in volume fluxes, and subsurface temperature and salinity fluctuations. It therefore serves also a good data set for the validation of variability in numerical models. For that reason, they are the starting-point of this study. The data record used starts in November 2003 and ends in January 2008. This 4.2-year time series is just long enough to study the variability of the Mozambique Channel at the range from eddy to biennial time scales.

In the next chapter, the velocity measurements of the LOCO project will be introduced. The mooring layout will be shortly presented, as well as the data treatment. Next, the Mozambique Channel volume transport time series, which is used in this and other chapters, will be derived. The second part of the chapter deals with one of the striking features of the transport time series: some large variations at interannual time scales. These variations will be shown to be a superposition of variability at the seasonal and biennial time scale and their origin is sought upstream. Could the quasi-biennial variance of the IOD index be related to the biennial variability of the volume transport?

In Chapter 3, the transport time series will be used to validate several ocean general circulation models. It addresses the discrepancy between the numerical models and the observations that was mentioned earlier in section 1.3.3: the seasonal cycle is dominant in the transport time series of numerical models, while in observations it is not. It is important to understand this discrepancy, as observational data is still sparse and numerical model data is often used by oceanographers to fill in its gaps. It will be shown in the chapter, that the main discrepancy lies in the underrepresentation of the intra-annual variability by the models. This variability overshadows the seasonal cycle in the observations. The focus of the chapter therefore is on the simulation of variability at the eddy time scale in the numerical models and on the question why this variability is underrepresented.

In addition to the interannual variability of the LOCO volume transport time series, interannual variations have also been observed in the water mass characteristics. From hydrographic measurements in the pilot project (in the years 2000 and 2001), the waters at the LOCO section in the Mozambique Channel between 50 m and 200 m depth were found to be much more saline than recorded in the continuous and hydrographic measurements from 2003 to 2008. In Chapter 4, this salinity anomaly is studied and traced back to variability in the Indian Ocean basin. For this, three ocean general circulation models are used that simulate a similar salinity anomaly.

In Chapter 5, the question is addressed whether variability of the circulation around Madagascar and in the Indian Ocean basin influences the mean state of the Mozambique Channel throughflow. The underrepresentation of variability might then explain the large variety of mean transport estimates of eddy-permitting and lower resolution Ocean General Circulation Models. In the study, a simple setup of the SWIO is used together with a hierarchy of four different models, ranging from a linear steady state model to a baroclinic time integration model. In Chapter 5, it is shown that the estimates of the time-mean channel transport in these models are indeed very different. Is the rectification of variability its main cause?

In the final chapter, the main results of the dissertation are summarized. Also, some of the main issues that are in need of further study are addressed. These are questions that will arise in the forthcoming chapters, as well as questions that put the results of these studies in a more global context.

2

Seasonal and Interannual Variability in the Mozambique Channel from Moored Current Observations

Direct observations from an array of current meter moorings across the Mozambique Channel in the Southwest Indian Ocean are presented, covering a period of more than four years. This allows an analysis of the volume transport through the Channel, including the variability on interannual and seasonal time scales. The mean volume transport over the entire observational period is 16.7 Sv in the poleward direction. Seasonal variations have a magnitude of 4.1 Sv and can be explained from the variability in the wind field over the western part of the Indian Ocean. Interannual variability has a magnitude of 8.9 Sv and is large compared to the mean. This time scale of variability could be related to variability in the Indian Ocean Dipole, showing that it forms part of the variability in the ocean-climate system of the entire Indian Ocean. The relatively strong interannual variability stresses the importance of these long-term direct observations.

This chapter is based on:
Ridderinkhof, H., P. M. Van der Werf, J. Ullgren, P. J. Van Leeuwen, H. M. Van Aken, and W. P. M. De Ruijter, Seasonal and interannual variability in the Mozambique Channel from moored current observations, *J. Geophys. Res. submitted*, 2009.

2.1 Introduction

Long-term direct observations on ocean currents that span more than 1–2 years are scarce. This holds even more for direct observations on parts or branches of ocean gyres or the global overturning circulation when a large number of deep sea moorings and instruments is needed to obtain reliable information over an ocean region rather than from a single location. Examples of such observational studies in the world oceans are those of the Florida Current (*Schott et al.*, 1988b), Kuroshio (*Johns et al.*, 2001), Yucatan Channel (*Sheinbaum et al.*, 2002) and the Atlantic meridional overturning circulation (*Cunningham et al.*, 2007). The reason behind the scarceness of this type of observations is obvious: the costs in terms of manpower, shiptime, instrumentation etc. is relatively large and the risk of failure is serious. By far, most of the studies on variability in ocean currents therefore rely on the application of numerical models. Observational studies on long-term variability in ocean currents mostly use indirect methods, like analyzing variability in ocean tracers or, more recently, on long-term satellite observations of the sea surface height (e.g. *Nauw et al.*, 2008).

The measurements in the Mozambique Channel that are used in this study are therefore very special. The observations started late 2003 and form a follow-up of a pilot experiment in the area that was conducted with a current meter mooring array in 2000 – 2001. This pilot project (*Ridderinkhof and De Ruijter*, 2003) showed that the flow through the Mozambique Channel (MCh) is an important part of the greater Agulhas system and forms the connection between the tropical regions and the Agulhas current and thereby of the large scale circulation in the Southern Indian Ocean. The time-variability of the net flow through the Channel appeared to be large and, due to undersampling and problems in data return, estimates on the volume transport through the Channel could be done only approximately. These estimates (for one year of observations only) showed that the volume transport oscillates remarkably regularly with values varying roughly between 20 Sv northward and 60 Sv southward and a mean value of some 14 Sv southward, which falls in the rather wide range of previous estimates that were based on hydrographic snapshots, derived indirectly or based on global ocean model simulations (*DiMarco et al.*, 2002; *Stammer et al.*, 2003; *Maltrud and McClean*, 2005). Another important finding was that North Atlantic Deep Water (NADW) is present at the section, with its core hugged against the continental slope of the African continent. The volume transport of NADW was estimated to be about 2 Sv (*Van Aken et al.*, 2004).

These observations, together with the long-term interest in this ocean area

of the NIOZ and IMAU (see e.g. *De Ruijter et al.*, 1999, 2005) were motivations to setup the LOCO (Long-term Ocean Climate Observations) program, in which a mooring array has been placed in the narrows of the MCh in the end of 2003. Since then, servicing and redeploying of these moorings combined with a hydrographic survey along the section has been done every 1.5–2 years. The final recovery of the moorings is now planned in 2011. Fortunately, thus far, the technical performance of the moorings and instruments has been excellent, with only very few instrument failures (*Ridderinkhof*, 2005; *Ridderinkhof and Quartly*, 2006; *Ridderinkhof*, 2008).

First analyses of the mooring data for the period end 2003 – early 2006 (a period of 2.3 years) have been presented by *Harlander et al.* (2009). The focus was on quantifying and analyzing the variability in the currents and volume transport at the frequency of five to six per year since the currents with frequencies at this part of the spectrum appeared to dominate the temporal variability in the currents and volume transport. Applying simplified models, it was made plausible that this frequency corresponds to the frequency of a Rossby wave channel mode. Moreover, the formation or passage of eddies at the location of the mooring array appeared to occur at the same frequency suggesting a strong relation between the Rossby waves and the formation of eddies although the precise mechanism leading to the formation of these eddies could not be deduced from the observations. Also, other possible causes are given of the 5/y eddy frequency, such as an oceanic connection to the equatorial region (*Schouten et al.*, 2002b; *Palastanga et al.*, 2006; *Zhou et al.*, 2008) or baroclinic instability of the South Indian Ocean Countercurrent (SICC, *Palastanga et al.*, 2007) that propagates westward around 24°S.

In this chapter, observations from the same mooring array are presented; now from the period end 2003 – early 2008. Thus, as compared to *Harlander et al.* (2009), one additional period of about 2 years is available that nearly doubles the total length. As the data recovery of this last period was very successful, this data could be used to fill gaps and data losses of the other two periods. A summary of the data treatment will be presented in the first part of this chapter (for a full coverage of this subject, see the paper of *Ridderinkhof et al.*, 2009).

As the observations are now covering more than 4 years, it is possible to study variability at longer time scales than in previous studies. Therefore, in analyzing the results, focus is on variability at seasonal and longer (interannual) time scales. Previous studies (*De Ruijter et al.*, 2005) have shown that variability in the ocean circulation at these time scales is most presumably coupled to variability in the entire Indian Ocean. Moreover, *Schott et al.* (2009) have recently shown that the influence of the Indian Ocean on climate variability

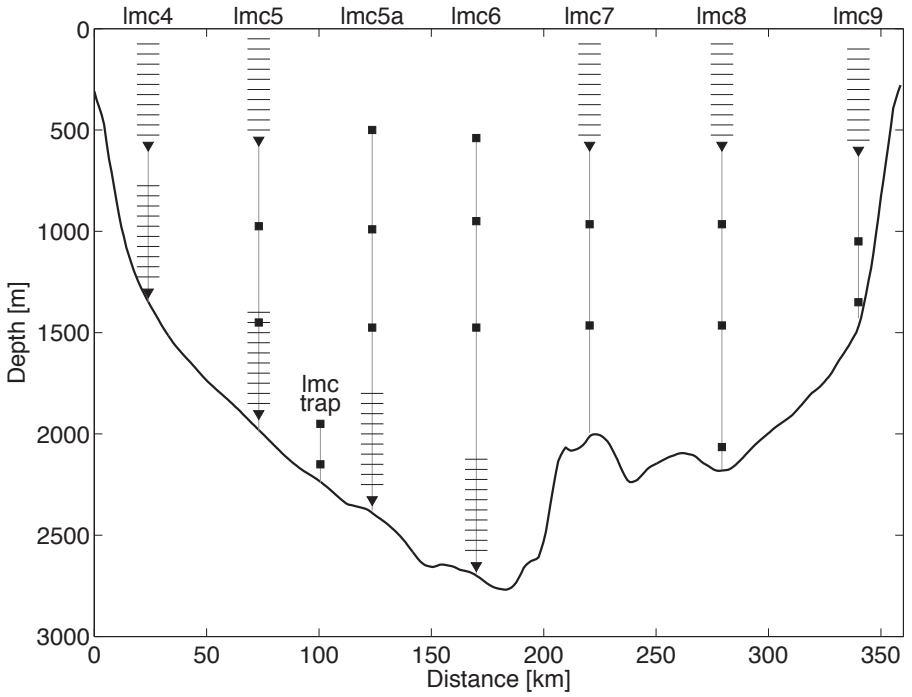

Figure 2.1: *Design positions of current meters (squares) and ADCPs (triangles; profiling range marked by horizontal stripes). Due to instrument failures the positions of instruments returning data may differ slightly (see text for details).*

may be much stronger than previously thought, thereby expressing the importance of knowledge on the variability of the ocean circulation on these time scales. The long-term variability in the volume transport is discussed in the remainder of the chapter where this variability is related to possible large scale sources of variability in the Indian Ocean like the wind field, the Indian Ocean Dipole (IOD) and the input from the Indonesian Throughflow.

2.2 Data

2.2.1 Velocity measurements from the mooring array

The array of seven long current meter moorings plus one short sediment trap mooring has been maintained across the narrowest part of the Mozambique Channel, around 17°S, since November 2003 (Figure 1.3). The moorings were serviced and redeployed three times: in March 2005, March 2006, and January 2008. The velocity measurements described in this dissertation span the first

three deployment periods, i.e., between November 2003 and January 2008.

The mooring array was designed with upward looking Acoustic Doppler Current Profilers (ADCPs) across the Channel measuring currents in the upper 500 m (Figure 2.1), the depth range in which the flow is strongest. Moorings on the western side of the Channel were also equipped with ADCPs near the bottom, in order to capture the northward flowing Mozambique Undercurrent (*De Ruijter et al.*, 2002; *Ridderinkhof and De Ruijter*, 2003). At intermediate depths and in the deep water on the eastern side of the Channel, Recording Current Meters (RCMs) provide point measurements of current velocity at the 1000 m and 1500 m depth levels. The velocity meters (RCMs and ADCPs) were set to tide resolving sampling rates of 20 and 30 minutes. Conductivity-Temperature-Depth (CTD) sensors were also distributed along the mooring lines at intermediate depths, and will be discussed in Chapter 4.

Not all instruments were working properly during the three deployment periods, resulting in gaps in the data record with respect to the designed array. During the first deployment period, the upper ADCP at mooring lmc4 failed. Mooring lmc6 could not be recovered at the end of the second deployment, and data from this site are therefore missing for the entire second period. The loss of instruments also resulted in a design change of the array, replacing the upper ADCP of mooring lmc6 by a single point current meter in the third period. In this last period, eight months of data are missing from two current meters at mooring lmc5a as well.

All current velocity records were low pass filtered (forward and backward) with a 3.5-day Butterworth filter and were subsampled at daily intervals, to remove tidal variability and inertial oscillations. The velocity data was inter- and extrapolated on a grid with a 25 m resolution in the vertical and a 1 km resolution in the horizontal direction. This inter- and extrapolation was done primarily in the vertical, because correlations of time series of instruments along cables were found to be much stronger than between cables (*Ridderinkhof et al.*, 2009). To fill in the velocity grid between the eastern- and westernmost moorings and the sides of the Channel, two methods were tested: (1) extrapolating to zero velocity at the boundary (no slip), and (2) keeping the velocity constant from the outermost mooring (full slip). The second method is the default method used in the studies of this dissertation. The effects of the different extrapolation methods on the resulting volume transport estimate will be discussed later. The gaps in the data record introduced by the failure of instruments were filled with estimates made by multiple linear regression (both horizontal and vertical), based on the time periods with existing data. Finally, the gaps in the transport time series introduced by mooring service and redeployment were filled by linear interpolation in time.

2.2.2 Other data sources

The time series of the Indian Ocean Dipole (IOD) index used in section 2.4.3 was obtained from http://ioc3.unesco.org/ oopc/state_of_the_ocean/. This index (*Saji et al.*, 1999; *Webster et al.*, 1999) is a measure of the zonal gradient of the sea surface temperature anomaly in the tropical Indian Ocean. The index is positive (negative) when the sea surface temperature anomaly of the western tropical Indian Ocean is higher (lower) than that of the eastern tropical Indian Ocean.

The sea surface height anomaly (SSHA) fields were produced by Ssalto/ Duacs and distributed by Aviso, with support from Cnes. The data was downloaded from http://www.aviso.oceanobs.com/en/data/products/sea-surface-height-products/global/msla/index.html. We used near-real-time data that was gridded on a $1/3^\circ \times 1/3^\circ$ Mercator grid.

Wind fields were obtained from QuikSCAT Level 3 data (http://podaac.jpl.nasa.gov/DATA_PRODUCT/OVW/index.html#quikscat, product 109), which is daily data gridded on a $0.25^\circ \times 0.25^\circ$ grid. Wind stresses were calculated from this data set, using an approximation for the drag coefficient C_d as proposed by *Smith* (1980):

$$C_d = \frac{1}{1000}(0.61 + 0.063\,U_{10}), \tag{2.1}$$

where U_{10} denotes the wind velocities at 10 m above sea level.

2.3 Observed velocities at the mooring section

Daily current vectors (Figure 2.2) demonstrate the different character of the currents at the western end compared to the rest of the section, with a stronger preference towards the south-southwest direction. Over most of the section the current records down to at least the 1000 m level are dominated by recurring events of strong, rotational motion, representing the passage of anticyclonic eddies that are a well known feature of the circulation in the MCh (*Biastoch and Krauss*, 1999; *Ridderinkhof and De Ruijter*, 2003; *Harlander et al.*, 2009).

Mean current vectors and standard deviation ellipses at the 100 and 1500 m (or as near 1500 m as possible) levels for the entire 4.2 years of deployment are shown in Figure 2.3. In general, the standard deviation of the current velocity was relatively high compared to the mean. The strongest mean current at the 100 m depth level was directed towards the southwest and found at the two westernmost moorings. The maximum resultant flow at the western side of the Channel was a result not only of high current velocities, but also of the significantly higher level of directional stability of the currents at these loca-

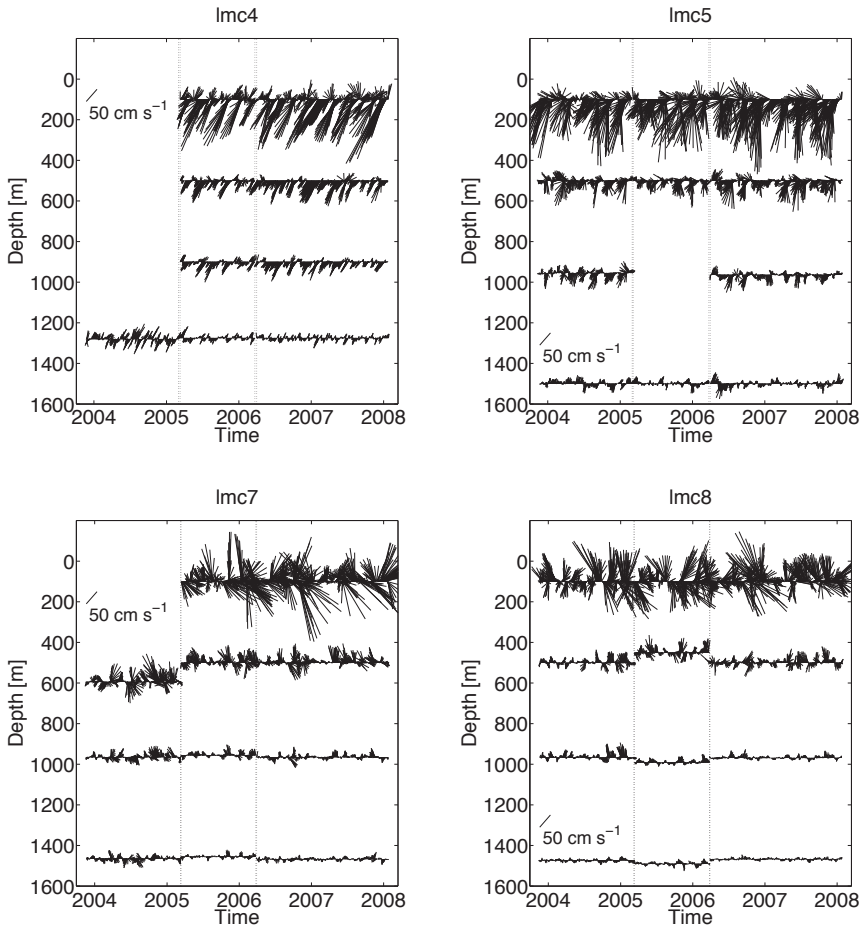

Figure 2.2: *Vector velocity plots of currents at selected depths at moorings lmc4, lmc5, lmc7 and lmc8, with a 50 cm/s vector plotted for scale. Dotted lines mark deployment breaks.*

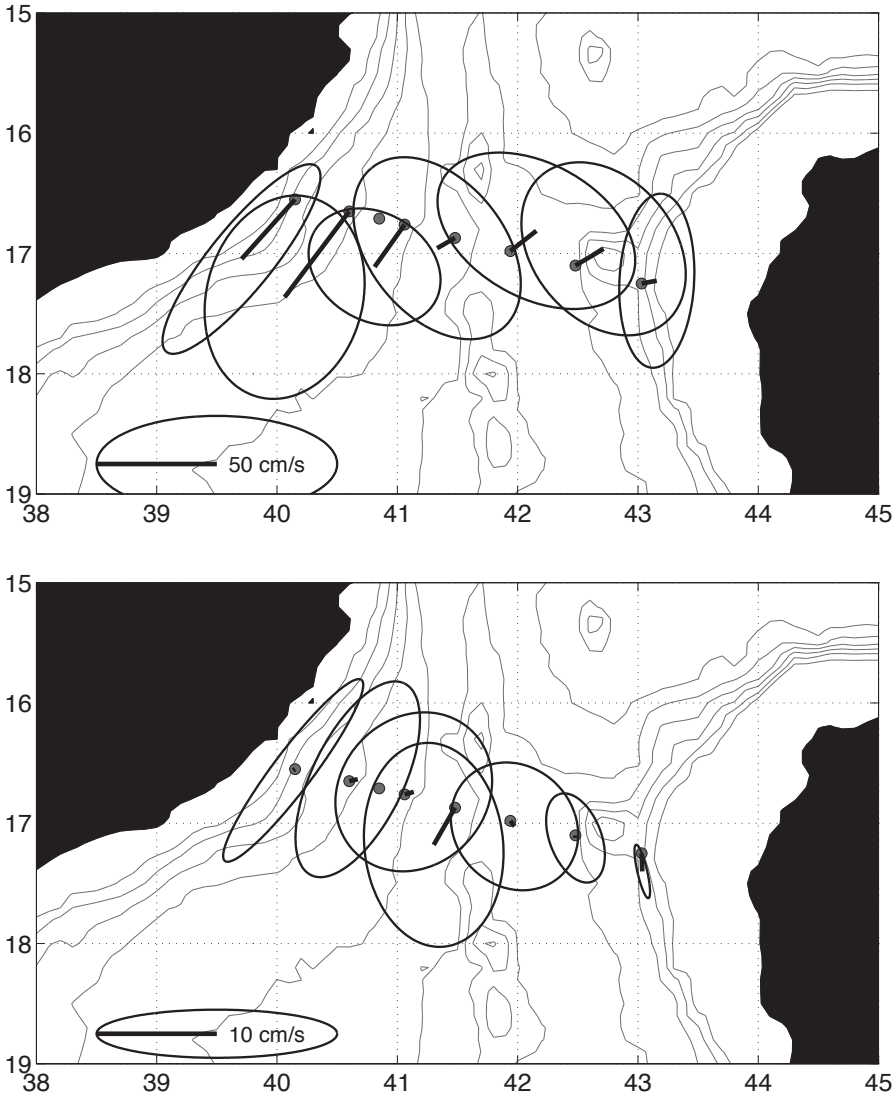

Figure 2.3: *Plan view of the mooring locations with mean velocity vectors at 100 m depth (top figure) and 1500 m depth (bottom figure), with the ellipses denoting 1 standard deviation.*

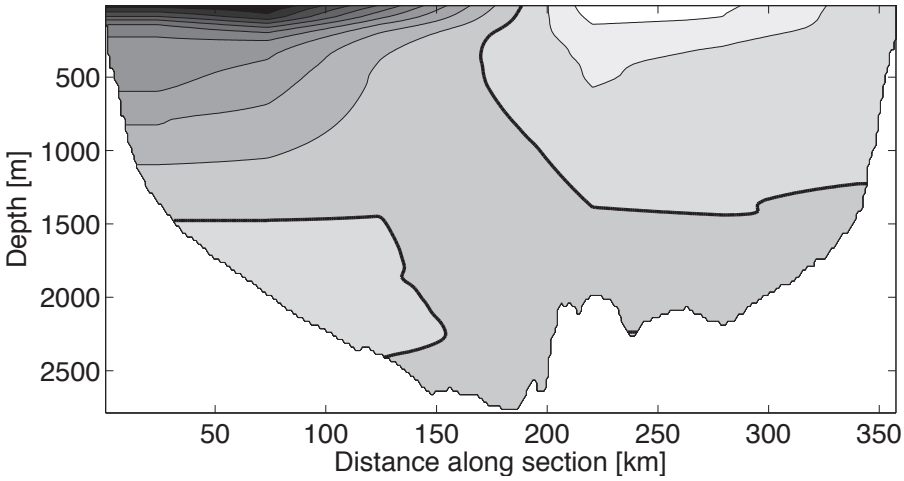

Figure 2.4: *Cross section of the mean velocity perpendicular to the mooring section. Velocity contours at 5 cm/s intervals; darker (lighter) colors denote southward (northward) flow; the bold line is the zero velocity contour.*

tions. The westernmost mooring (mooring lmc4, Figure 2.2), in 1350 m water depth, showed the highest steadiness or directional persistence of all the moorings, with Neumann factor values (the ratio of vector mean to scalar mean, expressed as a percentage, where 100% means unidirectional flow) of above 70% throughout the upper 900 m. Here, as well as at the easternmost mooring (lmc9), the standard deviation ellipse was elongated and largely aligned with topography (Figure 2.3), whereas in the center of the Channel, a smaller proportion of the variance is along the major axis. The second mooring from the west (lmc5) also had a relatively high level of directional persistence, and in addition the highest current speeds in the upper layers (Figure 2.2).

The cross-section of the mean velocities also demonstrates the strong southward flow on the western side of the Channel (Figure 2.4). The core of the southward flow was located in the upper 100 m, where the long term average velocity exceeded 40 cm/s. The mean current magnitude in the upper layer was similar between the moorings lmc4 and lmc5 (slightly stronger at lmc5), while at levels below the upper few 100 m the poleward flow was strongest and extended the deepest at the westernmost mooring, situated 30 km from the coast in a water depth of 1350 m. Poleward mean velocities extended throughout the upper kilometer of the water column at the two western moorings, weakening with depth to the zero velocity contour which was found at 1500 m at the second mooring from the west in 1990 m water depth.

On the eastern side of the Channel, currents were on average equatorward in the upper 1500 m. The northward flow was weaker than the southward flow on the western side, with maximum velocities in the upper 100 m of > 10 cm/s. However, the northward counter flow took up a substantial part of the cross sectional area, covering half of the Channel from the center to the eastern edge, and with velocities only reaching zero at about 1500 m depth, like on the western side. The observed mean flow pattern with its east-west asymmetry is most likely the result of the anticyclonic eddies superposed on a background southward flow (*Harlander et al.*, 2009).

Leaning on the continental slope on the western side of the Channel is the northward flowing deep Mozambique Undercurrent, with mean northward velocities of 0.3 – 4.8 cm/s (varying with depth level and measurement period) and maximum equatorward velocities of up to 35 cm/s. The strength of the flow in the Undercurrent increased with depth, and thus the highest long-term mean velocities – 3.8 cm/s towards the north-east, averaged over all three deployment periods – were found at the deepest measurement points, in the depth range 2200–2300 m. *Ridderinkhof and De Ruijter* (2003) suggested that the Undercurrent found in the MCh might be a continuation of the Agulhas Undercurrent (*Beal and Bryden*, 1997). There are insufficient data from the region between the Agulhas region and the MCh to conclude whether there is a continuous current linking the two regions, but model results from a recent study (*Biastoch et al.*, 2009) indicate that the link between the Agulhas and Mozambique Undercurrents is weak and the path of the deep water in the region complex, with a large part of the flow being detrained into eddies or into the Agulhas Current, and only a small portion continuing northward along the African continental shelf. Also, in a study on the water mass characteristics in the Southwest Indian Ocean, no direct connection between the Agulhas and Mozambique Undercurrents was found (*Van Aken et al.*, 2004). This agrees with the observation that the mean velocity of the undercurrent at the LOCO section (17°S) was much weaker than the 10 cm/s observed by *Beal and Bryden* (1997) at 32°S.

The mean flow structure was qualitatively similar between the different deployment periods, but the strength of the flow varied. The changes in current magnitude occurred on both sides of the 'eddy' part of the flow pattern, i.e. both in the southward flow in the upper western part of the Channel, and the northward flow on the eastern side. During the first measurement period, near-surface southward velocities of over 50 cm/s were found at the western side of the Channel, and the northward near-surface velocities on the eastern side exceeded 10 cm/s between moorings lmc7 and lmc8. While the zero velocity line was found at a similar depth and with a similar extension during the second

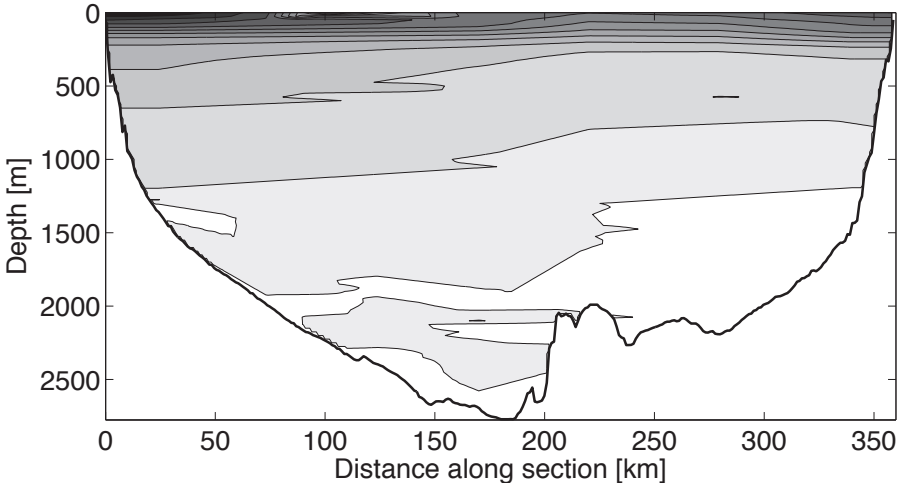

Figure 2.5: *Cross section of the standard deviation of the velocity perpendicular to the mooring section. White field: standard deviations ≤ 5 cm/s; contours at 5 cm/s intervals.*

period, the upper layer flows were significantly weaker, with a southward near-surface mean velocity of about 40 cm/s and northward velocity of <10 cm/s on the eastern side. During the last deployment period, the eddy velocities were stronger, exceeding 50 cm/s southward and 15 cm/s northward. While both northward and southward velocities became stronger, the increase in southward velocities was larger.

Temporal variability of the currents was higher in the western half of the Channel, as indicated by the standard deviations of current velocity (Figure 2.5). Across the Channel, current variability was highest in the upper few 100 m of the water column, but at the western end of the section, the 10 cm/s contour of standard deviation (over the whole 4.2 years) was found well below 1000 m, rather than at 700 m depth as on the eastern side. High variability was also found at mooring lmc5a, in particular during the first period, when the velocity standard deviation at 500 m was higher at mooring lmc5a (>20 cm/s) than anywhere else on the section. At depth, the variability was also higher on the western side and in the deepest part of the Channel, contrasting with the deep water on the eastern side of the Channel where both mean velocity and standard deviation were close to zero. In short, the distribution of current variability reflects the mean flow in that the strongest mean velocities also have the highest level of variability.

2.4 Transport

2.4.1 Volume transport calculation

The sensitivity of the volume transport estimate to the interpolation methods and the use of data 'reconstructions' was tested by comparing several estimates in Figure 2.6. The choice of the horizontal extrapolation method near the Channel boundaries ('full slip' versus 'no slip') makes a difference of about 10% of the total transport. Letting velocities approach zero at the boundary yields a transport that is 1–2 Sv lower (from 0.9 Sv for the weak transport in the second deployment period, to 1.9 Sv for the third period) than using constant velocities to the sides. These two approaches could be seen as two extremes and the real transport value might be expected to lie between these two endpoints (Figure 2.6).

As an alternative to the data reconstruction method, transports were also computed using a more basic approach, namely filling all long data gaps by horizontal interpolation. The most complete data set – that from the third period – was subsampled to correspond to the set with missing data, and new transport estimates for this period were computed. Removing mooring lmc4 (or the upper ADCP at mooring lmc4) made a negligible difference to the total volume transport in the full slip case, but led to a strong underestimation in the no slip case, reducing the mean southward transport by more than 5 Sv. Removing mooring lmc6 led to a less strong but still significant underestimation of the mean transport, of 1.5 Sv. These differences correspond to the transport estimates for the other periods with the basic approach. These tests imply that the filling of large data gaps using the multiple linear regression approach is an improvement over a more basic approach, and reduces the bias otherwise introduced by varying instrument coverage.

The effect of different inter- and extrapolation choices on the time mean transport was our main concern in this study, but it should be noted that the differences in instantaneous (daily) transport values between estimates from different methods are sometimes quite large. The temporal variability of the transport was somewhat higher using our gapfilling method, which indicates that the loss of data during some measurement periods leads to an underestimation of the transport variability as well as of the mean transport, unless special care is taken in the filling of these gaps. The mean bias between various methods of approximately 1.5 Sv may serve as an estimate of the systematic error in the transport calculation. Transport values discussed hereafter refer to the time series produced using reconstructed data sets to fill large gaps, and applying the full slip condition for flow near the horizontal boundaries (black

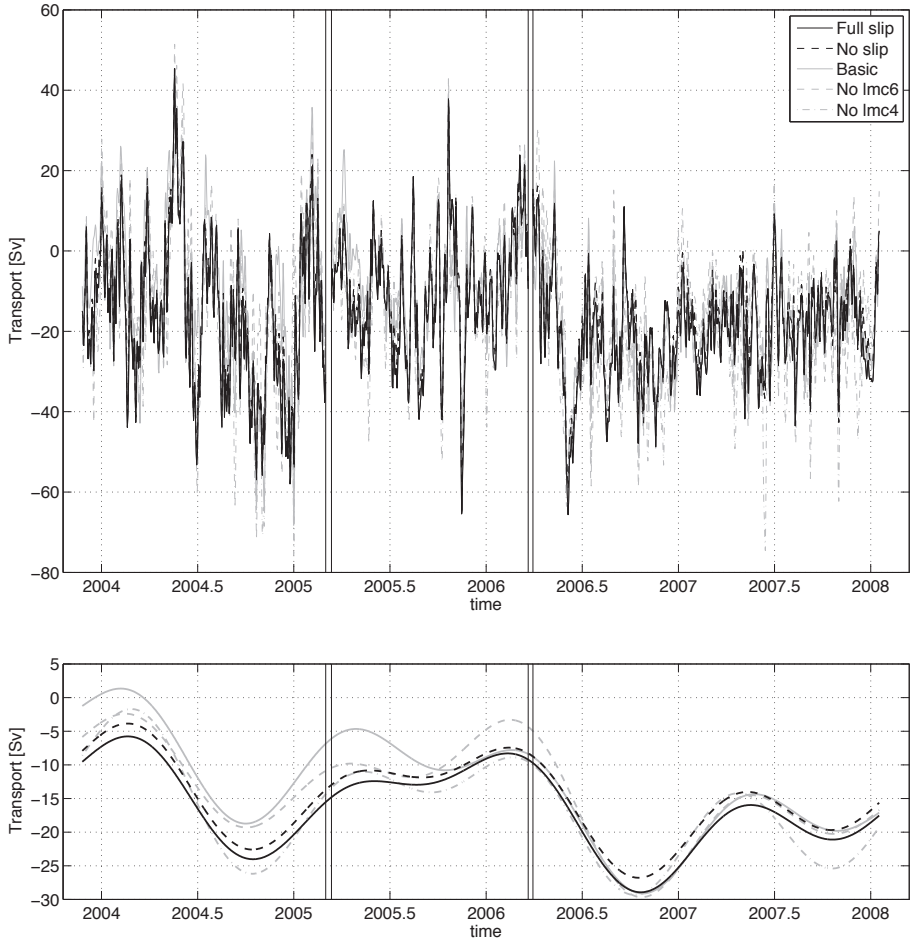

Figure 2.6: *(top panel) Time series of total volume transport through the section, computed with five different inter- and extrapolation schemes. 'No slip' forces zero velocity at the side boundary; 'full slip' keeps velocities constant to the side; 'basic' fills large gaps using horizontal interpolation rather than individually adapted gap filling techniques; in 'No lmc6' and 'No lmc4' , data from mooring lmc6 and the upper ADCP in mooring lmc4 is omitted for the whole time series. The vertical lines mark mooring turnovers. (bottom panel) The same five transport estimates filtered to exclude frequencies higher than 1.2/y.*

solid line in Figure 2.6). The resulting mean transport over all three deployment periods amounted to 16.7 Sv poleward, with a random error of 3.1 Sv about the mean (based on an integral time scale of 30 days).

The daily values of this time series range from 45 Sv northward to 65 Sv southward. Maximum northward transport occurred in mid-May 2004. At the peak of northward transport, a strong northward current core was present in the center of the Channel, reaching down to 1500 m. Only a weak southward core, centered at 1000 m depth at mooring lmc5, was present on the western side of the Channel. About 40 days later the transport had shifted to strongly southward, with the more typical strong southward flow at the western side of the Channel, strongest at the surface but present almost throughout the whole water column at the westernmost site, and surface intensified southward current also found on the eastern side of the Channel. Northward transport also peaked in October 2005, when the northward velocities on the eastern side took up more than half of the Channel width and the southward flow on the western side was unusually shallow and weak. Maximum southward transport occurred in November 2005. This event was marked by a strong and deep-reaching southward flow on the western side of the Channel, as well as a relatively strong southward flow in the upper layer on the eastern side.

The volume transport estimate exceeds that of *Harlander et al.* (2009) based on the same data set for the first two measurement periods, both with regard to the mean (13.6 Sv for the two first periods compared to their 8.6 Sv) and to the variability, with daily values ranging from 45 Sv northward to 65 Sv southward rather than 30 and 60 Sv, respectively. The discrepancy between our transport estimate and that of *Harlander et al.* (2009) is caused by several different choices in terms of methods for filling gaps (temporal and spatial) in the data set. The use of a full slip condition at the boundaries, individually adapted gap-filling techniques for large gaps, and different interpolation and extrapolation methods (linear, first vertical then horizontal, versus cubic 2-dimensional gridding) all contribute on its own to a higher transport estimate. The differences in variability can also partly be explained by the use of a different filtering method and window: *Harlander et al.* (2009) used a weekly cosine filter, whereas here a 3.5-day Butterworth filter was used. The sensitivity analyses of both studies suggest that the loss of mooring lmc6 and partial loss of mooring lmc4 lead to an underestimation of the transport. In this study it was attempted to compensate for these losses by using the data from the last, very successful mooring period as a basis for interpolation. In agreement with the earlier study, we find that the changes in transport between different periods, e.g. the significantly lower transport during the second period, are not artifacts due to changes in measurement coverage, but are real.

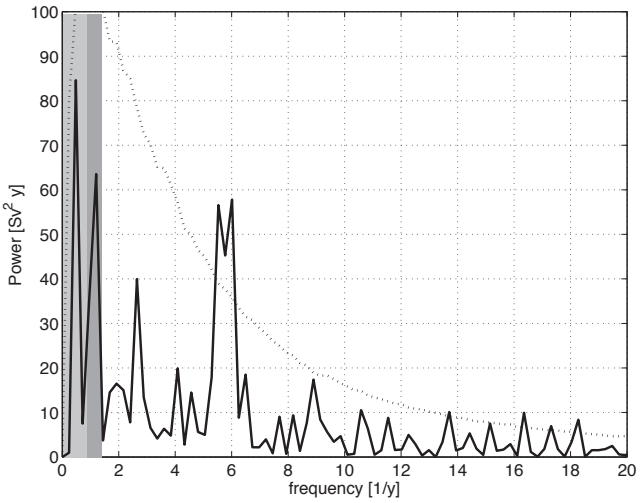

Figure 2.7: *Power spectrum of the transport. The dotted line denotes the 95% confidence interval of an AR(1) red noise spectrum. The two vertical gray bands show the frequency range over which the transport time series was filtered in Figure 2.8.*

The transport estimate as described in this dissertation and in *Ridderinkhof et al.* (2009) is an improvement on the previous estimates because it made use of the internal correlation between the instruments and of knowledge obtained by the third deployment period, which was the most complete. Either way, the choice of methods does not affect the main features of the transport time series, such as the large transitions both with respect to the mean transport and (dominant frequencies of) variability.

The power spectrum of the transport time series is shown in Figure 2.7. It shows a clear peak at a frequency of five to six times a year, i.e., a period of around 70 days, which was also observed in previous studies (e.g. *Schouten et al.*, 2003; *Harlander et al.*, 2009). At longer time scales, the variability is mainly at frequencies around 1/y (seasonal cycle) and 0.5/y, although neither peak is significant to an autoregressive model spectrum of order one (AR(1) spectrum). This is due to the relatively short length of the time series and the strong variability at high frequencies. Nevertheless, in the next section the origin of the variability at these long time scales will be discussed.

Compared to the frequency spectrum of the first two deployment periods, computed in the study of *Harlander et al.* (2009), the spectrum of the full 4.2-year time series is similar in a qualitative way, as the peaks occur around the same frequencies. However, the variability around five to six times a year is somewhat lower in the time series over all three periods than in the timeseries

over the first two periods. The variations in the strength of this particular frequency are very remarkable, but lie behind the scope of this dissertation. In the remainder of this chapter, focus will be on the longer time scales.

2.4.2 The transport time series in three frequency bands

Also by comparing the means of the transport in the three periods, it is apparent that there is variability at longer time scales. In the first deployment period, the mean transport was 16.0 Sv southward. In the second period, the transport was relatively weak, with a mean of 10.8 Sv southward. The mean transport of the third deployment period was strongest: 20.6 Sv southward. Occasionally, the transport changed quite rapidly. In the austral summer of 2004 – 2005 for example, the southward transport decreased from 30 Sv to almost no transport, while around May 2006 the transport changed from a 10 Sv northward transport to a 25 Sv southward transport. Both transitions took approximately two months.

To examine the origin of the variability at longer time scales, the transport time series was decomposed into three frequency bands (Figure 2.8, top panel). The selection of frequency bands was based on the power spectrum of the transport (Figure 2.7). The low frequency band consists of frequencies between zero and 0.9/y. Over the whole time series, the dominant period of the transport in this band is 2 years; its maximum amplitude is 8.9 Sv. The second frequency band is the yearly cycle (frequencies between 0.9/y and 1.2/y). The amplitude of the transport in this band has a maximum of 4.1 Sv. Finally, in the high frequency band all frequencies higher than 1.2/y are combined. The transport in this band has the largest range of the three bands, and varies between 55.3 Sv northward and 54.6 Sv southward.

The variability at longer time scales is the superposition of the variability in the low frequency band and the yearly frequency band (Figure 2.8, bottom panel). For example, the transport increase in May 2006 was due to an increase in both bands. Before this event, in the austral summer of 2005–2006, the total transport was weak because of the cancelling effect of the opposed transports in the low and yearly frequency bands. The total transport increased in May 2006, when the transport in both the low frequency band and the yearly band had the same (southward) direction and increased. Meanwhile, there was a sharp peak in the transport in the high frequency band. This resulted in a very sharp increase in the total transport. Afterwards, the total transport remained strong since especially the transport in the low frequency band remained (strongly) southward. A similar analysis can be given for the decrease of the mean transport in the end of 2004 – beginning of 2005.

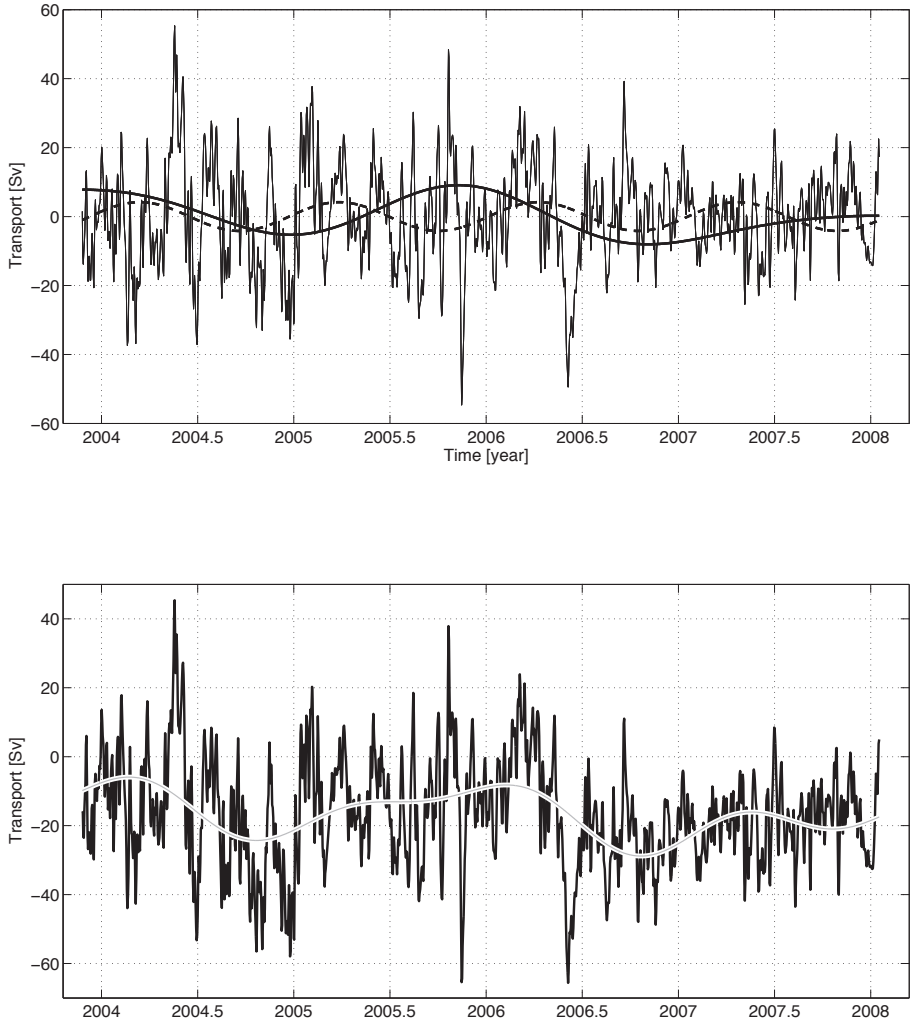

Figure 2.8: *(top figure) The transport time series decomposed into three frequency bands: the low frequency band (0–0.9/y, thick solid line), the yearly frequency band (0.9/y – 1.2/y, thick dashed line), and the high frequency band (1.2/y – 100/y, thin solid line). (bottom figure) The original transport time series (black line) and the superposition of the transport in the low and yearly frequency bands (gray line). The superposition neatly follows the long term variability of the transport.*

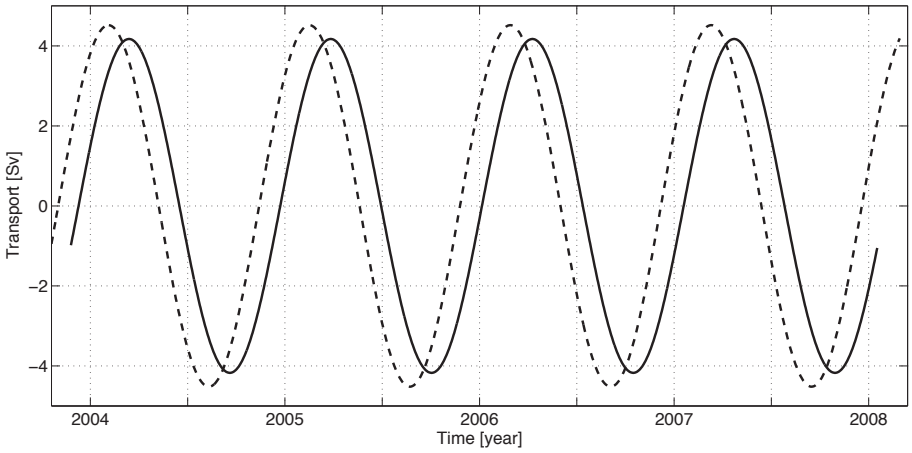

Figure 2.9: *Time series of the band filtered (0.9/y – 1.2/y) observed Mozambique Channel transport (solid line) and the calculated transport through the Channel induced by the winds west of 75°E (dashed line).*

Thus, these interannual transport changes occur because of the almost parallel increase of the transport with a small phase shift in the low and yearly frequency bands. To understand the origin of the variability of the transport at these longer time scales, the origin of the variability in the yearly and low frequency bands is investigated in the next section.

2.4.3 Origin of the variability in the yearly and low frequency band

The transport in the yearly frequency band is primarily related to the wind stress pattern in the Indian Ocean. *Matano et al.* (2002, 2008) showed that due to the topographic ridges, regional barotropic processes control the seasonal variability in the South Indian Ocean. The origin of the seasonal variability of the transport in the MCh should therefore be found west of 75°E (see Figure 3a of *Matano et al.*, 2008), since the seasonal variability cannot cross the Mid Indian Ridge. Applying the linear island rule (*Godfrey*, 1989) on the wind stress west of 75°E, band-pass filtered between 0.9/y and 1.2/y, gives a transport variability in the MCh of 4.5 Sv (Figure 2.9). This is slightly higher than the observed amplitude of the transport in the yearly band in the Channel. The lag between the wind forcing and the transport is about a month, consistent with the propagation speed of the seasonal cycle (*Matano et al.*, 2008).

The transport in the lowest frequency band is presumably related to large scale variability in the Indian Ocean. In Figure 2.10, the low pass filtered time series of the MCh transport (equal to the thick solid line in the top panel of

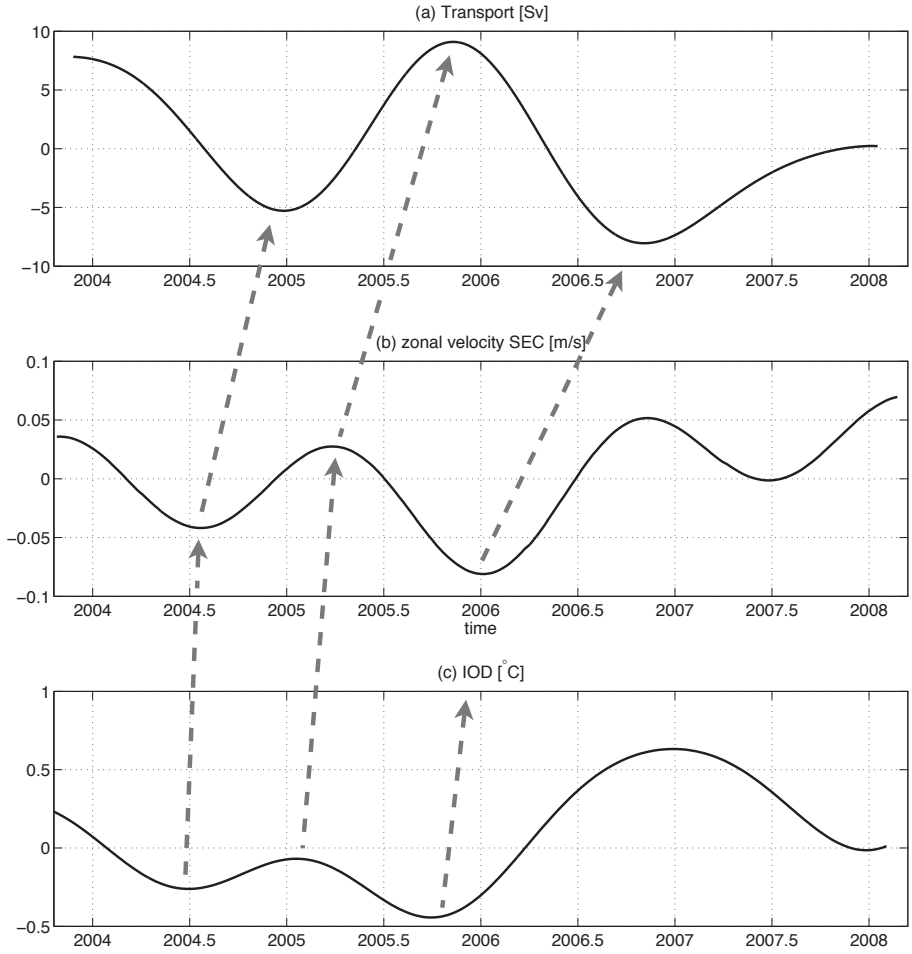

Figure 2.10: *Time series of low pass filtered Mozambique Channel transport (a), zonal velocity anomaly of the SEC (b) and the IOD index (c). The zonal velocity of the SEC was derived from a SSHA time series ($80°E$; $10° - 15°S$, Figure 2.11) by using the geostrophic balance.*

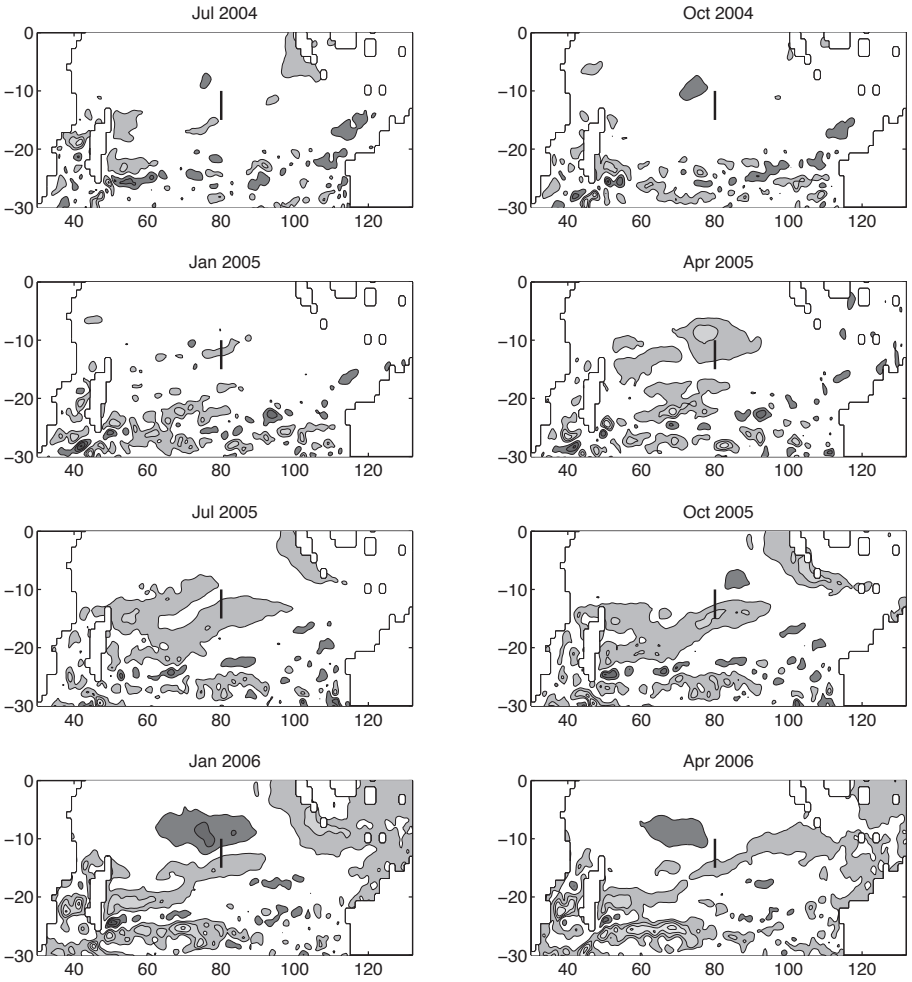

Figure 2.11: *Eight snapshots of low pass filtered SSHA in the Indian Ocean from July 2004 to April 2006. The black line in each panel denotes the section along which the strength of the SEC was determined. Contours are drawn every 5 cm, darker (lighter) colors are negative (positive) values. The values between -5 cm and 5 cm are omitted.*

Figure 2.8), the zonal velocity anomaly of the South Equatorial Current (SEC) and the IOD index are shown. The strength of the SEC is derived from the gradient in sea level anomaly from Aviso at 80°E and at the section $10° - 15°$S (Figure 2.11), by using the geostrophic balance.

The low pass filtered zonal velocity of the SEC and the low pass filtered transport in the MCh are positively correlated. In July 2004 and January 2006, the SEC had a maximum westward flow, of respectively 4.2 cm/s and 8.1 cm/s. Assuming a current width of 5° and 200 m depth (*Conkright et al.*, 2002), this is equivalent to a transport anomaly of 4.7 Sv and 8.9 Sv, respectively. A couple of months later, these anomalies were followed by a maximum southward transport through the LOCO section with a similar magnitude. After an anomalous eastward flow in the SEC, the southward flow in the MCh weakened, for example in the austral summer of 2005 – 2006. The correlation between transport and SEC strength is significant at an 80% confidence level. The correlation coefficient is 0.48 where the SEC leads the transport by 8.6 months. This lag can be explained by the speed of a baroclinic wave with a Rossby radius of deformation of 100 km (Figure 6 of *Chelton et al.*, 1998) travelling with a speed of 20 cm/s.

A similar relationship between the SEC and the MCh throughflow has been described by *Palastanga et al.* (2006). Their Figure 10 shows that in the period 1993 to 2003, a few months after the strengthening (weakening) of the SEC, the strength of the Northeast Madagascar Current (NEMC) increases (decreases), followed by an increase (decrease) of the strength of the MCh throughflow.

The strength of the SEC anomaly is probably related to the sea level anomaly changes by the IOD cycle and by changes in the Indonesian Throughflow. The low pass filtered IOD index (Figure 2.10c) has a similar shape as the low pass filtered SEC strength, although the amplitudes of the IOD index are not consistent with the other two time series. Nevertheless, the time series of the IOD index and the SEC anomaly are positively correlated to a confidence level of 90% with a correlation coefficient of 0.60. The lag between the time series is 2.3 months. This correlation might be stronger in a longer time series. Also, we would like to emphasize that the correlation between IOD index and SEC anomaly does not have to be linear. The IOD index is a measure of the zonal sea surface temperature gradient in the tropics, while the SEC strength is measured somewhat further poleward and is derived from the meridional gradient of the sea surface height. The temperature and sea surface height are related (a negative SSH anomaly indicates upwelling, which causes colder waters to rise to the surface), and a strong nonlinear relation might exist between the two.

In the first one-and-a-half years of the studied period, from January 2004

to July 2005, there were no large gradients of the SSHA in the tropical Indian Ocean (Figure 2.11). The anomaly in the strength of the SEC was therefore relatively small. In October 2005 this changed, as the IOD index was in a negative phase. The SSHA gradients in the Indian Ocean became therefore somewhat stronger. A negative anomaly in SSHA appeared around 80°E; 8°S. This anomaly increased and moved westward (January 2006), just as during the IOD in 1997 (*Webster et al.*, 1999; *Rao et al.*, 2002; *Feng and Meyers*, 2003; *Palastanga et al.*, 2006). It strengthened the tropical gyre and thereby intensified the SEC. In April 2006, the negative phase of the IOD was ending, as the negative SSH anomaly weakened. While the IOD index transferred to its positive state, the signal induced by the negative state travelled westward.

There thus seems to be a negative correlation between the IOD cycle and the transport through the Mozambique section. A positive IOD index is related to a weakening of the tropical gyre and in the end a weaker southward transport through the Channel, while a negative IOD index strengthens the tropical gyre, which is followed by a stronger, southward transport. The coupling via the SEC is essential, as the IOD index itself is not significantly correlated to the Mozambique Channel transport. The lag between the IOD phase and the transport in the MCh in the studied time span is roughly one year, about half of the typical IOD time scale. Therefore, a positive IOD index coincides with a period of more southward MCh transport (Figure 2.10). This could lead to incorrect interpretations of cause-effect relations. For example, *Palastanga et al.* (2006) observed a southward transport increase just after the IOD+ phase of 1997/1998, and concluded that the IOD+ phase caused the transport increase. However, this is inconsistent with the time series in Figure 2.10, as here the transport increases just before the IOD+ phase of 2006. The explanation given here, i.e., a negative IOD phase causes a transport increase after a lag of about one year, explains both the transport increases of 1997/1998 and of May 2006.

The strength of the Indonesian Throughflow has a variability over long time scales. The Indonesian Throughflow feeds directly into the SEC (*Gordon*, 1986; *Song et al.*, 2004; *Talley and Sprintall*, 2005). *Sprintall et al.* (2009) observed a weaker ITF transport around November 2004 and a stronger transport around July–August 2005. This seems to be in agreement with the observed anomalies in the SEC (Figure 2.10).

The low frequency MCh transport is not correlated to the low frequency wind stress in the Indian Ocean, although for example *Horii et al.* (2008) have shown that there were anomalous winds in the tropics preceding the IOD+ of 2006 (see also *Reason et al.*, 2000). The low pass filtered island rule induced MCh transport by the anomalous wind stress (*Godfrey*, 1989) is maximum in

April 2006, when it contributed an extra 2.3 Sv to the transport. This was 26% of the maximum southward low frequency transport of 8.9 Sv. Nevertheless, in the 4.2 year time series, the wind induced transport was mostly out of phase with the Channel throughflow, as it had a different periodicity of 14 months instead of about 2 year.

2.5 Conclusions

The long term dataset from the array of current meter moorings in the MCh offers excellent opportunities to study variability in currents and volume transports in this branch of the large scale circulation of the Indian Ocean. Quantitative estimates on variability in the long term volume transport are sensitive to the spatial interpolation that is applied to obtain a complete coverage of currents on the entire cross section, especially if spatial gaps are present in the basic dataset. Repeated periods of observations are very useful in order to be able to derive interpolation schemes for an estimate of currents at locations where no observations are available.

The mean volume transport through the Channel was 16.7 Sv $\pm$ 3.1 Sv poleward. Daily transport values ranged between 45 Sv northward and 65 Sv southward. The length of the observations, covering more than 4 years, allows a study on the variability in the volume transport on seasonal and interannual time scales. Seasonal variability has an amplitude of about 4 Sv with the strongest southward currents in the austral winter. The amplitude of this signal is remarkably close to an estimate based on an application of the island rule using the observed seasonal variability in the winds in a region to the west of the Mid Indian Ridge in the Southern Indian Ocean.

Variability on interannual time scales in the volume transport in the MCh is remarkably large (the variability is of the same order as the mean) and seems to be closely related to variability in the South Equatorial Current and the Indian Ocean Dipole (IOD) index and, presumably interrelated, variability in the Indonesian throughflow. Satellite observations on anomalies in the sea surface gradient across the SEC suggest that a relatively strong (weak) southward volume transport through the MCh is related to an increased (decreased) westward transport in the SEC. The changes in the strength of the SEC lead the changes in the MCh volume transport with a lag of about 8–9 months. The time lag between the IOD index and the MCh volume transport is about one year. For this 4 year period of observations, the IOD varies with a typical time scale of 2 years resulting in a relatively weak transport through the MCh when the IOD is at its maximum.

3

Comparison Between Observations and Models of the Mozambique Channel Transport: The Seasonal Cycle and Eddy Frequencies

The time series of the observed transport through the Mozambique Channel is compared to that of six model runs with ocean general circulation models. In the observations, the seasonal cycle can not be distinguished from red noise, while this cycle is dominant in the transport of the numerical models. It is shown that the seasonal cycles of the observations and numerical models are similar in strength and phase. The cycle has an amplitude of 5 Sv and a maximum in September and can be explained by the yearly variation of the wind forcing.

The seasonal cycle dominates the models, because the spectral density at other frequencies is underrepresented, especially in the $5/y - 6/y$ frequency range. Nevertheless, the structure of eddies in the models is close to the observed eddy structure. The discrepancy is found to be related to the formation mechanism and the formation position of the eddies. In the observations, eddies are frequently formed from an overshooting current near the mooring section, which causes an alternation between a strong southward current and the formation and passing of an eddy and results in a large variation of transport in the frequency range of $5/y - 6/y$. In the models, the eddies are formed further north and propagate through the section. No alternation similar to the one in the observations is observed, resulting in a more constant transport.

This chapter is based on:
Van der Werf, P. M., P. J. Van Leeuwen, H. Ridderinkhof, and W. P. M. De Ruijter. Comparison between observations and models of the Mozambique Channel transport: The seasonal cycle and eddy frequencies. *J. Geophys. Res. in press*, 2009.

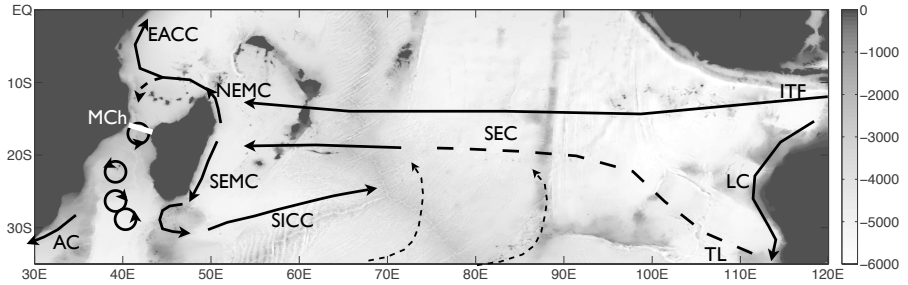

Figure 3.1: *Depth of the Southern Indian Ocean (in meters) overlaid with the main currents. The South Equatorial Current (SEC) is fed by the Indonesian Throughflow (ITF), the Tasman Leakage (TL) and the strengths of the tropical and subtropical gyres. It bifurcates at the Madagascar coast into the Northeast Madagascar Current (NEMC) and the Southeast Madagascar Current (SEMC). The NEMC bifurcates again at the African coast into the northward flowing East African Coastal Current (EACC) and a flow through the Mozambique Channel (MCh), which appears as a train of eddies. South of Madagascar, the SEMC retroflects and eddies and dipoles are shedded towards the Agulhas Current (AC). The white line in the MCh marks the LOCO mooring section.*

3.1 Introduction

In the Mozambique Channel, several water masses converge. The strength of the volume transport in the Channel is controlled by the inflow of the Indonesian Throughflow, the Tasman Leakage and the strengths of the tropical and subtropical gyre in the Indian Ocean (*Schott et al.*, 2009, and Figure 3.1). The Mozambique Channel is one of the main source areas of the Agulhas Current (*De Ruijter et al.*, 2005; *Schott et al.*, 2009). This current is an important conduit in the global thermohaline circulation, as this is the route via which warm, salty Indian Ocean water enters the South Atlantic and potentially influences the Atlantic meridional overturning circulation (*Gordon*, 1986; *Schott and McCreary*, 2001; *Schouten et al.*, 2002a; *Matano et al.*, 2002; *De Ruijter et al.*, 2005; *Biastoch et al.*, 2008b). *Van Sebille et al.* (2009b) found in a high-resolution model that this leakage is enhanced when the Agulhas Current is weaker, although when the far field is changed, a weaker Agulhas Current can also lead to a smaller leakage (*Franzese et al.*, 2009; *Rouault et al.*, 2009). The mean and variability of the transport through the Mozambique Channel are therefore important quantities to monitor the system.

In the past, many estimates of the mean transport through the Mozambique Channel have been made. Estimates, based on hydrographic data, varied between 5 Sv northward and 26 Sv southward (*DiMarco et al.*, 2002). *Ridderinkhof and De Ruijter* (2003) found a mean transport of 14 Sv from a mooring array covering 19 months in 2000 and 2001. Experiments conducted

with numerical models obtained similar results (*Biastoch and Krauss*, 1999; *Biastoch et al.*, 1999; *Matano et al.*, 2002).

Most numerical models simulate a dominant seasonal cycle in the Mozambique Channel transport. For example, *Biastoch et al.* (1999) calculated a seasonal cycle with an amplitude of 10 Sv and a minimum transport of 4 Sv northward in February–March. The seasonal cycle found by *Matano et al.* (2002) had an amplitude of 6 Sv and a minimum also in February. On the other hand, in most observational data (*Swallow et al.*, 1988; *Schott et al.*, 1988a; *Ffield et al.*, 1997; *Ridderinkhof and De Ruijter*, 2003; *Schouten et al.*, 2003) no clear seasonal cycle was observed in the transport.

In this study, this seeming discrepancy between observations and models is addressed. We use new data from both observations and numerical models, that have become available recently (Chapter 2 and section 3.2). Since November 2003, an array of moorings is being maintained across the narrowest section of the Mozambique Channel, around 16.5°S as part of the Dutch LOCO program (Long-term Ocean Climate Observations, see Figure 3.1 for its location, *Ridderinkhof and De Ruijter*, 2003; *Harlander et al.*, 2009; *Ridderinkhof et al.*, 2009). This mooring array contains, amongst others, instruments that continuously measure velocity. Previous studies with this data set have shown that the flow across the section is dominated by anticyclonic eddies, that are related to standing Rossby waves (*Ridderinkhof and De Ruijter*, 2003; *Harlander et al.*, 2009). In addition, the transport was found to be highly variable, also at long time scales (*Ridderinkhof et al.*, 2009). In the present study, we use velocity measurements from November 2003 to January 2008. This long time span, together with the high time resolution of the observations, provides a good measurement of the variability in a range of frequencies. The observational transport time series is compared to the output of six runs with four ocean general circulation models (OGCMs), that have a range in horizontal resolution and simulation duration. We have concentrated on the mean transport, the total transport variability and variability in selected frequency bands, such as the seasonal cycle (section 3.3).

This research shows that the seasonal cycles in the numerical models have the same amplitude and phase as the seasonal cycle in the observations. However, owing to the underrepresentation of the power at other frequencies, the seasonal signal dominates in the models.

The actual question should therefore be why the variability at other frequencies is not well simulated. Focus will be at the $5/y - 6/y$ frequency range, which is associated with the Mozambique Channel eddies and Rossby waves in the Channel (*Schouten et al.*, 2003; *Harlander et al.*, 2009) and has a dominant signal in the observation transport time series (section 3.4). In section 3.5, the

sensitivity of the results to the data sets will be discussed, and conclusions are drawn in section 3.6.

3.2 Data

3.2.1 Observational data from LOCO and AVISO

In the Long-term Ocean Climate Observations (LOCO) program, the mass, salinity and heat transport across the Mozambique Channel is being measured at its narrowest section, around $16.5° - 17°$S (for its location, see Figure 3.1). The mooring array is a refinement of the pilot experiment that took place between 2000 and 2002 (*Ridderinkhof and De Ruijter*, 2003). It contains temperature-salinity-depth sensors, Recording Current Meters (RCMs), Acoustic Doppler Current Profilers (ADCPs) and a sediment trap. In this study, only data from the RCMs and ADCPs are used.

The time series consists of three periods between which the instruments were serviced and redeployed: November 2003 – February 2005, March 2005 – March 2006, and March 2006 – January 2008. To remove tidal and inertial oscillations, the data were low pass filtered (forward and backward) with a 3.5-day Butterworth filter, and subsampled at daily intervals. The velocity data were inter- and extrapolated vertically and horizontally to obtain the transport. A full-slip boundary condition was applied at the bottom and side walls of the Channel. Chapter 2 gave a more elaborate discussion on the data processing. Amongst other things, it showed that for the purposes in this dissertation the transport time series is not very sensitive to the inter- and extrapolation scheme used.

Sea surface height anomaly (SSHA) data were produced by Ssalto/Duacs and distributed by Aviso, with support from Cnes. It was downloaded from http://www.aviso.oceanobs.com/en/data/products/sea-surface-height-products/global/msla/index.html. We used near-real-time data that were gridded on a $1/3° \times 1/3°$ Mercator grid. The data spanned the period 2003–2008.

3.2.2 Numerical models

In this study, we used the output from a total of six OGCM runs. These model runs were chosen because of their good spatial and temporal resolution. Since the dominant frequencies of the transport in the Mozambique Channel are within the range $4/y - 6/y$ (*Schouten et al.*, 2003; *Harlander et al.*, 2009), we have omitted model outputs with an output resolution of 1/month or lower. Also, we only considered models that used depth as a vertical coordinate. The

considered models are: Estimating the Circulation and Climate of the Ocean (ECCO), the global configuration of the Océan Parallélisé (OPA) model (two runs with different horizontal resolutions and forcing: ORCA025 and AG01-R), Ocean Circulation and Climate Advanced Modeling (OCCAM, two runs with different horizontal resolutions) and the Ocean general circulation model For the Earth Simulator (OFES). Below, each of these numerical data sets will be briefly described. A summary is given in Table 3.1. From each data set, the zonal and meridional velocities at the LOCO section across the Mozambique Channel at 16.5°S (Figure 3.1) were considered as well as the SSHA in an area spanning $35° - 55°$E and $10° - 25°$S.

The ECCO model configuration used is the one used for a quasi-operational analysis (*Menemenlis et al.*, 2005). The model is based on the MITgcm (*Marshall et al.*, 1997). Its output is available on http://ecco.jpl.nasa.gov/, of which we analyzed the data set with Kalman Filter assimilation. The output data set starts in 1993 and ends in 2008 with a 10 day output interval. It has a zonal grid spacing of 1° and a meridional grid spacing increasing from 1/3° within 10° of the equator to 1° poleward of 22°N/S. There are 37 vertical levels in the Mozambique Channel, with a vertical resolution of 10 m in the top 150 m. The time integration of the run was carried out with a 1-h time step. It uses a horizontal biharmonic friction ($k_0 = -10^{13}\, m^4/s$) and vertical Laplacian diffusion ($k_0 = 10^{-4}\, m^2/s$). The model uses the K-Profile Parameterization (KPP) vertical mixing scheme of *Large et al.* (1994) and isopycnal mixing schemes of *Redi* (1982) and *Gent and McWilliams* (1990). Atmospheric forcing was applied by 12-hourly wind stress and daily heat and freshwater fluxes from NCEP (*Kistler et al.*, 2001). The model is constrained by satellite observations of the sea surface height variability and by a collection of vertical temperature profiles (*Menemenlis et al.*, 2005).

The ORCA025 run (*Madec*, 2006) was performed by the Royal Netherlands Meteorological Institute (KNMI) as part of the DRAKKAR project (*Penduff*, 2005). The run has a 1/4° horizontal resolution and 32 vertical layers in the Mozambique Channel. This run stretches from 1968 to 2001 with a 5-day-mean output. The time step of the model was 1440 s. It has a horizontal biharmonic eddy viscosity ($-1.5 \cdot 10^{11}\, m^4/s$) and a turbulent eddy kinetic energy dependent vertical viscosity. The run was forced by a mix of ERA-40 data (*Uppala et al.*, 2005) and CORE (*Griffies et al.*, 2008) (the DFS3 data set, *Brodeau et al.*, 2009). The bottom topography uses partial steps with a minimum thickness of 25 m.

	LOCO	ECCO	ORCA025	AG01-R	OCCAM025	OCCAM008	OFES
First year	2003	1993	1968	1968	1993	1993	2000
Last year	2008	2008	2001	2005	2004	2004	2006
Span [years]	4.14	15	33	37	12	12	7
Time res. output	1 day	10 days	5 days	5 days	5 days	5 days	3 days
Hor. res.	-	1°	0.25°	0.1°*	0.25°	0.08°	0.1°
grid size 16.5°S [km]	-	106.9	26.7	10.7	26.7	8.9	10.6
Tot. layers	-	37	32	32	47	47	43
0–100m	-	10	10	10	14	14	14
100–500m	-	14	9	9	15	15	16
500–1500m	-	10	8	8	10	10	8
1500m–bottom	-	3	5	5	8	8	5
wind forcing	-	NCEP**	ERA-40 + CORE	NCEP + CORE	NCEP	NCEP	QuickSCAT

Table 3.1: *Model parameters. *AG01-R has a horizontal resolution of 0.5° globally and 0.1° in the Madagascar and Agulhas region (20°W–70°E, 47°S–7°S). **In ECCO, data assimilation is conducted on the SSH field and on a collection of vertical temperature profiles.*

The AG01-R run was conducted with a nested model (*Biastoch et al.*, 2008a,b). It consists of a global model with a 0.5° horizontal resolution (ORCA05, *Madec*, 2006) and is also part of the DRAKKAR project (*Penduff*, 2005). In the region 20°W–70°E, 47°S–7°S, a 1/10° model is nested using two-way nesting. The model has 46 vertical layers at the section and uses a bilaplacian scheme for the horizontal viscosity ($k_0 = -8.5 \cdot 10^{11}\, m^4/s$ for the global model, and $-2.125 \cdot 10^{10}\, m^4/s$ for the nest) and a vertical laplacian diffusion of $k_0 = 10^{-4}\, m^2/s$ both globally and nested. In the mixed-layer, a 1.5-level turbulent kinetic energy closure scheme is used. The run has a 5-day-mean output and stretches from 1968 to 2005. The time steps used in the integration are 2160 s for the global model and 540 s for the nest. The atmospheric forcing is applied by NCEP/NCAR reanalysis and CORE (*Griffies et al.*, 2008). The bottom topography uses partial steps with a minimum thickness of 25 m.

The OCCAM model (*Webb et al.*, 1998; *Coward and de Cuevas*, 2005) was derived from the Bryan-Cox-Semtner general ocean circulation model. In this study, we analyzed the output of model runs 103 and 401 (available at http://www.noc.soton.ac.uk/JRD/OCCAM/EMODS/select.php), spanning the period 1989 to 2005. Run 103 has a 1/4° horizontal resolution, while run 401 has a 1/12° resolution. These runs will be referred to as OCCAM025 and OCCAM008, respectively. Both runs have a 5-day-mean output (using a baroclinic time step of 900 s for OCCAM025) and a total of 47 layers in the vertical direction at the section, with 14 layers in the top 100 m. Since the runs were started from 1985 from Levitus temperature and salinity and zero velocity and thus had a shortened spin up (personal communication, B. A. de Cuevas), the first years of the output (1989–1992) were not used for analysis. Therefore these data sets stretch from January 1993 to December 2004. OCCAM uses Laplacian diffusion (horizontal viscosity is $2 \cdot 10^2\, m^2/s$ for OCCAM025 and $5 \cdot 10\, m^2/s$ for OCCAM008, and a vertical mixing coefficient of $10^{-4}\, m^2/s$). In the mixed layer, the KPP vertical mixing scheme is used (*Large et al.*, 1994). Atmospheric forcing was applied by NCEP 6-hourly forcing (*Coward and de Cuevas*, 2005). OCCAM uses partial grid cells for the bottom topography.

OFES (*Sasaki et al.*, 2008) is based on the Modular Ocean Model version 3 (MOM3, *Pacanowski and Griffies*, 1999). The model has a 1/10° horizontal resolution and a total of 43 vertical layers at the section. The data has a 3-day-mean output and stretches from 2000 to 2006. The model run uses a baroclinic time step of 200 s and a barotropic time step of 4 s. The biharmonic horizontal viscosity coefficient is calculated as in *Smith et al.* (2000) and has a value of $-2.7 \cdot 10^{10}\, m^4/s$. The vertical viscosity is calculated using the K-Profile Parameterization (KPP, *Large et al.*, 1994). The run is forced by daily mean values of the NCEP/NCAR reanalysis products and QuikSCAT winds. Partial

grid cells are used for the bottom topography.

3.3 General characteristics of the time series

3.3.1 Mean, standard deviation and power spectra

The time-mean meridional velocities (Figure 3.2) of the observations consist of three 'cores': a strong southward flow at the near surface off the African coast, a weaker northward flow at the near surface off the Madagascar coast, and a weak northward Mozambique undercurrent at the African continental slope (*De Ruijter et al.*, 2002). The two 'cores' near the surface are a result of the southward propagating Mozambique Channel eddies (*Ridderinkhof and De Ruijter*, 2003; *Harlander et al.*, 2009). A similar flow structure is observed in most numerical models (AG01-R, OCCAM025, OCCAM008 and OFES), although their flow is too strongly surface intensified. These four numerical model runs simulate Mozambique eddies at the measurement section (the structure of the eddies will be discussed in section 3.4). No eddies are simulated in ECCO and ORCA025. These models simulate two 'cores': the strong, southward near-surface flow at the African coast and a weak northward undercurrent. In ORCA025, eddies are observed further downstream, south of 20°S, while the horizontal resolution of ECCO does not suffice to simulate eddies.

Time series of the volume transport and their power spectra are shown in Figures 3.3 and 3.4. The power spectra are compared to an AR(1) red noise spectrum, which was computed with a Monte Carlo simulation with 5000 members. The seasonal cycle is not taken into account in the calculation of the red noise spectrum, because it is a deterministic signal, i.e., it is driven by external forcing. The AR(1) spectrum was therefore based on each time series subtracted by a sine function with a period of 1 year which was fitted to the time series. The model spectra have been interpolated to the frequency bins of the observed spectrum.

The mean of the southward transport over the full time series in the observations is 16.7 Sv. Two models (ECCO and ORCA025) estimate a higher transport, others (OCCAM025 and OFES) a lower transport (for an overview see Figure 3.5). Note however, that the time series of LOCO is relatively short and that large variations on the interannual time scale have been observed (Chapter 2). The mean transport in the models is not solely dependent on grid size. Of the two models with a horizontal resolution of 1/4° (ORCA025 and OCCAM025), one overestimates the transport and the other one underestimates it (respectively 23.6 Sv and 11.3 Sv). A possible explanation for these differences will be discussed in Chapter 5.

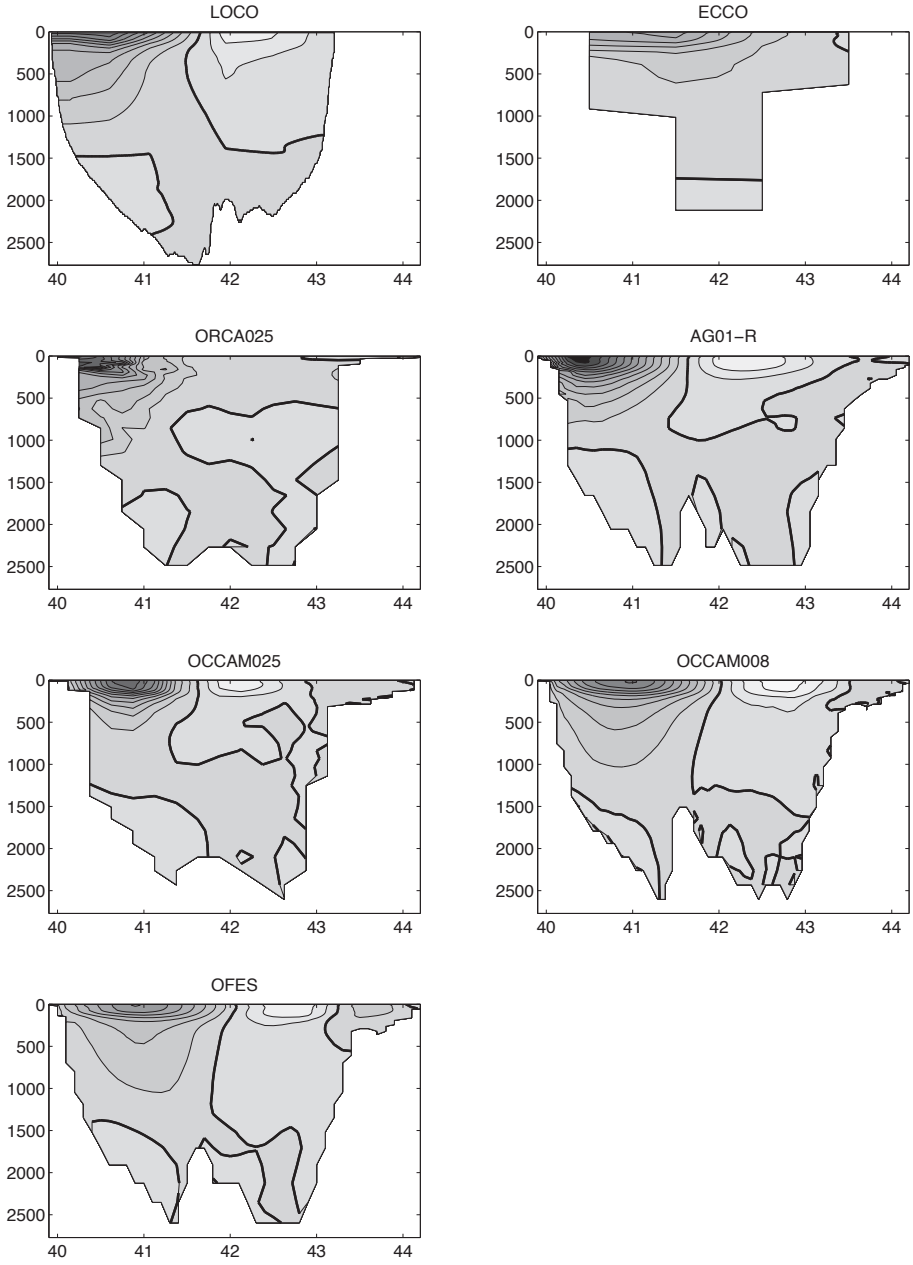

Figure 3.2: *Time-averaged meridional flow for the observations (LOCO) and the six numerical model runs. Contours are drawn every 5 cm/s, the lighter (darker) colors denote northward (southward) flow, and the thick contour denotes the zero-line. All data sets have a strong southward flow in the upper west corner of the section and a northward / weak flow in the upper east. A northward flowing undercurrent is observed in all data sets.*

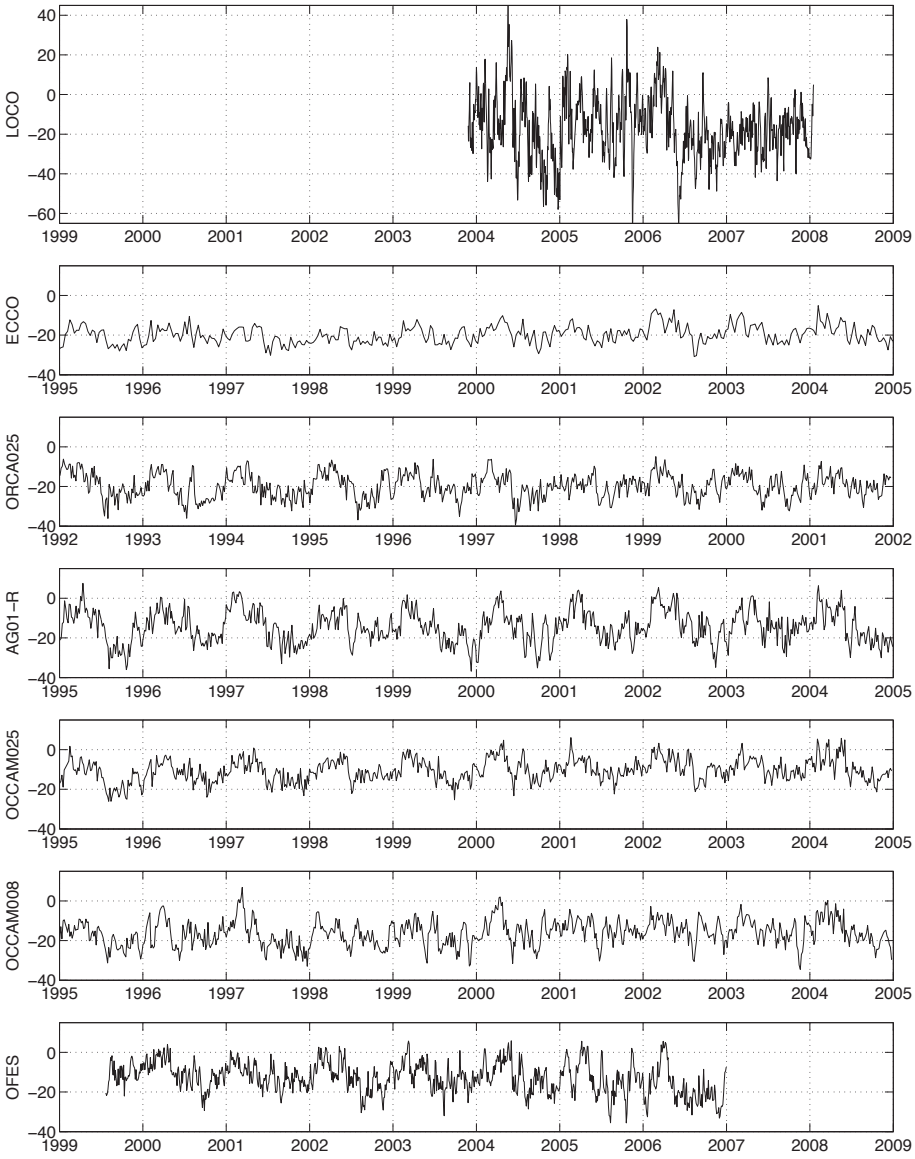

Figure 3.3: *Transport time series [Sv] for the observations (LOCO) and the six model runs in the Mozambique Channel at 16.5°S. Negative values denote southward transport. For the runs ECCO, ORCA025, AG01-R, OCCAM025 and OCCAM008, a ten-years selection of the data has been made. In the numerical model time series a seasonal cycle is observed by eye, while no clear seasonal cycle exists in the LOCO time series.*

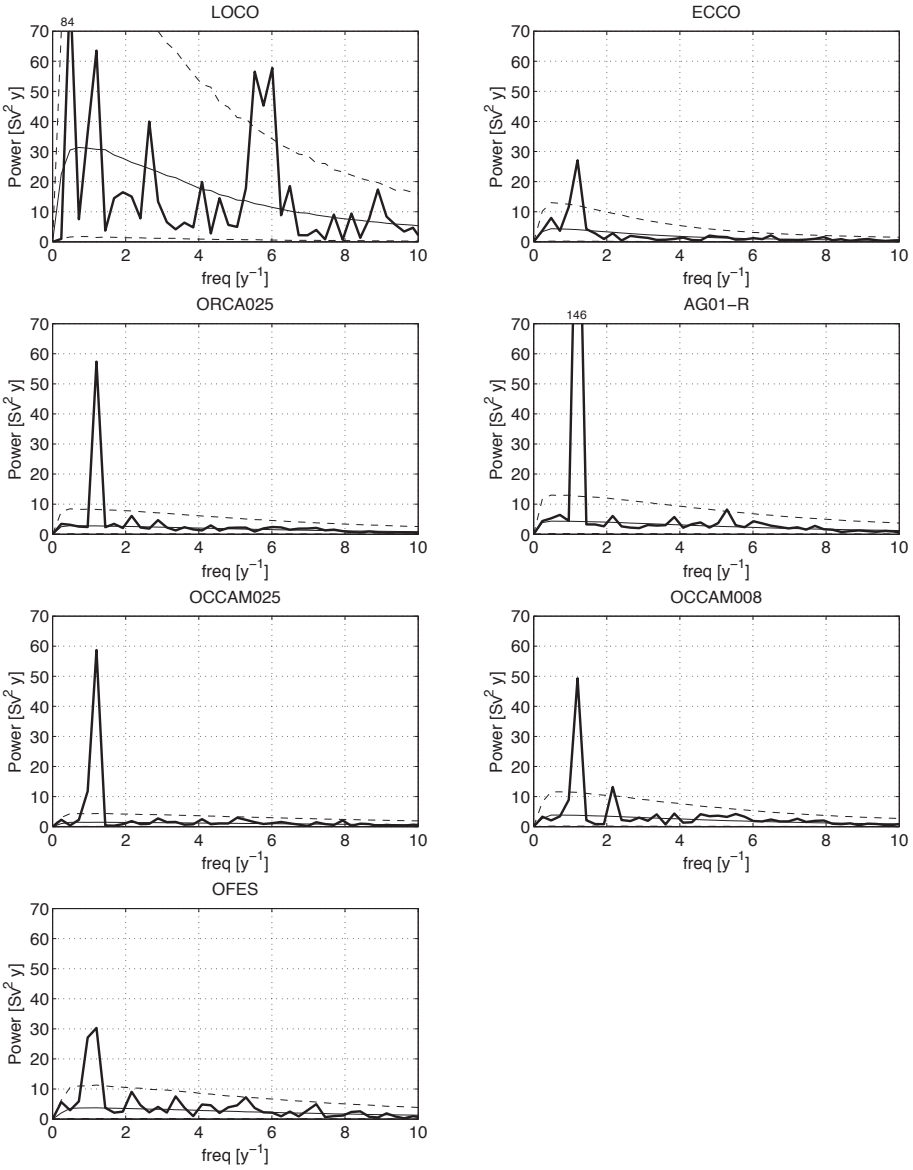

Figure 3.4: *Power spectra of the transport time series (thick lines) for the observations (LOCO) and the six model runs in the Mozambique Channel at 16.5° S. The thin lines denote the mean of an AR(1) spectrum (solid line), and the 95% and 5% confidence intervals (dashed lines). The spectra of the models were interpolated to fit the frequency axis of the observations. The power at the 1/y frequency is quite similar for all time series. On the other hand, the power at high frequencies in the models is clearly underrepresented.*

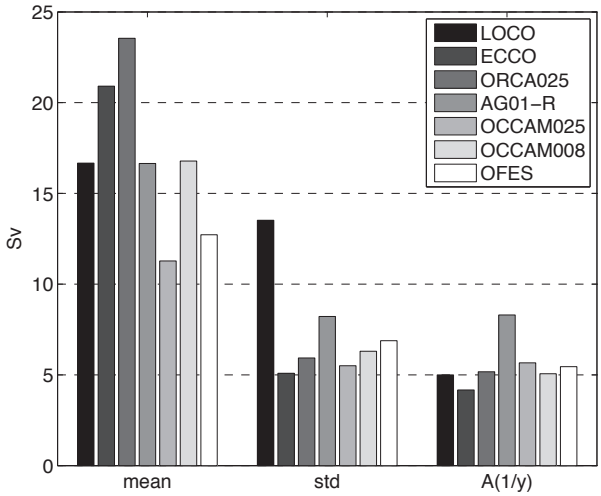

Figure 3.5: *Mean of the southward volume transport at 16.5°S, its standard deviation (std) and the amplitude of the $1/y$ frequency (A(1/y)) in the observations (LOCO) and the six model runs. The standard deviations have been calculated as the square root of the integrated variance between frequencies of 0 – 18/y.*

Stricking is the difference in transport variability. The transport in the observations ranges from 65 Sv southward to 45 Sv northward (Figure 3.3). The extremes in the model runs are much smaller. The standard deviation of the observations (13.5 Sv, calculated as the square root of the integrated variance within the frequency band of 0 – 18/y) is about twice as large as that of the model runs (Figure 3.5). That difference in transport variability is also clear in the power spectra (Figure 3.4), Especially at frequencies higher than $1/y$, the variability of the observations is much larger than that of all model runs.

Two frequency ranges in the observations have a spectral density that is distinguishable from the red noise spectrum. The first is a peak around $5.5/y - 6/y$, which is associated with Rossby waves and the Mozambique Channel eddies (*Schouten et al.*, 2003; *Harlander et al.*, 2009). The other range has a lower spectral density and ranges from $7/y$ to $9/y$. This range is most presumably associated with barotropic instability in the strongly sheared flow near Cape Amber, the northern tip of Madagascar (*Quadfasel and Swallow*, 1986; *Schott et al.*, 1988a; *Biastoch and Krauss*, 1999; *Schouten et al.*, 2003).

The spectral density of the model runs is not significant with respect to the red noise spectrum in the $7/y - 9/y$ frequency range, and only AG01-R and OFES simulate a narrowly significant variability in the $5/y - 6/y$ frequency range. Nonetheless, even for AG01-R and OFES, the spectral density in this

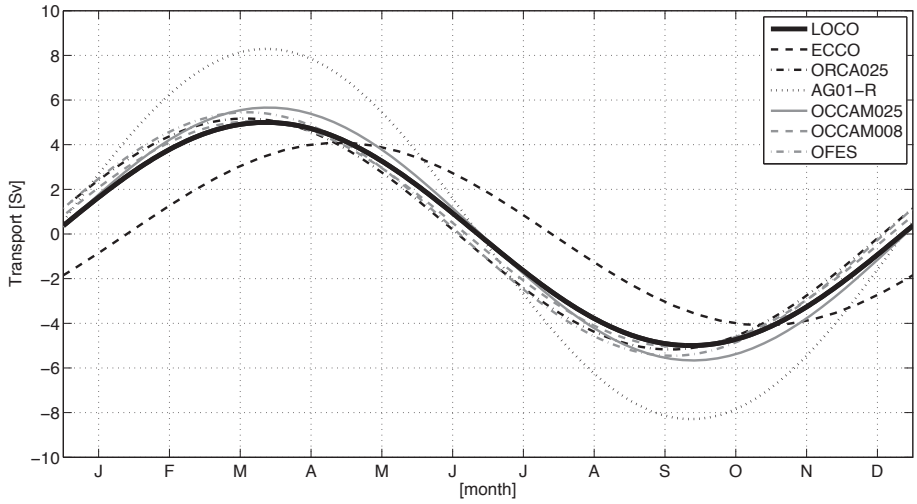

Figure 3.6: *Seasonal cycles of the transport in the observations (LOCO) and the six model runs. The seasonal cycle was obtained by fitting a sine function to the transport time series with a period of one year. The seasonal cycle is quite similar for all data sets. It has a higher amplitude in AG01-R and a phase shift of about one month in ECCO.*

frequency range is very small compared to the observations.

The transport variability benefits somewhat from an investment in the horizontal resolution. Although all models underestimate the variability of the transport, the power spectra of the models with a higher horizontal resolution are slightly closer to that of the observations than that of models with a coarser resolution.

3.3.2 The seasonal cycle

The frequency with the highest spectral density in all of the numerical model runs is $1/y$, the seasonal cycle (Figure 3.4). In all numerical models, this signal is higher than the AR(1) spectrum that was discussed in the previous section. This is in contrast to the observations, where the seasonal cycle is lower than the AR(1) spectrum and is of the same size as the variability at low frequencies ($0.5/y$) and in the $5/y - 6/y$ range. The main reason for this difference is the underrepresentation of the variability at higher frequencies ($f > 1/y$) in the models, which decreases the spectral density of the red noise spectrum at the lower frequencies. This difference is clearly visible in the transport time series (Figure 3.3). No clear seasonal cycle exists in the observations, whereas in each numerical model run a seasonal cycle can be detected by eye in the time series.

To extract the seasonal cycle from each data record, a sine with a period

of one year was fitted to each time series. This method does not discriminate between cycles that are significant (in the models) or insignificant (in the observations). The amplitudes of all the seasonal cycles (Figure 3.5 and 3.6) range between 4.1 Sv (ECCO) and 8.3 Sv (AG01-R). The amplitude of the seasonal cycle in the observations is 5.0 Sv, comparable to those of most numerical models runs. The phases of the cycle in all data sets but ECCO are also similar, with the maximum southward transport in September and the minimum in March. The phase of ECCO is lagged by a month (Figure 3.6).

The seasonal cycle is primarily related to the wind stress pattern in the Indian Ocean. *Matano et al.* (2002, 2008) showed that regional barotropic processes control the seasonal variability in the South Indian Ocean. The origin of the seasonal variability of the transport in the Mozambique Channel should therefore be found west of 75°E (see Figure 3a of *Matano et al.*, 2008), since the barotropic seasonal variability can not cross the Mid Indian Ridge. Applying the linear island rule (*Godfrey*, 1989) on the wind stress west of 75°E gives a seasonal cycle in the Mozambique Channel transport of 4.5 Sv. The lag between the wind forcing and the transport is about a month, consistent with the propagation speed of the seasonal cycle (*Matano et al.*, 2008).

In conclusion, there is indeed a seasonal cycle in the observations, explained by varying upstream wind forcing. A similar seasonal cycle is simulated in the numerical model runs. However, the seasonal cycle in the models is dominant because it is the only frequency which is well resolved. The spectral density at all other frequencies is underrepresented. In contrast, the seasonal cycle in the observations is not dominant, since it is overshadowed by the variability at other frequencies. Hence, the origin of the discrepancy should be sought in the underrepresentation by the models of variability at other frequencies than $1/y$.

3.3.3 The structure with depth

To better understand the difference between the models and the observations at frequencies higher than 1/y, we have repeated the above analysis for the transport at several depth ranges. For example, if the difference between observation and model transport variability would be largest near the surface, then the variability in atmospheric forcing could be insufficient. In contrast, if the difference would be largest in the bottom layers, then the interaction with the bottom topography could be wrongly modelled.

Our results appeared clearest by dividing them into two depth ranges: the transport shallower than 1500 m and that between 1500 m and the bottom. Figure 3.7 shows the standard deviation of the band pass filtered transport of frequencies between $1/y$ and $10/y$, for the two depth ranges. In this frequency

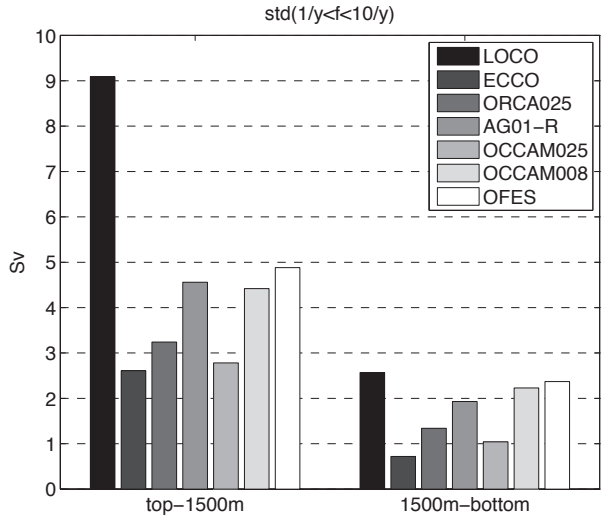

Figure 3.7: *Standard deviation of the transport time series, band filtered between the frequencies of $1/y$ and $10/y$, for the transports shallower (left) and deeper (right) than 1500 m for the observations (LOCO) and the six model runs. The variability at depths shallower than 1500 m is underrepresented in the numerical models.*

band, both the frequency band 5/y – 6/y and 7/y – 9/y are represented. Remarkably, the three high resolution model runs (AG01-R, OCCAM008 and OFES) have about the same standard deviation in the transport deeper than 1500 m as is observed in the observations (1.9 Sv – 2.6 Sv). However, for the depth range above 1500 m depth, the numerical model runs fail to simulate about half of the variability of the observations (4.4 Sv – 4.9 Sv for the three high resolution models vs. 9.1 Sv for the observations). As expected, the high resolution models do better than the low resolution models.

The largest differences between observations and numerical models were observed between 500 m and 1500 m depth (not shown). At this depth, the variability is mainly related to baroclinic Rossby waves and the Mozambique Channel eddies ($5/y$–$6/y$) and most presumably to barotropic instability ($7/y$–$9/y$). Near the surface, the variability is forced by both internal processes and local atmospheric forcing. Variability due to the local atmospheric forcing is quite well resolved by the numerical models, which makes the relative difference between variability in the observations and the models near the surface smaller.

3.4 Focus on the 5/y frequency: eddies and Rossby waves

As pointed out above, the most important variability in the observations is concentrated in the frequency range $5/y - 6/y$ (Figure 3.4), while the spectral density in this frequency range is not particularly well represented by the OGCMs. Moreover, the largest difference between the observations and the models is in the upper layer variability above 1500 m. In this section, we will therefore focus on the typical features that are observed in this frequency range and depth scale: Mozambique Channel eddies and Rossby waves (*Schouten et al.*, 2003; *Harlander et al.*, 2009).

Harlander et al. (2009) studied a series of snapshots of the meridional velocity of an eddy at the LOCO mooring section. As the eddy moves southward, the pattern at the section has a westward phase propagation, suggesting a southwestward direction of the eddy. Then, when the eddy has nearly passed through the section, a southward current is observed at the eastern side of the section, which is moving westward as well. After analysis by empirical orthogonal functions (EOFs) and principal oscillation pattern (POP) analysis, *Harlander et al.* (2009) concluded that this pattern was caused by the superposition of Mozambique Channel eddies and westward propagating Rossby waves. In the following, we use the analysis methods of *Harlander et al.* (2009) to compare the data of the observations with that of the numerical models. Only those numerical models with eddies around 16.5°S (AG01-R, OCCAM025, OCCAM008 and OFES) will be studied.

Figure 3.8 shows the first two EOFs of each of the five data sets. These EOFs were calculated from the meridional velocities from which the seasonal cycle was removed. The time series of these ten EOFs have their main variability in the frequency band $5/y - 6/y$.

As in *Harlander et al.* (2009), the first two EOFs of the observations were identified as the superposition of Mozambique Channel eddies and a westward propagating Rossby wave. EOF2 looks like EOF1, but is phase shifted by $\pi/2$, indicating westward propagation. *Harlander et al.* (2009) explained the main part of EOF1 by a southward propagating anticyclonic eddy, and the remaining part of EOF1 together with the main part of EOF2 as a westward propagating Rossby wave.

The four numerical models show a similar structure of the first two EOFs, although the ratio between the explained variances of EOF1 and EOF2 in the models is slightly lower than in the observations. In OCCAM008, the variance explained by the two EOFs is almost equal. This can partly be explained by the different orientation of the 'mooring sections' in the observations and the

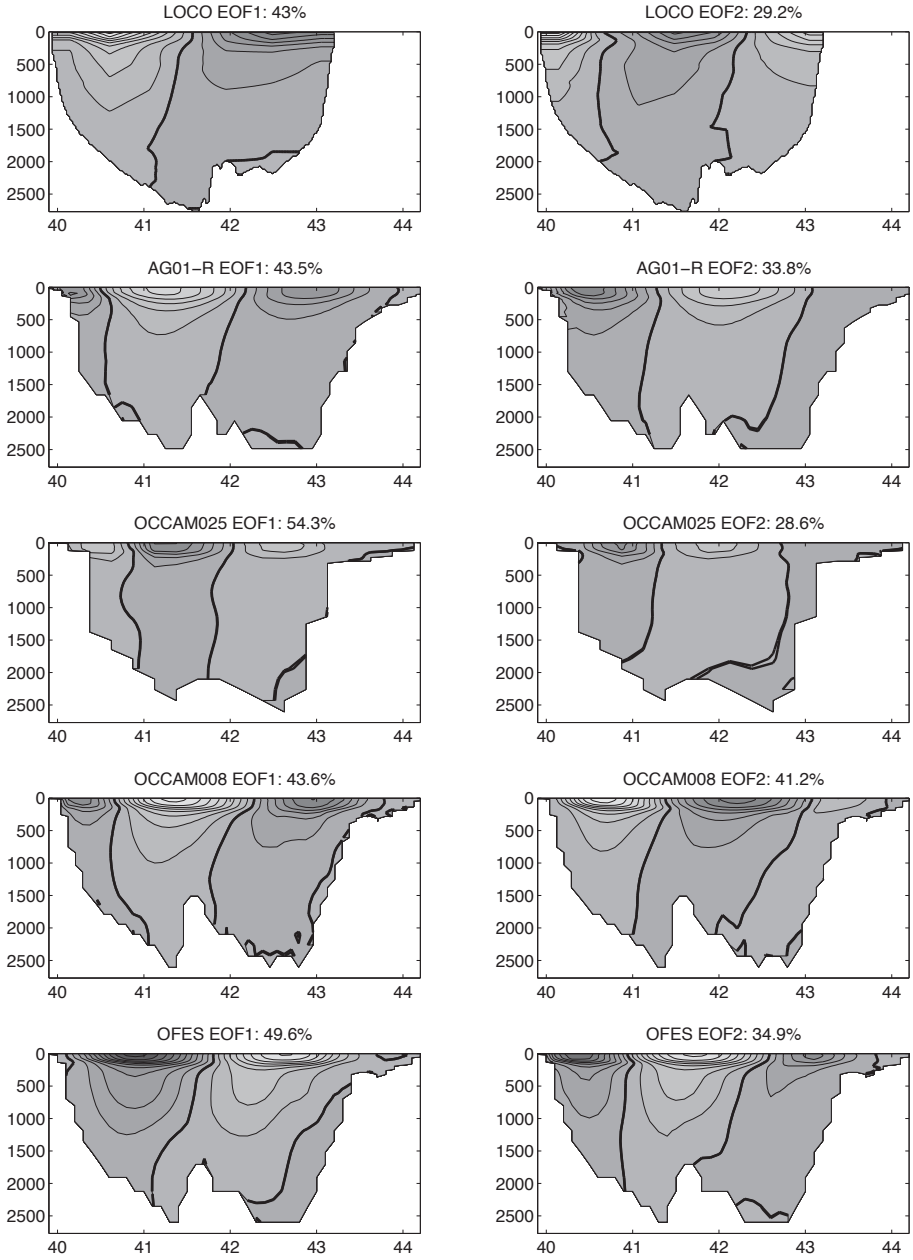

Figure 3.8: *(left) EOF1 and (right) EOF2 for the meridional velocities, of which the seasonal cycle was removed, of the observations (LOCO) and the four numerical model runs which simulate eddies at the mooring section. Contours are drawn every 5 cm/s, and the thick contour denotes the zero-line. The amount of variance explained by each EOF is stated in the heading of each plot.*

models (Figure 3.10). The section of LOCO is tilted slightly in a southeastward direction, while the sections in the models are zonally orientated. From altimetry, it is observed that the eddies pass the section in a southwestward direction. Therefore, their propagation in the models has a small parallel (westward) component to the section. Although one cannot determine it directly from these EOFs which are based on meridional velocities, this extra westward motion is probably captured by EOF2.

The EOF structures of the observations reach depths of 1500 m. The structures in OFES are similarly deep, while the structures in OCCAM025 are very shallow and reach depths of only 280 m. To examine the vertical structure in more detail, a velocity-depth plot has been made of EOF1 (Figure 3.9): for each depth, the mean velocity of EOF1 and the maximum absolute anomaly relative to that mean were determined. If EOF1 can be considered as a pure eddy, this maximum absolute velocity anomaly represents the tangential velocity of an eddy. As mentioned above, this assumption is not completely true, as EOF1 is regarded as the superposition of an eddy with a westward propagating Rossby wave. The tangential velocity is therefore an estimation for all data sets. We did however get qualitatively similar results with individual eddies, and the EOF analysis gives us an estimate over all eddies in the time series.

The thus-obtained eddy structure in the observations consists of two parts: above 380 m depth, the tangential eddy velocity strongly decreases with depth, while deeper than 380 m, the decrease in tangential velocity is much less. The eddies in the observations have a strong barotropic component (also shown in *De Ruijter et al.*, 2002). Near the surface, the tangential velocities of the eddies in the OGCMs range around the observations: eddies in OCCAM008 and OFES are a bit too strong, while eddies in AG01-R and OCCAM025 are a bit too weak. Also at depth, the tangential velocities of the eddies in the models range around the LOCO values. The eddies of the three high resolution models (AG01-R, OCCAM008 and OFES) in particular have tangential velocities at depth that are comparable to that of the observed eddies. This is a major improvement from the former generation models with a lower horizontal resolution, such as OCCAM025, which have eddies that are too much surface intensified and very weak at depth (*Schouten et al.*, 2003). We thus find that the eddy structure in the models can not be the cause of the underrepresentation of the variability in the frequency range $5/y - 6/y$. Related to this, it should be noted that the contribution of a passing eddy to the transport variability is very small. A 'perfect' eddy with a zero translational velocity does not contribute to the total transport; a result which is independent of the tangential velocity. When an eddy is propagating, only the sea level anomaly related to the eddy contributes to the transport variability. An eddy with a sea level anomaly of 30 cm and

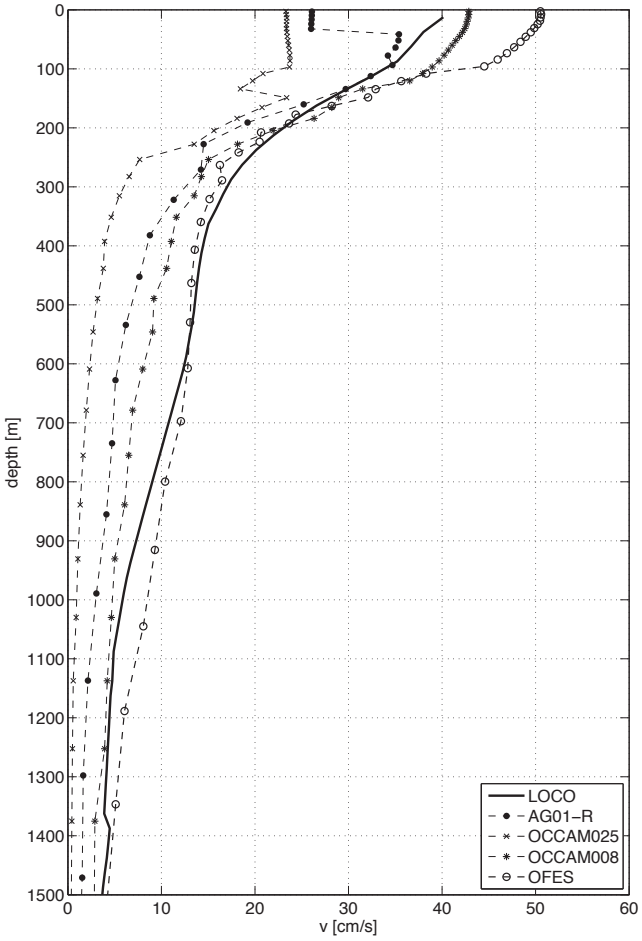

Figure 3.9: *Tangential velocity of eddies in the observations (LOCO – solid line) and the four numerical models with eddies (dashed lines with markers), obtained via EOF analysis (see text for details). The markers indicate the depth levels of the models. The higher resolution models (AG01-R, OCCAM008 and OFES) represent eddies well.*

a propagation speed of 6 km/day (*Schouten et al.*, 2003) contributes an extra 3 mSv to the transport, which can be neglected relative to the total transport variability.

In contrast to the eddy structure, a major difference in the formation area and formation mechanism of the eddies was found between the observations and the models. For the four models and in the observations, four years of eddy paths have been tracked by manually following the positive SSH anomalies through the Mozambique Channel (Figure 3.10). The criteria used for the identification of an eddy were that the eddy should have at least a SSH anomaly of 20 cm and should be relatively circular (ratio of meridional and zonal diameter of less than 3). Only eddies that crossed the section at 16.5°S were taken into account. In addition to the eddy paths, Hovmöller plots of the surface velocities at the mooring section were analyzed (Figure 3.11 and 3.12).

In the observations, most eddies that pass the mooring section are formed relatively close to the mooring section (Figure 3.10-AVISO). Some eddies are formed further north, near the northern tip of Madagascar, but these eddies dissolve north of the mooring section, and are therefore not shown. The mechanism of the formation of eddies in the observations was proposed by *Ridderinkhof and De Ruijter* (2003) and verified by *Harlander et al.* (2009) (also see Figures 3.11-LOCO and 3.12-LOCO): first, a strong southward flow close to the Madagascar coast exists, e.g. at day 80 and 150. This current is a western boundary current flowing along the Northern Mozambican coast, which overshoots at the narrows. The maximum of the southward flow propagates westward, presumably by the interaction with a Rossby wave. Then, a strong anticyclonic eddy develops (days 120 and 170). Also the eddy itself has a small westward propagation (compare the position of the maximal westward flow at day 120 and day 140 in Figure 3.11-LOCO).

The surface flow in the observations is thus characterized by two main structures that alternate: the strong southward current and the eddy formation. Also at the first eddy event in the 200-days LOCO time series the eddy is preceded by a southward current, although this current flows at the western side of the Mozambique Channel (day 30 of Figure 3.12-LOCO). The alternation between current and eddy, which has a frequency of $5.5/y$, results in variability of the transport at the same frequency.

The eddies in the three high resolution model runs (AG01-R, OCCAM008 and OFES) are mainly formed further north in the Channel (Figure 3.10). They propagate with the background flow through the mooring section. Altimetry data suggests that the Rossby waves in these models do not play the same role as in the observations. Instead of facilitating the formation of an eddy, they seem to strengthen the eddy that has already been formed north.

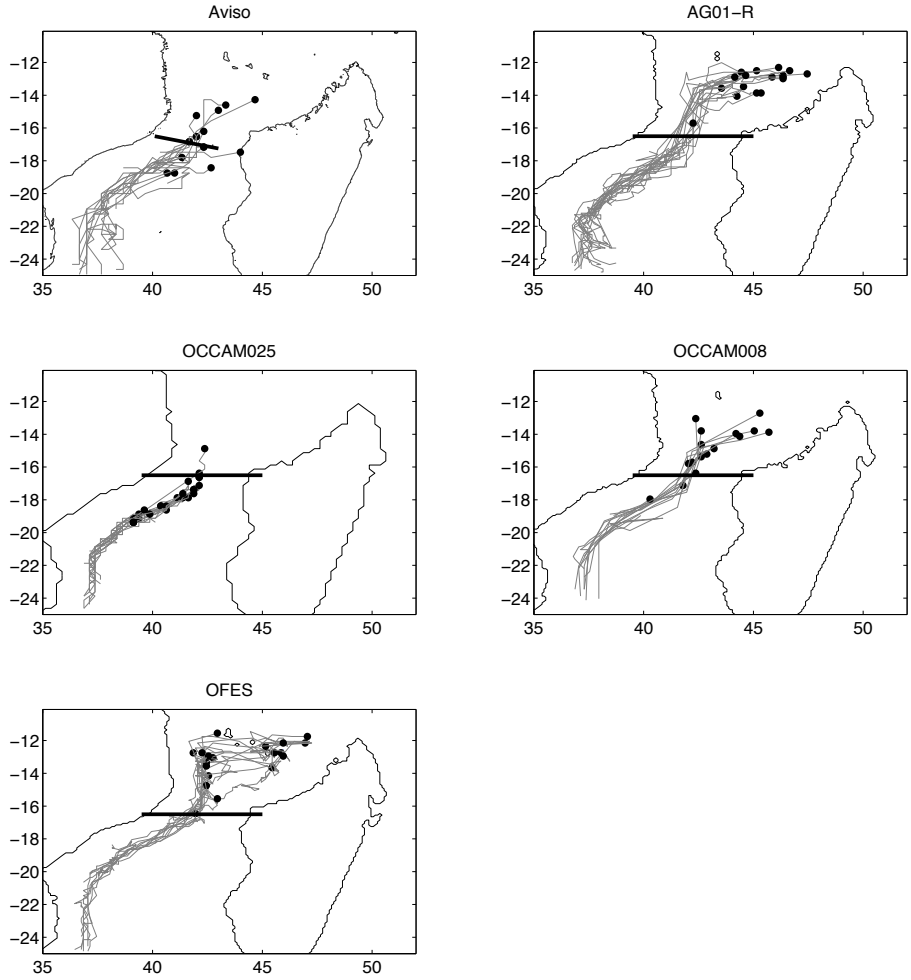

Figure 3.10: *Tracked eddies that pass the mooring section in four years of data for the observations (AVISO: 2004–2007) and the four models with eddies (2001:2004). The black dot denotes the start of each eddy, the gray lines their path, and the black line denotes the measurement section.*

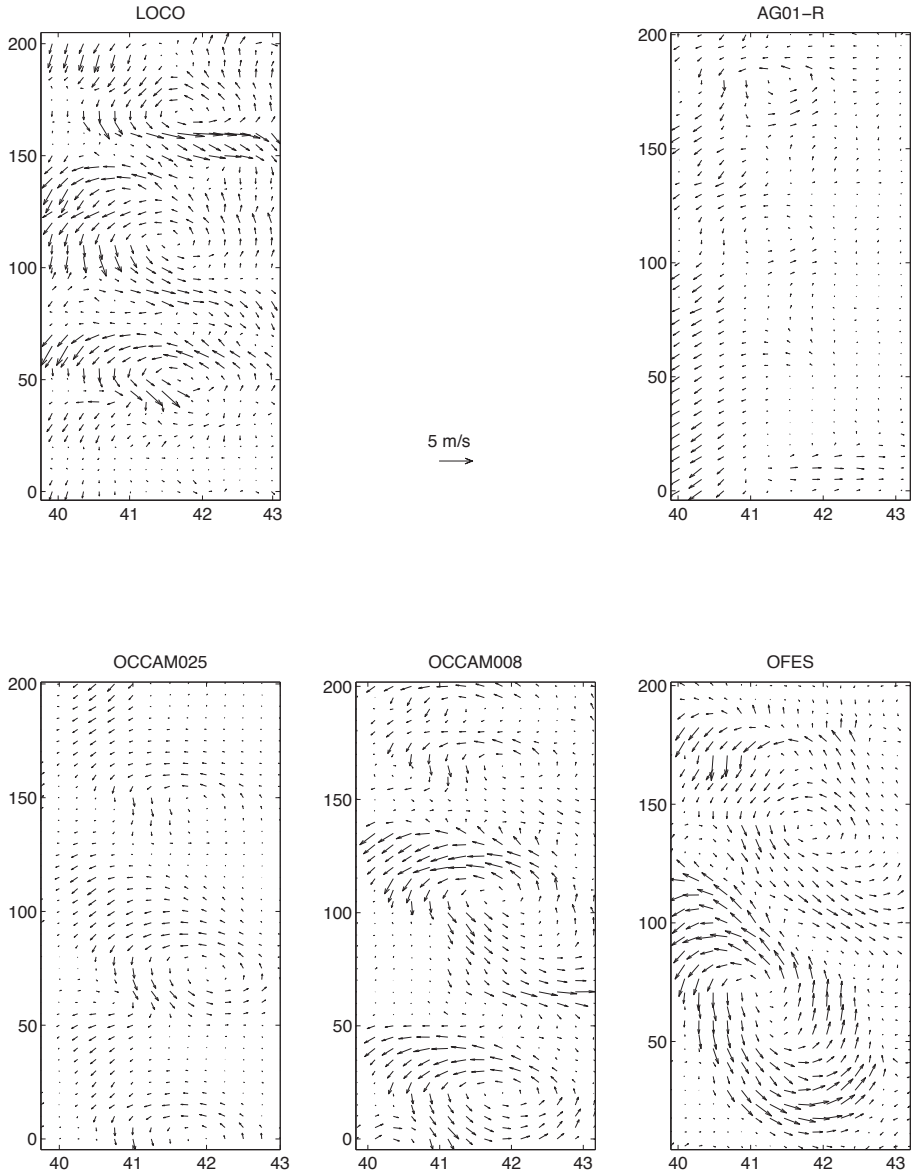

Figure 3.11: *Hovmöller plots over 200 days of the near-surface velocity at the section for each data set containing eddies. Vectors show speed and direction. The first day of the plots is July 18, 2004 (LOCO), December 24, 2001 (AG01-R), January 9, 2001(OCCAM025 and OCCAM008), and March 16, 2001 (OFES). A correspondence between space and time exists under the assumption that the eddy moves by a constant speed while preserving its structure. A more elaborate discussion on these kind of plots can be found in Harlander et al. (2009).*

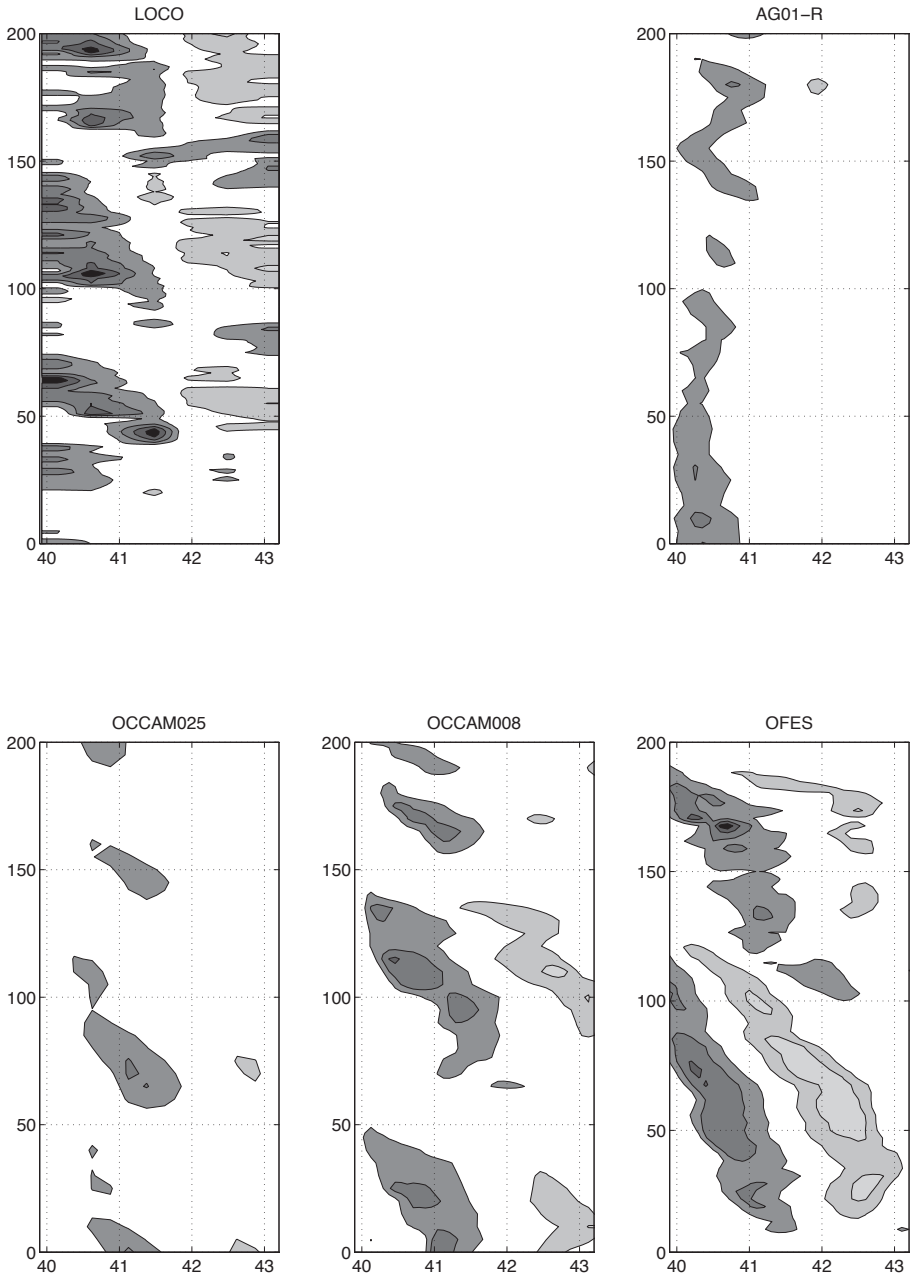

Figure 3.12: *As Figure 3.11, but for meridional velocity only. Contours are plotted every 50 cm/s, the zero line is omitted and darker (brighter) colors denote southward (northward) flow. The Hovmöller plot of the observations clearly shows an alternation between southward currents and eddies; such an alternation does not exist in the models.*

They also provide the eddies with westward momentum and bend their path from southward to southwestward. In the lower resolution model OCCAM025, the eddies are formed at the mooring section, like in the observations, but without the interaction with a Rossby wave (Figures 3.11-OCCAM025 and 3.12-OCCAM025). Moreover, instead of occupying the whole section, they are small disturbances in the background flow.

In all four numerical model runs, there is no alternation at the mooring section between currents and eddies (Figure 3.11 and 3.12). For AG01-R and OCCAM025, eddies are seen at days 30, 120 and 180 (AG01-R) and days 0, 70 and 120 (OCCAM025). These eddies are only small disturbances in the background flow, which is a southward current at the western side of the Mozambique Channel. As the effective transport of an eddy moving with the background flow is close to the transport of the background flow, the resulting transport time series does not have strong variations in the eddy frequency range ($5/y - 6/y$). In OCCAM008 and OFES, only eddies pass the mooring section, as is clearest seen in Figure 3.12. The eddies in OFES seem to be moving slower through the section as in the other data sets, but this does not influence the transport variability. Around day 110 in the OFES data, a southward current is seen east of the previous eddy. However, the zonal mean velocity at the surface is very steady, around 5 cm/s, because at the same time a northward current flows west of the southward current. Again, there is no alternation between southward currents and eddies, which results in a quite continuous transport as well.

3.5 Discussion

The power spectrum of the Mozambique Channel transport in numerical models could be greatly improved when the formation mechanism and formation location of the eddies is corrected. Why the eddies in the OGCMs passing the mooring section are formed at the wrong location is not precisely understood at this moment. Both in the observations and in the high resolution models, eddies are formed near the northern tip of Madagascar. However, in the observations, these eddies decay and new eddies are formed at the mooring section, while in the numerical models, they propagate through the mooring section. This difference in behavior could be caused by the representation of the bottom topography, with which the eddies interact. For example, the path of the eddies is through the Comores. This island group is not well represented by the OGCMs. In reality, it consists of four major islands (diameter larger than 5 km). OCCAM008 and AG01-R only have one island representing the Comores. In OFES, all four islands can be identified, but they consist of only a

few grid points. Deeper down, AG01-R has a better bottom topography, but in OCCAM008 the gaps between the three westernmost islands is almost closed, while the gap in reality is about a quarter degree (which would be a distance of three instead of one grid cell for OCCAM008). Nevertheless, the bathymetry close to the Comores is very steep, and the interaction of eddies with this island group might therefore not be correctly simulated by the OGCMs.

It is not clear to what extent the location of the LOCO mooring section influences the power spectrum of the transport. As pointed out above, the strong signal at $5/y - 6/y$ in the observations is mainly due to the formation of eddies close to the section and therefore the alternation between southward currents and eddies. Further south, this alternation may not be present, as the eddies propagate in and with the background flow. However, there are no transport observations to measure the strength of the $5/y - 6/y$ signal south of the eddy formation area.

In a sensitivity study to the mooring section location in the numerical models, two extra transport time series at different latitudes (14°S and 20°S) have been extracted from the OCCAM008 data. The power spectra of these two transport timeseries were not significantly different from the model spectrum at 16.5°S. The formation of eddies in the numerical models north of the mooring section is different from the formation of eddies in the observations. Therefore, we might expect that the power spectrum of the transport near the formation area of eddies in the numerical models will be different from that of the observations.

Apart from the six model runs described above, the analysis was also carried out with data from a four-year run with the Parallel Ocean Program (POP) model (1/10° horizontal resolution and daily output, *Dukowicz and Smith*, 1994; *Maltrud and McClean*, 2005). This run was forced by monthly climatological atmospheric forcing, which includes only a part of the atmospheric forcing variability of the other OGCMs. Therefore, it was not taken into account in the full analysis. Nevertheless, similar results were obtained. The mean southward transport through the Mozambique Channel in POP is 14.6 Sv with a standard deviation of 5.2 Sv. Its seasonal cycle has an amplitude of 5.4 Sv, which is of the same size as the standard deviation. As in the other numerical models, the seasonal cycle exceeds the AR(1) spectrum, while the variability at frequencies higher than 1/y is underrepresented. The conclusions drawn in this paper are thus independent of the atmospheric forcing.

The second main frequency range of which the spectral density in the transport of the observations is significant, is the range $7/y - 9/y$ (Figure 3.4). Spectral density in this range can be associated with barotropic instability at the northern tip of Madagascar (*Quadfasel and Swallow*, 1986; *Schott et al.*,

1988a; *Biastoch and Krauss*, 1999; *Schouten et al.*, 2003). The shear leading to this instability is very strong. The along-coast velocity increases from zero at the coast to 1 m/s at 30 km offshore (*Swallow et al.*, 1988). Such a narrow boundary layer may not be fully resolved by numerical models with a 1/10° resolution. It has been shown that models do solve the barotropic instability (e.g. *Biastoch and Krauss*, 1999), but they might not resolve all the energy at this frequency that is observed in the observations. This might explain why the spectral density in this range in the numerical models is less than in the observations.

3.6 Conclusions

In this study, we analyzed the temporal variability of the observed transport through the Mozambique Channel and compared it to transports simulated by six ocean general circulation model runs. An important difference between the observations and the numerical models regards the dominance of the seasonal cycle. This signal is relatively weak in the observed transport, while it is dominant in the numerical model transport. However, the seasonal cycles of the observations and numerical models are similar in strength and phase. The cycle can be explained by the yearly variation of the wind forcing in the Indian Ocean west of 75°E. Thus, a seasonal cycle in the Mozambique Channel transport does exists and has an amplitude of 5 Sv.

The seasonal cycle in the models is dominant because the spectral density at other frequencies is not well represented. Main deviations from the observations were found at depths shallower than 1500 m and in the $5/y - 6/y$ frequency range.

The three high resolution models (AG01-R, OCCAM008 and OFES) simulate the Mozambique Channel eddy structure quite well; the barotropic component of the eddies in these models was stronger and closer to eddies in observations than in the lower resolution model OCCAM025 and previous studies (*Schouten et al.*, 2003). However, in all models, the formation mechanism of the eddies was found to be different from that in observations. Research by *Ridderinkhof and De Ruijter* (2003) and *Harlander et al.* (2009) suggests that eddies in the observations are frequently formed from an overshooting current near the mooring section in combination with a Rossby wave. This causes an alternation of events at the mooring section, varying between a strong southward current and the formation and passing of an eddy. This alternation results in a variation of transport in the frequency range of $5/y - 6/y$. In the models, on the other hand, the eddies are formed further upstream and they propagate symmetrically through the section. Altimetry data suggests that the Rossby

waves in the models strengthen the eddies that have already been formed and do not play a role in their formation. No alternation similar to the observations was found, which results in a more constant transport in the models.

Our results have implications for the use of numerical model output in the South West Indian Ocean. The time-mean dynamics of the system seems to be well resolved by the numerical models, as is the eddy structure in the high resolution models. Studies with numerical models that only use these characteristics should therefore not encounter problems. For example, *Biastoch et al.* (2008b) did a sensitivity experiment to whether Mozambique Channel eddies influence the interocean exchange in the Agulhas system. In that study, it was not relevant where the Mozambique Channel eddies were formed, but their strength should be close to observations, as should the amount of Mozambique Channel eddies per year.

On the other hand, the wrongly estimated formation area of the eddies could have implications for the water masses that are trapped by the eddies. Also, studies involving local biology or sediment transport should be careful in applying these numerical models.

4

Observation and Origin of an Interannual Salinity Anomaly in the Mozambique Channel

A positive salinity anomaly of 0.2 PSU was observed between 50 and 200 m depth over the years 2000 – 2001 across the Mozambique Channel at a section at 17°S, which was repeated in 2003, 2005, 2006 and 2008. Meanwhile, a moored array is continued from 2003 to 2008. This anomaly was most distinct showing an interannual but nonseasonal variation. The possible origin of the anomaly is investigated using output from three ocean general circulation models (ECCO, OCCAM and POP). The most probable mechanism for the salinity anomaly is the anomalous inflow of subtropical waters, caused by a weakening of the northern part of the South Equatorial Current by weaker trade winds. This mechanism was found in all three numerical models. In addition, the numerical models indicate a possible salinization of one of the source water masses to the Mozambique Channel as an additional cause of the anomaly. The anomaly propagated southward into the Agulhas Current and northward along the African coast.

This chapter is based on:
Van der Werf, P. M., M. W. Schouten, P. J. Van Leeuwen, H. Ridderinkhof, and W. P. M. De Ruijter. Observation and origin of an interannual salinity anomaly in the Mozambique Channel. *J. Geophys. Res., 114*(C03017), doi:10.1029/2008JC004911, 2009.

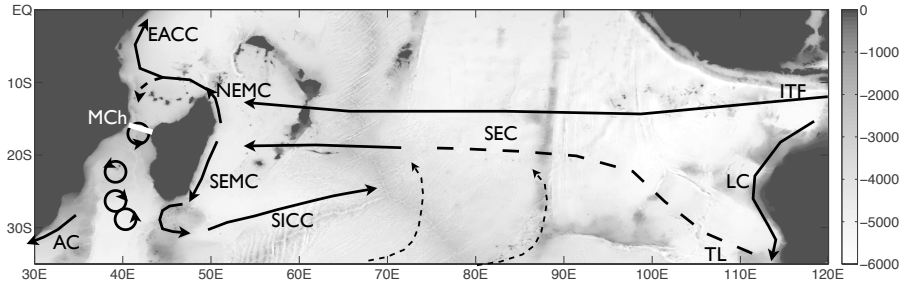

Figure 4.1: *Main currents of the Southern Indian Ocean: Indonesian Throughflow (ITF), Leeuwin Current (LC), Tasman Leakage (TL), South Equatorial Current (SEC), Northeast and Southeast Madagascar Currents (NEMC and SEMC), East African Countercurrent (EACC), South Indian Ocean Countercurrent (SICC) and Agulhas Current (AC). The Mozambique Channel (MCh) and the LOCO mooring section are drawn in white.*

4.1 Introduction

The circulation around Madagascar is characterized by its high variability (*DiMarco et al.*, 2002; *Quartly and Srokosz*, 2004; *De Ruijter et al.*, 2005; *Hermes et al.*, 2007). The main inflow into this area is from the South Equatorial Current (SEC), which impinges on the island from the east between $10° - 20°$S (Figure 4.1). There, it bifurcates into a northward and southward branch, being the Northeast and Southeast Madagascar Currents (NEMC and SEMC), respectively. The northward branch follows the northeast coast of the island and flows westward towards the African coast, where it bifurcates once more. Part of the flow of the SEC thus enters the Mozambique Channel. Observations have shown that the flow in the Mozambique Channel consists of a train of eddies, rather than a continuous current (*De Ruijter et al.*, 2002; *Ridderinkhof and De Ruijter*, 2003, and Chapters 2 and 3). In the southern part of the Channel, the eddies from the Mozambique Channel meet with the highly variable flow from the Southeast Madagascar Current, and move into the Agulhas Current. At the retroflection of the Agulhas Current, some of this water moves into the overturning circulation of the Atlantic Ocean (*De Ruijter et al.*, 1999; *Gordon*, 1986; *Biastoch et al.*, 2008a).

In the previous chapters, the variability of Mozambique Channel *transport* was described. In this chapter, on the other hand, the focus will be on variability of the *water mass characteristics*. Monitoring and understanding the variability in heat and salinity content is important to the overturning circulation of the Atlantic Ocean. Because the Mozambique Channel is one of the sources of the Agulhas Current, this variability probably propagates to the heat and salinity content of the inter-ocean exchange (*Beal et al.*, 2006; *Van Sebille*

et al., 2009c).

Again, measurements from the Long-term Climate Observations (LOCO) program (see Figure 4.1 for its location) will be used to study the variability. For this, conductivity-temperature-depth (CTD) meters have been fitted at the moorings (Figure 4.2). One of these moorings has been fitted with three CTD meters in the upper layers. In addition to the moored instruments, six hydrographic sections have been taken at this location in the period 2000 to 2008.

A positive salinity anomaly has been observed in the upper layers of the Mozambique Channel in the years 2000 and 2001. In this chapter, we will present and discuss the observations of this anomaly and its possible origin.

The waters in the Mozambique Channel consist of a mixture of different water masses. The observed anomaly in the salinity content of the mixture could be caused by either an increased salinity of one of the source waters, or a change in the mixing ratio of these source waters. The main source waters of the upper layers of the Mozambique Channel are the Subtropical Surface Water (STSW), the Tropical Surface Water (TSW) and the Indonesian Throughflow Water (ITFW).

The STSW is formed by strong evaporation between $25°-35°$S, and subducts below the fresher waters in the north (*Wyrtki*, 1973; *Karstensen and Quadfasel*, 2002a). The salinity maximum decays northward, but remains clearly distinguishable due to southward Ekman transport of fresher tropical waters in the upper layer (*Song et al.*, 2004). *Schouten et al.* (2005) described a seasonal variation in the source waters of the northern part of the Mozambique Channel, that oscillates between STSW and TSW.

The ITFW signal is found along a zonal band across the basin ($10° - 15°$S, *Wyrtki*, 1971; *Gordon*, 1986). The deeper component of the throughflow has also been traced along a zonal trajectory across the basin (*Talley and Sprintall*, 2005), but has not been identified west of the Mascarene ridge around 60°E. Nonetheless, the characteristics of the ITFW have their imprint on the water mass characteristics all over the South Indian Ocean thermocline (*You and Tomczak*, 1993; *You*, 1997).

In the recent past, several studies were concerned with salinity variations of water masses in the Indian Ocean. Firstly, *Bryden et al.* (2003) and *McDonagh et al.* (2005) report on a freshening of the upper thermocline along 32°S before 1987 and a salinization afterwards. Secondly, during El Niño (La Niña), the precipitation above the Indonesian Seas is below (above) average, causing a salinization (freshening) of the ITFW (*Phillips et al.*, 2005). Lastly, *Nauw et al.* (2006) observed two anomalously salty intrathermocline eddies in the boundary current southeast of Madagascar, that originated from the southeast

Indian Ocean.

A change in mixing ratios of the source waters can be caused by wind variations. A prominent example is the latitudinal variation of the SEC caused by the Indian Ocean Dipole (IOD, *Saji et al.*, 1999; *Webster et al.*, 1999; *Palastanga et al.*, 2006). During an IOD+, the SEC is shifted to the north and more relatively saline water from the subtropical gyre can enter the Mozambique Channel. On the other hand, during an IOD-, the SEC is shifted to the south and more relatively fresh water (TSW and ITFW) can enter the Channel.

Mixing ratios can also change further upstream. For example, the transport of the Indonesian Throughflow is reduced during El Niño's (*Gordon et al.*, 1999; *Phillips et al.*, 2005; *Susanto et al.*, 2001; *Vranes et al.*, 2002).

The aim of the present chapter is to describe the observed salinity anomaly and determine its origin. In section 4.2 the observations of the salinity anomaly in the Mozambique Channel are described. The observational data show that the anomaly is an interannual phenomenon that is not caused by local forcing. Because of a lack in temporal and spatial resolution of measurements in the Indian Ocean, we have to make use of numerical models to determine the origin. These models are the Estimating the Circulation and Climate of the Ocean (ECCO) model, the Ocean Circulation and Climate Advanced Modeling (OCCAM) model, and the Parallel Ocean Program (POP) model. These three models were chosen, because their salinity fields in the Mozambique Channel were similar to the observations and their data spanned a sufficiently long period. In section 4.3, the models are introduced and their salinity time series in the Mozambique Channel are studied. Then, the sources and path of the anomaly will be studied using the numerical models in section 4.4. We will conclude with a summary and discussion of our main results.

4.2 Observations

Measurements of salinity, temperature, and velocities at different depths in the Mozambique Channel have been carried out both by a moored array and by a six-times repeated hydrographic section at the location of the moored array. This moored array is placed across the Mozambique Channel at its narrowest section around 17°S (Figure 4.1).

During deployment and recovery of the mooring array, six hydrographic sections over the full width of the Channel were made. In the years 2000 and 2001, the section was sampled in March/April from aboard RV Pelagia, whereas in 2003 the moorings were serviced in November utilizing the RRS Charles Darwin. In February/March 2005 and in March/April 2006 the section was revisited by RRS Discovery. The last sampling of the section was in

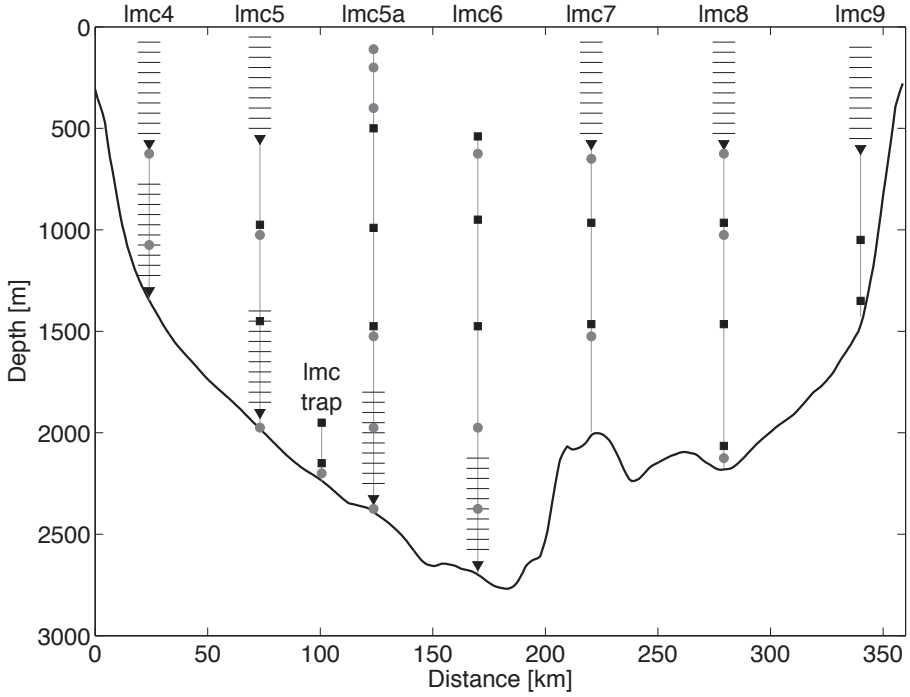

Figure 4.2: *Mooring configuration in the LOCO program (November 2003 – January 2008). Shown are current meters (black squares), ADCPs (triangles; profiling range marked by horizontal stripes) and CTD meters (dark gray dots). Mooring 5A has been fitted with three CTD meters in the top 500 m.*

January/February 2008 by the RV Meteor.

In the period between the 2003 and 2008 occupations of the section, continuous observations of temperature and salinity were made by 22 Seabird 37-SM CTD sensors attached to the moorings (Figure 4.2). These observations allow us to assess the water mass characteristic variability on shorter time scales than allowed for by the hydrographic sections, and to verify how much of the observed interannual differences should be attributed to shorter time scales, e.g. those associated with the passage and formation of Mozambique Channel eddies.

Three CTD-sensors were located in the upper layers, at nominal depths of 100, 200 and 400 m in the top part of mooring 5A located in the central part of the Channel near 41.1°E. Vertical motion of the moored instruments is considerable (downward excursions up to 100 m are recorded), due to the strong currents in the Channel. Combined with the vertical motion of the isopycnals associated with the passage of Mozambique Channel eddies, the three sensors cover most of the upper 400 m density range.

Results of the six occupations and the moored array are summarized in Figure 4.3. Large differences in T/S characteristics between the six occupations of the section (lines) are readily observed. Averaged on levels of potential density (σ_0) the first two years (2000 and 2001) are more saline than the last four years by over 0.2 PSU in the upper 200 meters. Except for the very fresh waters found in 2001 in the uppermost 50 m, the first two profiles (2000 and 2001) are very similar. Their maximum salinity is situated at 130 m depth. Between 100–200 m, the 2003, 2006 and 2008 thermoclines were significantly warmer and fresher, with a sharp salinity maximum at 200 m depth. In 2005, a similarly fresh thermocline is observed, with a salinity maximum at 170 m depth.

The anomaly is maximal around the $\sigma_o = 24.5$ level, which has a climatological depth between 125 m and 150 m (Figure 4.4b). The anomaly is therefore well covered by the continuous CTD measurements at the moorings within the period November 2003 – January 2008. The moored measurements are spaced around the last four hydrographic measurements (2003–2008, Figure 4.3), and are overall much fresher than the first two years. The fresher branch is climatologically more 'normal' (Figure 4.4). We cannot completely rule out the possibility that the two more saline sections (2000/2001) were unrepresentative of the period in between these sections, but it is clear from the continuous observations over 2003–2008 that the 2000 and 2001 sections were anomalously saline with respect to the complete period 2003–2008. This indicates that the measurement of the high salinity in 2000 and 2001 was not the product of the sampling in different seasons. Moreover, the hydrographic section taken in 2006

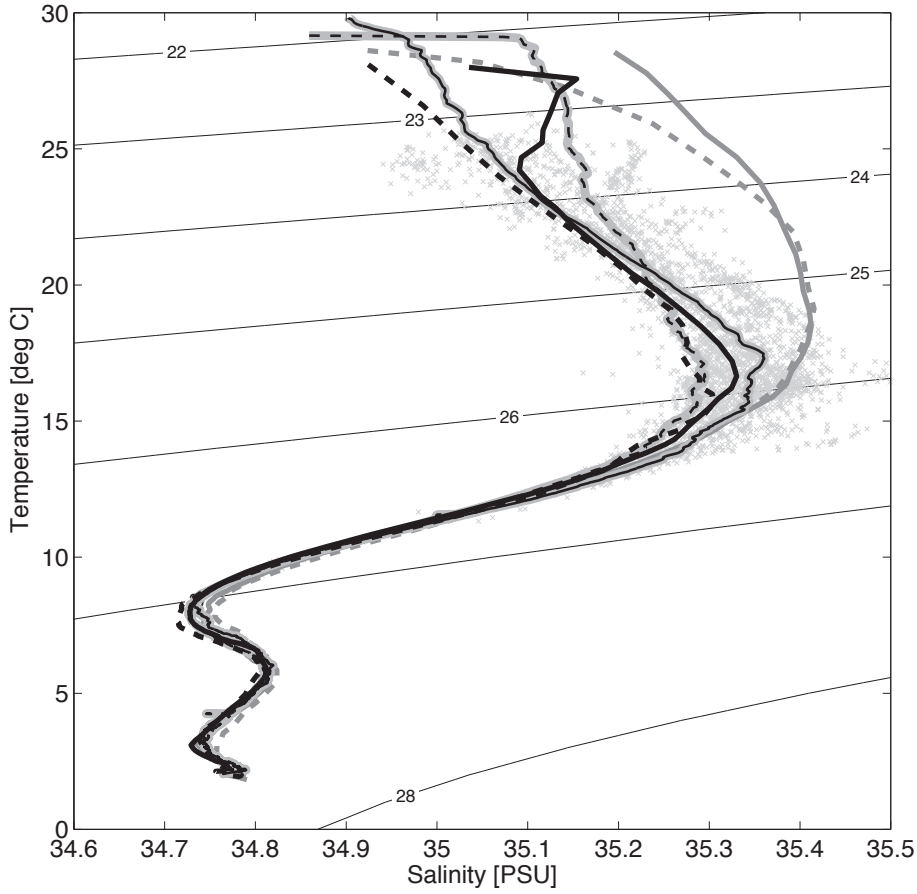

Figure 4.3: *Six section-averaged (T,S)-curves of the years 2000 (solid gray), 2001 (dashed gray), 2003 (solid black), 2005 (dashed black), 2006 (solid black overlying gray), and 2008 (dashed black overlying gray line) overlying daily averages of (T,S) measured continuously at mooring 5A (Figure 4.2) between November 2003 and January 2008 (light-gray markers) by CTD sensors at 100 m, 200 m and 400 m. The thin, curved lines in the figure denote isopycnals. The (T,S)-curves of 2000 and 2001 are much more saline in the upper layers.*

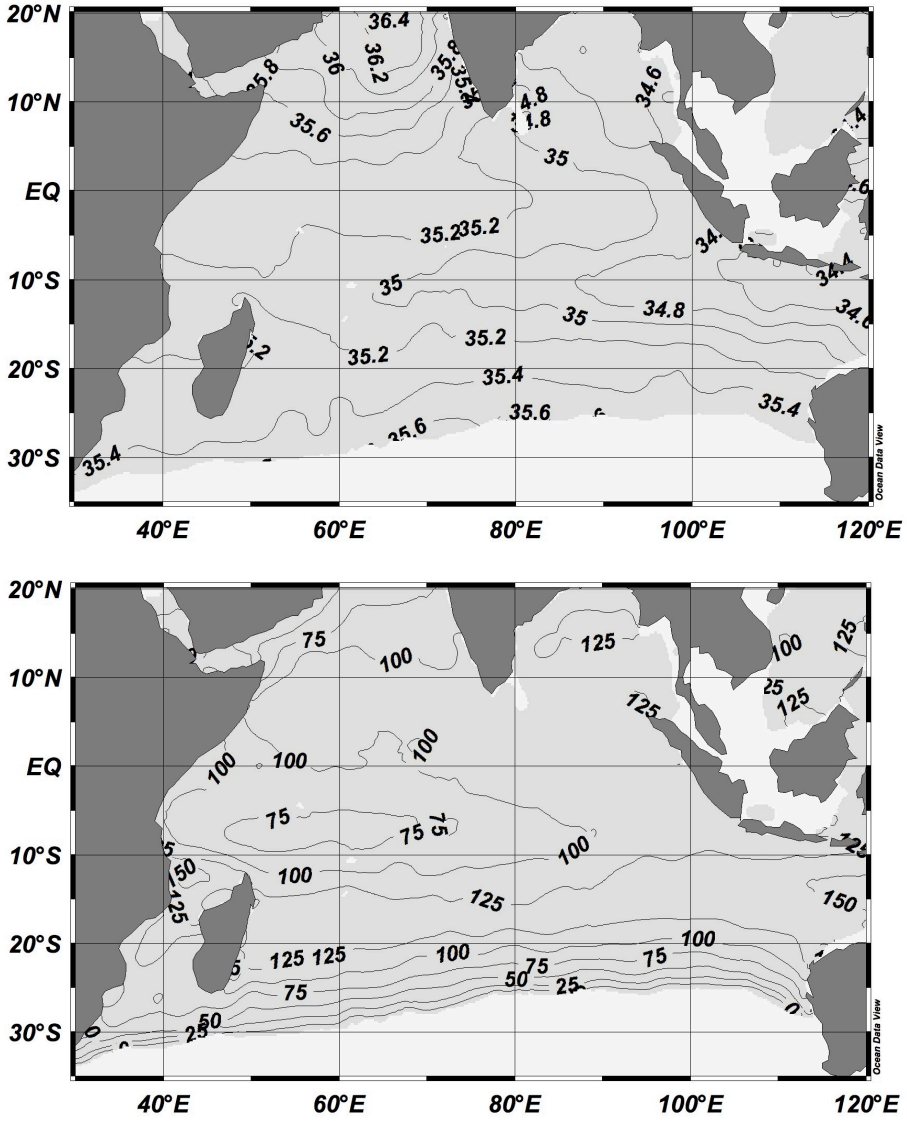

Figure 4.4: *(upper panel) Salinity at the 24.5 isopycnal layer. (lower panel) Depth of this isopycnal layer. Annual mean climatological data were extracted from the World Ocean Atlas 2001 (Conkright et al., 2002).*

took place in the same season as those taken in 2000 and 2001.

This is quite a surprising result, because of the strong seasonality in regions close to Madagascar due to the monsoon variation. However, even in individual CTD recordings at the moorings, there was no seasonal cycle observed.

The anomaly was also not caused by local rainfall. Although the net precipitation in 2000 was anomalously low, in the austral summer of 2001 the rainfall in the northern part of the Mozambique Channel was anomalously high. This resulted in the very fresh waters in the uppermost 50 m of 2001, but had no influence on the salinity at the depth of the anomaly, which is below the mixed layer.

In addition, no correlation has been found between the 2000–2001 salinity anomaly and the local background flow. An anticyclonic Mozambique Channel eddy was observed during the survey of 2000, while in 2001 a cyclonic anomaly was present.

In summary, it is concluded that the anomaly is an interannual phenomenon that originated upstream in the Indian Ocean.

Inspection of the annual mean salinity distributions from the World Ocean Atlas 2001 (*Conkright et al.*, 2002) gives a clue about the background of the observed differences. In particular, we are interested in the isopycnal surface at $\sigma_o = 24.5$, where the largest salinity difference between the 2000 and 2001 hydrographic sections and the 2003–2008 period is observed (Figure 4.4). The observed salinities at that isopycnal level over the four year continuous observational period ($S \approx 35.2$ PSU) are close to climatological values for the SEC region near the northern tip of Madagascar from where most of the water entering the Mozambique Channel is likely derived. The years 2000 and 2001 appear anomalously saline, with salinities corresponding to those found in the subtropical gyre further south ($S \approx 35.4$ PSU, Figure 4.4a). An explanation for the anomalously high salinities in the upper thermocline of the Mozambique Channel may therefore be found in anomalously large inflow of subtropical water from that source.

4.3 Analysis of the anomaly in numerical models

Since there is not enough observational data, the output of three ocean general circulation models is studied: the Estimating the Circulation and Climate of the Ocean (ECCO) model, the Ocean Circulation and Climate Advanced Modeling (OCCAM) model, and the Parallel Ocean Program (POP) model.

The ECCO configuration used is the one used for a quasi-operational analysis (*Menemenlis et al.*, 2005). The model is based on the MITgcm (*Marshall et al.*, 1997). Its output is available on http://ecco.jpl.nasa.gov/, of which the

data set with Kalman Filter assimilation is studied. This data set starts in 1993 and ends in 2005 with a 10 day output interval. It has a zonal grid spacing of 1° and a meridional grid spacing increasing from 1/3° within 10° of the equator to 1° poleward of 22°N/S. This coarse resolution implies that the observation section at 17°S is represented by only 5 grid cells in the horizontal. There are 46 levels in the vertical direction, with a vertical resolution of 10 m in the top 150 m. Atmospheric forcing was applied by 12-hourly wind stress and daily heat and freshwater fluxes from NCEP (*Kistler et al.*, 2001). More information about this model run and the assimilation can be found in *Menemenlis et al.* (2005).

The OCCAM model (*Webb et al.*, 1998; *Coward and de Cuevas*, 2005) was derived from the Bryan-Cox-Semtner general ocean circulation model. In this study, we analyzed the output of model run 103 (available at http:// www.noc.soton.ac.uk/ JRD/OCCAM/ EMODS/select.php), which is equal to the OCCAM025 data set studied in Chapter 3. The run is spanning the period 1989 to 2005. It has a 5-day-mean output, a horizontal resolution of 1/4° and 66 layers in the vertical direction, with 14 layers in the top 100 m. Since the run was started from 1985 from Levitus temperature and salinity and zero velocity and thus had a shortened spin up (personal communication, B. A. de Cuevas), the first years of the output (1989–1992) could not be used for analysis. Therefore the data set stretches from January 1993 to December 2004. Atmospheric forcing was applied by NCEP 6-hourly forcing (*Coward and de Cuevas*, 2005).

The POP model (*Dukowicz and Smith*, 1994) was also derived from the Bryan-Cox-Semtner code. The model has a 1/10° horizontal resolution and 40 layers in the vertical, with 9 layers in the top 100 m. The data set stretches from 1994 to the end of 2003 and has a monthly mean output. Also for this run, the atmospheric forcing was applied by NCEP (daily). A more detailed description of this model run can be found in *Maltrud and McClean* (2005).

The area studied in all the models stretches from $30° - 110°$E and from the equator to 35°S. Most of the analysis was performed in the top 1000 m. Since the salinity anomaly in the observations was shown to be an interannual phenomenon (Section 4.2), we have conducted all analysis of the numerical models after yearly smoothing of the data sets, which emphasizes the interannual variations.

Section averaged salinity time series from the numerical models at the section in the Mozambique Channel (17°S, Figure 4.1), show qualitatively similar results to the observations. All three models show an anomaly around the years 2000 and 2001 (Figure 4.5). The amplitude of these anomalies is a bit smaller than in the observations, in the order of 0.1 PSU. This is partly due to the

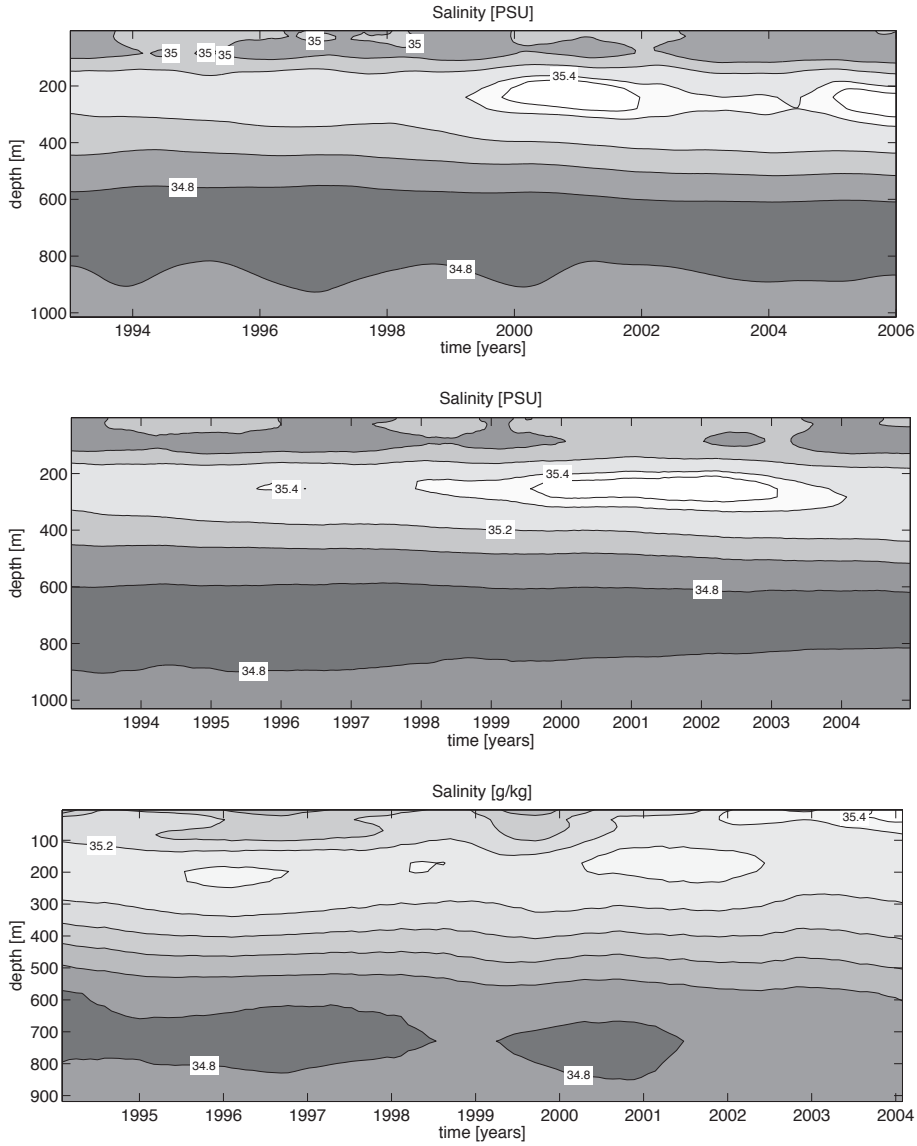

Figure 4.5: *Section averaged salinity at 17°S in the Mozambique Channel (Figure 4.1) in ECCO (top panel), OCCAM (middle panel) and POP (bottom panel). Contours are drawn every 0.2 PSU and at 35.45 PSU for ECCO and OCCAM, and every 0.1 g/kg for POP. In ECCO, a salinity anomaly is seen in the layer of maximum salinity (around 240 m depth) from the end of 1999 to the end of 2001. A second anomaly starts around the same depth in 2005. In OCCAM, a salinity anomaly is seen in the layer of maximum salinity (around 253 m depth) from 2000 to the end of 2002. In POP, three salinity anomalies are seen in the layer of maximum salinity. The anomaly that stretches from 2000 to March 2002 has its core at 171 m depth.*

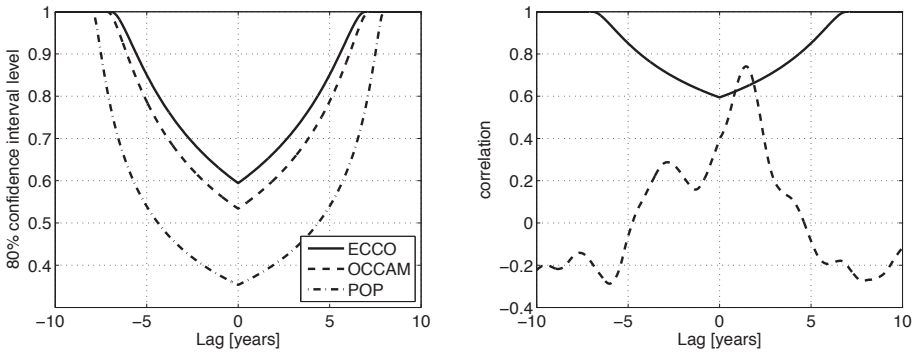

Figure 4.6: *Left: The 80% confidence levels for the three models as a function of the lag in a correlation. Correlations smaller than these confidence levels are considered insignificant and are not taken into account in further analysis. Right: Example of the correlation function between the salinity time series at 12° S, 70° E and the reference time series in ECCO (dashed line). The correlation is only significant when the correlation exceeds the 80% confidence level (solid line), which is for lags between 0.8 and 1.8 years in this example.*

high diffusivity in the models and to the time smoothing of the signals. The depth of the anomalies in the three models is respectively 240 m, 253 m and 171 m for ECCO, OCCAM and POP, which are all in the layer of maximum salinity. The anomalies in the models are thus a bit deeper than in the observations. However, the anomalies in the observations and in the models are all situated well below the mixed layer. As in the observations, the anomalies in the numerical models are interannual phenomena. Their origin may therefore be found in interannual, large-scale variations in the Indian Ocean.

In view of the similarities between the observations and the models, and despite the somewhat deeper level of the anomalies in the models, we assume the anomalies in the models of similar nature as the anomalies in the observations.

4.4 Path of the anomalies in the models

The source areas of the anomaly were traced by a method based on correlation functions, which is explained below by using the results from ECCO. First, the ECCO-simulated data of layer 20 (240 m depth) from the section averaged salinity time series across the Mozambique Channel (described above) is selected as reference time series. This layer was chosen, because it intersects the center of the anomaly.

This salinity time series is then correlated to the time series of several variables at all the grid points of the domain. In this study, focus has been on the salinity and zonal and meridional velocity time series. A positive correlation

with the salinity time series indicates that the increase of salinity of one of the source waters could be the origin of the salinity anomaly in the Mozambique Channel. On the other hand, a correlation with the velocity time series indicates a changing transport of source waters. First, the salinity field in ECCO will be analyzed.

At each grid point in the domain, a correlation function is derived. Only those parts of the correlation functions that have coefficients higher than the 80% confidence interval level are included in the analysis. This significance level has been calculated following *Bendat and Piersol* (1986). We have computed the number of independent variables as the ratio of the total number of data points in the time series to the number of points between zero and the first $1/e$-crossing of the autocorrelation function of the reference time series. Figure 4.6 shows the significance level as a function of the lag for each of the models. For zero lag, the significance level is 0.59, 0.53 and 0.35 for ECCO, OCCAM and POP, respectively. At longer lags, the number of points decreases and therefore the significance level increases exponentially (Figure 4.6). In ECCO, when using this constraint at lags of 5 years, the correlation coefficient should be larger than 0.85 to be significant, while for lags larger than 7 years coefficients are never significant. As a result, we are not able to trace the anomalies back for more than 5 years in practice.

Finally, the results of all grid points are combined to obtain an overview at the basin scale. All layers are analyzed equally. However, the results can be summarized by the layer of the reference time series (Figure 4.7). In the top panel of Figure 4.7, the maximum significant correlation coefficient at each point is shown; the lags corresponding to these maxima are displayed in the bottom panel. Positive lags indicate that the correlated anomaly at the particular grid cell occurred before the anomaly in the mooring section; negative lags indicate that the correlated anomaly occurred after the anomaly in the section. Anomalies propagate from grid cells with large positive lags, via areas with zero lag, towards the cells with large negative lags. Along their paths, the anomalies remain in a positive correlation with the anomaly at the reference section. A pathway of an anomaly should be continuous in time, i.e., jumps in the lag are unphysical. These unphysical paths shall not be considered in the analysis.

As expected, the correlation of the averaged section in the Mozambique Channel with a point at that section is almost one and has a zero lag. Upstream (downstream) the lag increases (decreases). The largest lag in a direct physical path with the mooring section can be seen at 85.5°E, 12.5°S, and is 2 years (bottom panel of Figure 4.7). Its correlation coefficient is 0.74, which is slightly larger than the significance level at this lag. From there, the anomaly moves

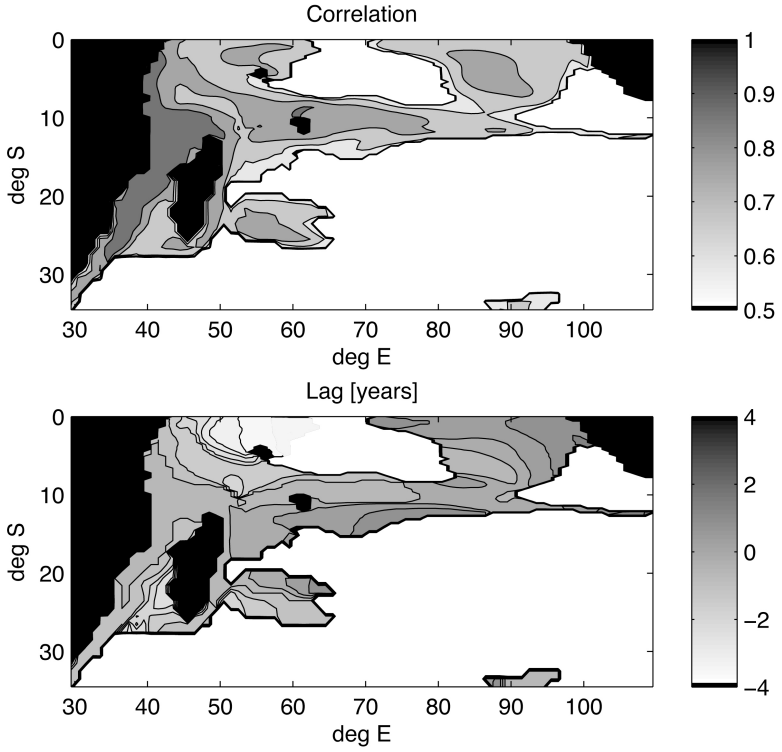

Figure 4.7: *Values of maximum correlation (upper panel) and lags corresponding to these maxima (lower panel, in years) for correlations in ECCO of the salinity time series at each grid point in the domain with the section averaged salinity time series in the Mozambique Channel at the depth of the salinity anomaly (240 m depth). Only significant correlations are displayed (see section 4.4). Positive lags denote that the anomaly at that point appeared before the anomaly in the Mozambique Channel. Contour interval is 0.1 for the top panel and 0.5 years for the bottom panel.*

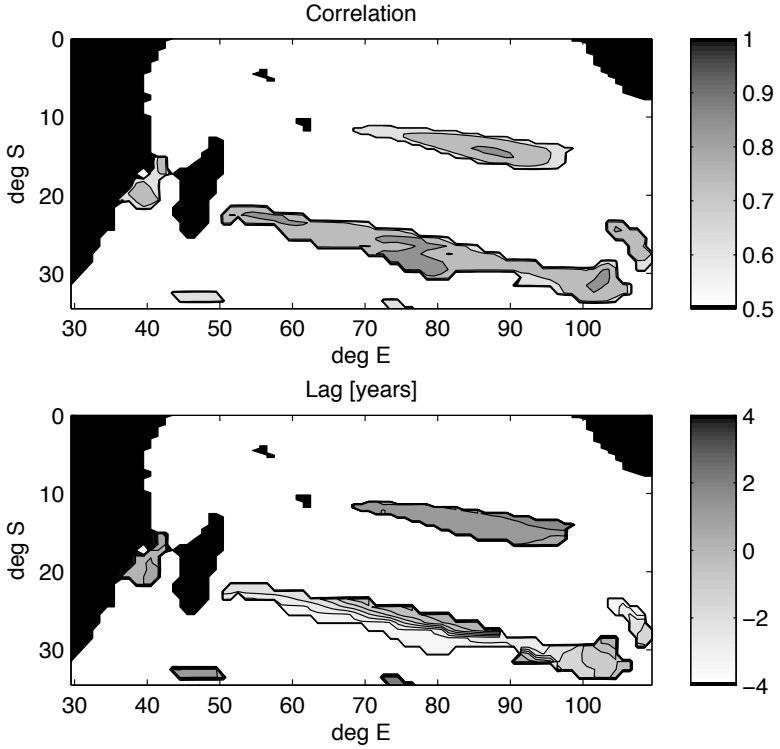

Figure 4.8: *As Figure 4.7 but now for correlations with the zonal velocity time series (positive eastward) at each grid point with the section averaged salinity time series in the Mozambique Channel at the depth of the salinity anomaly (240 m depth).*

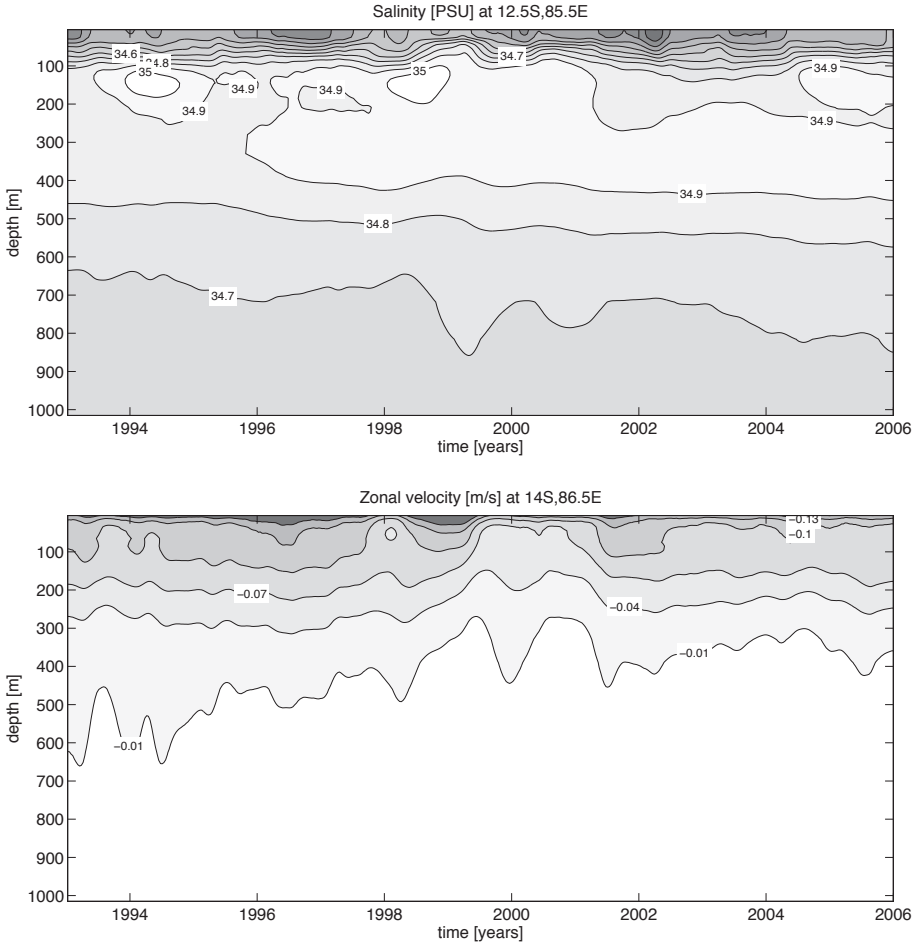

Figure 4.9: *(upper panel) Salinity anomaly at the starting point of the path physically realistically leading to the Mozambique Channel in the ECCO simulation; (lower panel) Anomaly in the zonal velocity at the core of the highly correlated region. The time series have been averaged over an 2° x 2° region around the location defined above the figures.*

westward in the SEC towards Madagascar. The vertical extent of this path is roughly from 150 m – 330 m depth. At the African coast, one part moves southward into the Mozambique Channel and the Agulhas Current. An other part moves north along the African coast. This latter part is also fed by another path extending directly from the eastern boundary of the domain. Note that the anomaly could not travel from 85.5°E northward, since there is a jump in lags at 11°S.

In the northern part of the domain, around 60°E, 5°S, the signal is correlated with a negative lag up to the surface, which is probably due to wind-forced upwelling.

To verify whether the transported signal is the salinity anomaly itself, we studied the salinity time series in a 2° x 2° region around 85.5°E, 12.5°S (top panel of Figure 4.9). Indeed, a salinity anomaly is present at this location 2 years before it is observed in the Mozambique Channel. The anomaly stretches from 75–280 m depth and has its maximum in June 1998. The amplitude of the simulated anomaly is only 0.07 PSU, which makes it improbable that this anomaly is the only cause of the anomaly in the Mozambique Channel.

The change in lag along the path is directly related to the background velocity along the streamlines of the path. Extrapolating the path backward in time, the anomaly originates from the Indonesian waters at the end of 1997. The occurrence of both an El Niño and a positive IOD explains the salinity increase of this water.

The correlation analysis method conducted on the zonal and meridional velocity fields yields a second origin for the salinity anomaly in ECCO. In Figure 4.8, a positive correlation to the zonal velocity with an area stretching around 86.5°E, 14°S is observed. A positive correlation in a westward flowing current (SEC; zonal velocity is defined positively eastward) means a weakening of that current. Note that the correlation is primarily found at the northern limit of the SEC, which means that the speed of especially the TSW and ITFW is weakened. The lag of this region with the Mozambique Channel is 9 months. Figure 4.9 shows that the anomaly is 3cm/s, and that it reaches to the surface. An estimation of the salinity increase caused by this velocity anomaly of fresh waters, taken into account its width and hight, is in the order of 0.1 PSU.

Lee (2004) and *Lee and McPhaden* (2008) have shown that the zonal wind stress south of the Equator (20° −0°S) weakened over the period 1992–2000 and increased afterwards. The transport variation estimated by *Lee* (2004) from the amplitude of this wind stress variation and Sverdrup theory is in agreement with the velocity variation in the SEC that we have found.

A second region of positively correlated zonal velocity in ECCO is apparent in Figure 4.8. However, this region has a negative lag and can therefore not be

the cause of the salinity anomaly in the Mozambique Channel.

Results from the model OCCAM differ from the above findings for the salinity field correlations, but are quite similar for the velocity field correlations. Figure 4.10 shows a connection to the subtropical gyre, but not to the Indonesian Throughflow. The first point of the path is found at 77.5°E, 21°S and has a lag of 2.8 years. The anomaly at this point has an amplitude of 0.1 PSU (top panel of Figure 4.12). It follows the northern border of the band, with a velocity in agreement with the streamlines. The correlated region stretches from 205 m to 609 m depth. Then, the signal travels via the NEMC in a very narrow band along the coast, which is more apparent in the lower layers. As in the results of ECCO, the signal splits at the African coast, partly northward along the coast and partly through the Mozambique Channel into the Agulhas Current.

There is no direct physical explanation to the origin of this particular anomaly. However, when applying the correlation function method without significance constraints, the anomaly could be traced further back in time, to a region around 95°E and 27°S where it appeared in 1993 as an area of high salinity. Although its origin is undeterminable in the model output, the salinity anomaly is comparable to the observations of *Bryden et al.* (2003) and *McDonagh et al.* (2005), who found an increase in salinity in the thermocline east of 80°E along 32°S in 1995 relative to 1987, and a decrease between 1995 and 2002.

As in ECCO, the anomaly in OCCAM has a positive correlation with the zonal velocity of the SEC (Figure 4.11). The amplitude of the anomaly is 5 cm/s (bottom panel of Figure 4.12), slightly higher than in ECCO. However, since the width of the region is smaller in OCCAM, this again results in a salinity anomaly in the Mozambique Channel in the order of 0.1 PSU.

The results of POP are harder to interpret, since the reference time series shows three anomalies, all two years from each other. The highest correlations will therefore be given to time series that correlate with all three anomalies. Also, the significance levels are much lower because of this, and the resulting figures show many regions that are not cause-effect related to the salinity anomaly of 2000 – 2001. For the analysis of POP we will therefore focus even more on the highest correlations with physically realistic paths.

Only the salinity fields above 200 m depth are correlated to the Mozambique Channel anomaly. As in ECCO, the anomaly originates from the SEC (Figure 4.13), but it is not connected to the Indonesian Throughflow, rather to the subtropical part of the SEC, as can be seen from the high background salinity found around the first point of the path (68.8°E, 17.8°S, with a lag of 8 months, top panel of Figure 4.15). In contrast to ECCO and OCCAM, the salinity

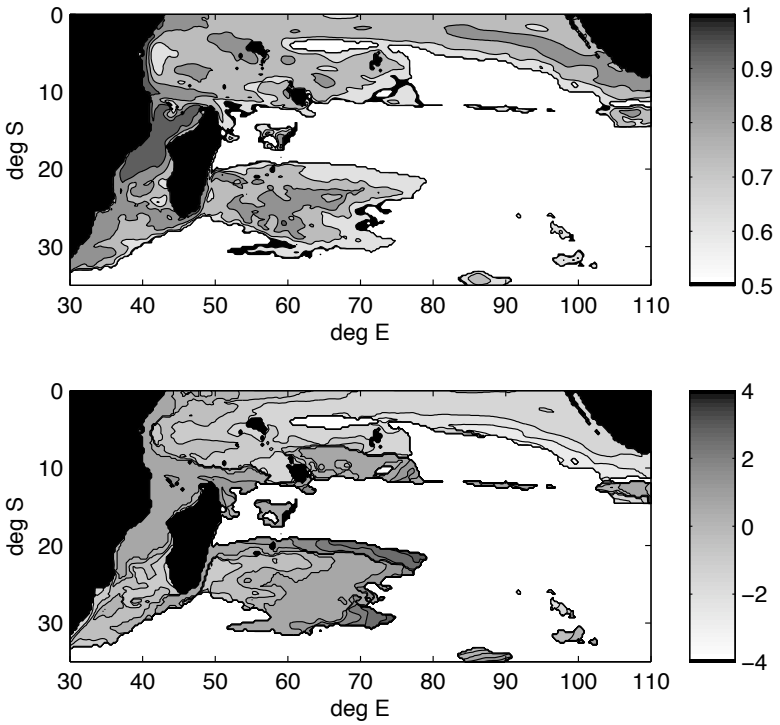

Figure 4.10: *Correlation (upper panel) and lag (lower panel) of the salinity field in OCCAM at 253 m depth (as Figure 4.7).*

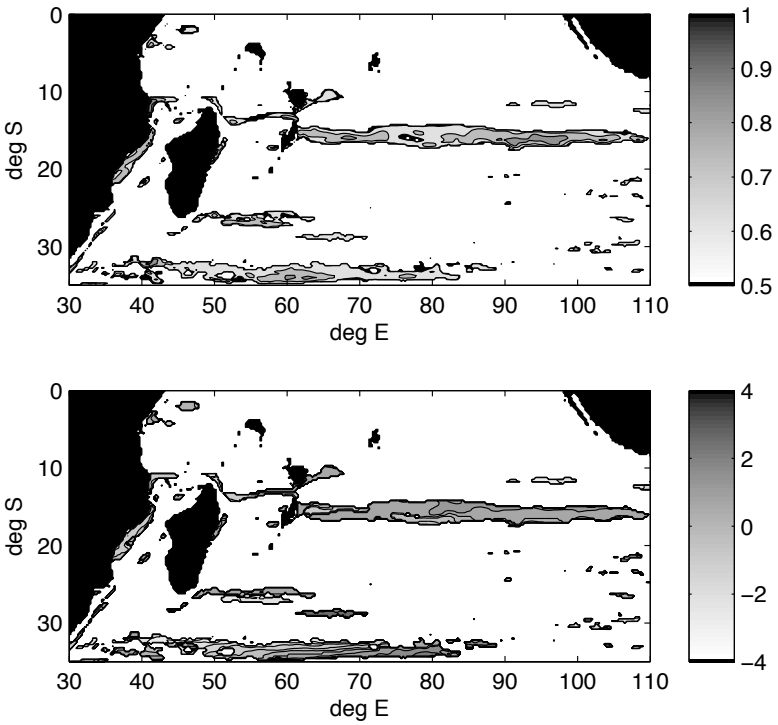

Figure 4.11: *Correlation (upper panel) and lag (lower panel) of the zonal velocity field in OCCAM at 253 m depth (as Figure 4.8).*

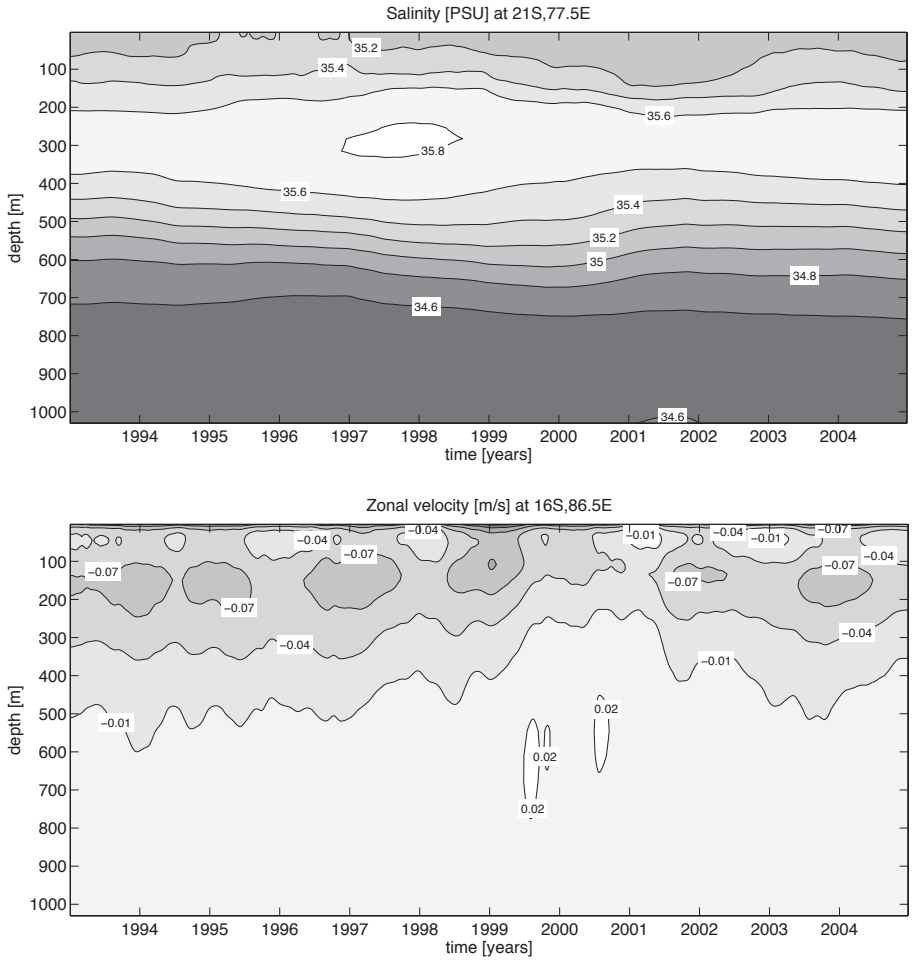

Figure 4.12: *Salinity origin (upper panel) and core of the velocity anomaly (lower panel) in OCCAM (as Figure 4.9).*

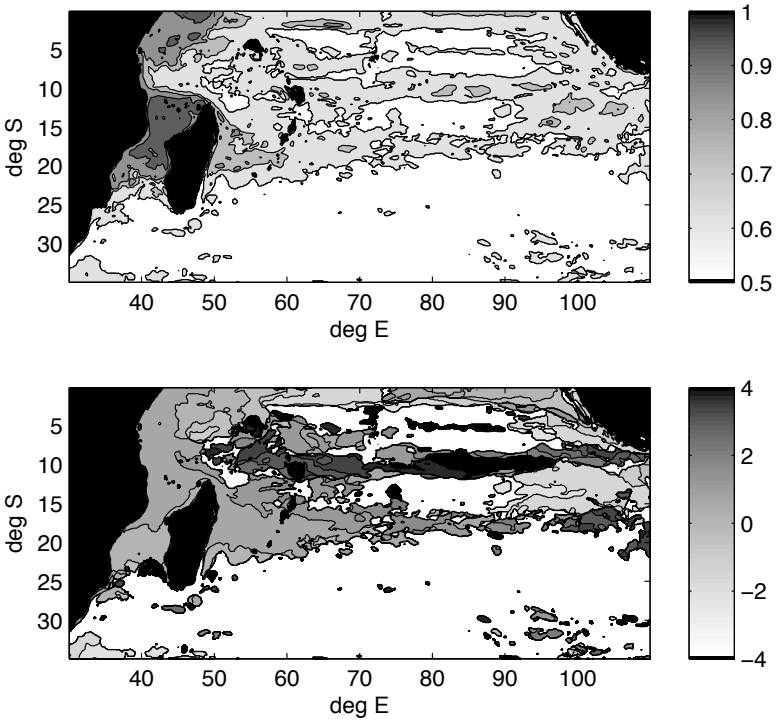

Figure 4.13: *Correlation (upper panel) and lag (lower panel) of the salinity field in POP at 171 m depth (as Figure 4.7).*

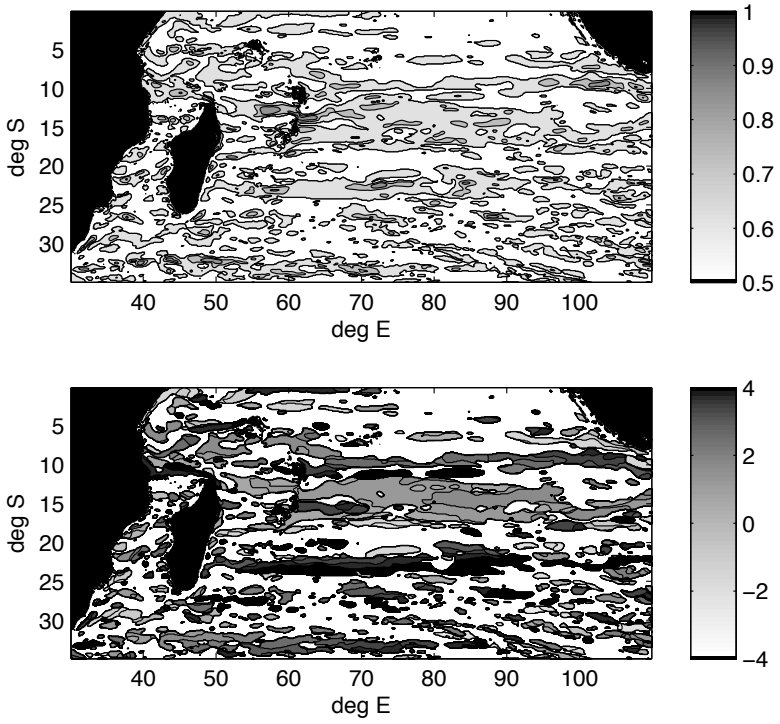

Figure 4.14: *Correlation (upper panel) and lag (lower panel) of the zonal velocity field in POP at 171 m depth (as Figure 4.8).*

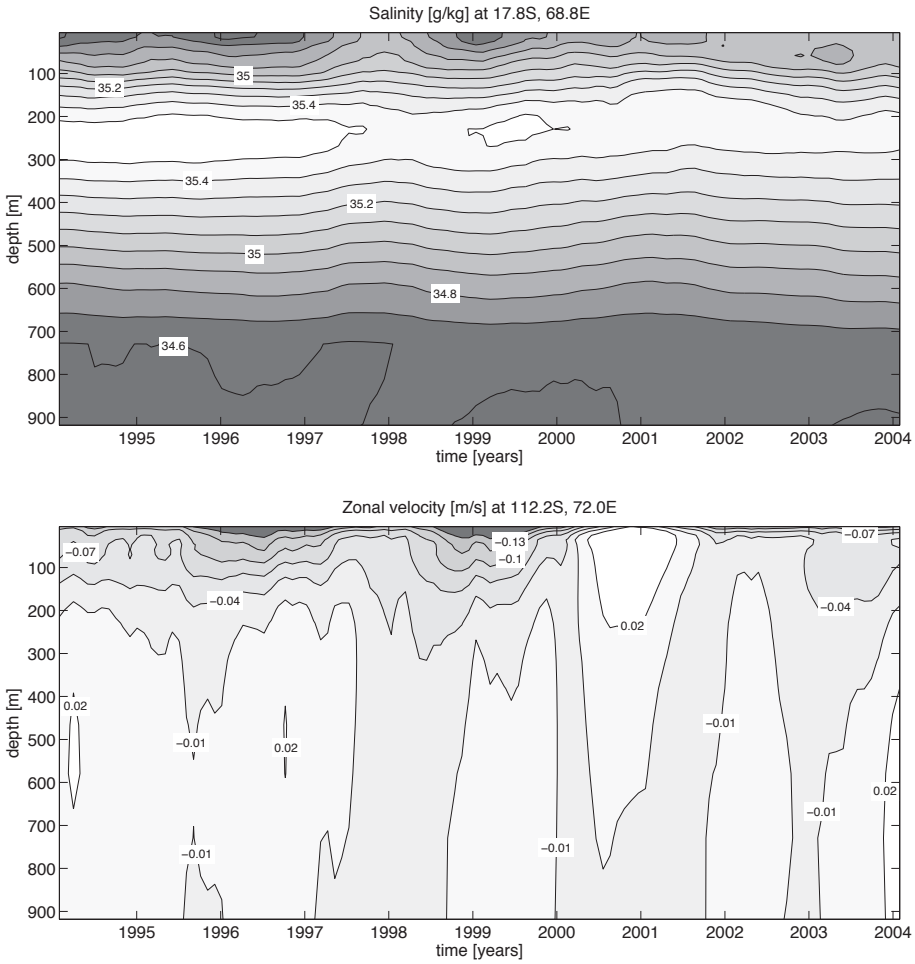

Figure 4.15: *Salinity origin (upper panel) and core of the velocity anomaly (lower panel) in POP (as Figure 4.9).*

anomaly in POP emerged in the model's time and spatial domain. Figure 4.15 shows that it is not the anomaly in the maximum salinity layer that correlates with a lag of 8 months, but the upwelling of isohalines instead. This upwelling is caused by an anomalous negative wind curl of 0.01 N/m^3. Note that the maximum salinity layer is deeper than 200 m, where no correlation path has been found.

In the results for the correlation of the zonal velocity field there is a lot of noise. However, as in the results for ECCO and OCCAM, the SEC is weakening at its northern limit just before the salinity anomaly in the Mozambique Channel (lag is 10 months).

To summarize the above results, we have found a salinity anomaly in all three numerical models that resembles the anomaly as observed in the LOCO project. The three models do not give us a unique cause for the origin of the anomaly in the salinity field. Nonetheless, all three models show a correlation with the strength of the SEC, which is related to a decrease in the wind stress (*Lee*, 2004; *Lee and McPhaden*, 2008), and the advection of a salinity anomaly formed elsewhere in the basin. Given the agreement in the models on the weakening of the SEC, we conclude that this mechanism is likely a major part of the origin of the anomaly found in the observations.

4.5 Conclusions and discussion

The aim of this study was to describe and explain the variations in the salinity field observed in the Mozambique Channel. In 2000 and 2001, a strong positive salinity anomaly has been found both in *in situ* measurements and in three numerical models (ECCO, OCCAM and POP). In all cases, the anomaly was an interannual variation and not a seasonal phenomenon. The most probable origin of this anomaly is the anomalous inflow of subtropical waters, caused by a weakening of the northern part of the SEC by weaker trade winds. In addition, the models indicated a possible salinization of one of the source water masses, i.e., a saltier ITFW from the 1997 El Niño and IOD+ (ECCO), a saltier patch in the southeastern Indian Ocean (already present at the start of the time series in OCCAM), or upwelling of the salinity maximum layer by a local wind curl (POP).

The method we used to obtain these results was based on correlation functions. This method was less effective in the case of POP. The POP salinity time series showed three anomalies, which were regularly spaced in time. The method could not distinct correlations with the 2000 – 2001 anomaly from correlations with the other anomalies. This resulted in many regions which were correlated to the salinity time series of the LOCO section, but not all of which

could be physically related to the 2000 – 2001 anomaly. This is unfortunate, since the POP run had the highest horizontal resolution of the three numerical models.

In a recent paper, *Nauw et al.* (2008) have described a similar salinity variation in the SEMC. In four sections around the south coast of Madagascar, the along-current salinity differences were small, of the order of 0.1 PSU or less. However, compared to data collected during a World Ocean Circulation Experiment (WOCE) survey in 1995, the salinity maximum during the occupation of 2001 was 0.2 PSU higher (their Figure 6c).

In the results from the models ECCO and OCCAM, a positive correlation at zero lag of the salinity anomaly at the section in the Mozambique Channel with the sections south of Madagascar is found (Figures 4.7 and 4.10). In OCCAM the path towards the SEMC is a side branch of the path described in section 4.4, which means that the anomalies in the Mozambique Channel and the SEMC have a common source. There are two paths leading towards the SEMC in ECCO, one starting at the same location as the path towards the Mozambique Channel, i.e., 85.5°E, 12.5°S, and the second starting at a more southern origin. These two origins have a common source by an insignificantly correlated path. As in the Mozambique Channel, the anomalies in the SEMC of the two numerical models have a smaller amplitude than in the *in situ* observations because of smoothing. This additional agreement with observations gives extra support to the results from ECCO and OCCAM, which suggested that the strength of the SEC is a major part of the origin of the anomaly found in the observations.

5

The Effect of Rectification of Variability on the Time Mean Mozambique Channel Transport

The estimates of the time mean transport through the Mozambique Channel by numerical models can vary considerably, especially for eddy-permitting or lower-resolution models. In this chapter, we provide a possible explanation for this: not all models simulate the same modes of variability, and hence the rectified total mean transport in the Mozambique Channel is different. The rectification processes are studied in a simple setup using a hierarchy of models, ranging from an analytical steady state model to models that simulate barotropic and baroclinic variability. The mean transport is found to be very sensitive to the type of internal variability present in the flow. The rectification by the divergence of eddy stresses is the most important term that affects the time-mean circulation. It is largest at the north and south boundaries of the island. The amount of rectification differs between the simulations and is likely responsible for the range in transport estimates.

5.1 Introduction

In the previous chapters, it has been shown that the Mozambique Channel throughflow is highly variable on a range of time scales. This throughflow is important for the global circulation, because it affects the properties of the inter-ocean exchange south of Africa (for an overview, see *De Ruijter et al.*, 2005; *Lutjeharms*, 2006, and Chapter 1). Apart from measurements (e.g. *DiMarco et al.*, 2002; *Harlander et al.*, 2009; *Ridderinkhof et al.*, 2009), the Mozambique Channel throughflow has been simulated in numerical models. Advantages of numerical simulations are that data is available on a larger and denser spatial domain and, if preferred, on a larger temporal domain. Moreover, numerical experiments can be designed to study the basic physical processes by simplification of, for example, the atmospheric forcing and bathymetry.

However, the outcomes of numerical models vary considerably. An example of this is the estimated mean Mozambique Channel volume transport of six ocean general circulation models (Figure 3.5): the time mean values of especially the eddy-permitting and lower-resolution models (ECCO, ORCA025 and OCCAM025) are quite diverse (respectively, 20.9 Sv, 23.6 Sv, and 11.3 Sv). When using these models, it is important to understand possible causes for this diversity in mean transport. Especially, because it is easier to use lower resolution models for long experiments such as climate change simulation experiments, as they are cheaper in computational time.

One possible explanation for the range in time mean transports is that not all models might favour the same modes of internal variability. Rectification of these modes affects the mean state of the ocean (*Feron et al.*, 1998; *Katsman et al.*, 1998; *Alves and Colin de Verdiere*, 1999; *Berloff et al.*, 2007), and some of these modes might therefore change the mean transport through the Mozambique Channel.

To study this process, the Mozambique Channel transport is quantified in a hierarchy of four different models: a linear, frictionless, analytical, steady state model, a steady state shallow water model, a transient primitive equation model with one layer, and a transient primitive equation model with two layers. Differences between the simulations with these models show the influence of friction, nonlinearities, and barotropic and baroclinic variability. The setup of the models is representing the Southern Indian Ocean, but at the same time, it is kept as simple as possible. Therefore, we study a wind-driven double gyre system in a closed basin containing an island under steady wind forcing. The double gyre system consists of a tropical and subtropical gyre. The basic flow is thus different from Gulfstream-like configurations (e.g. *Nauw and Dijkstra*, 2001; *Dijkstra*, 2005; *Berloff et al.*, 2007), because the current

dividing the two gyres flows westward instead of eastward. The setup is chosen such that this current impinges the island and bifurcates, as representation of the South Equatorial Current, the Northeast Madagascar Current and the Southeast Madagascar Current (Figure 1.3).

In the circulation, variability can be identified at a range of scales. On the one hand, there is the variability created at the northern and southern tip of the island, due to instabilities of the flow (*Quadfasel and Swallow*, 1986; *Pedlosky et al.*, 1997; *Biastoch and Krauss*, 1999; *Schouten et al.*, 2003; *De Ruijter et al.*, 2004; *LaCasce and Isachsen*, 2007). On the other hand, variability exists at larger scales, such as basin and gyre modes (*Pedlosky*, 1987; *Dijkstra*, 2005). One of the main questions we address here is at what scale the rectification of variability gives the largest contribution to the Mozambique Channel transport.

First, the setup of the experiments and the four models will be introduced. Next, the transports through the 'Mozambique Channel' of the four models will be studied and their differences discussed in section 5.3. Two simulations will be discussed in more detail in section 5.3.2. By analyzing the time-mean vorticity balance of their flow, the importance of the variability will be illustrated. After a summary of the results, it will be discussed whether rectification might play a role in the time mean Mozambique Channel transport in ocean general circulation models.

5.2 Setup and models

5.2.1 General setup of the models

The model setup (Figure 5.1) is similar for all four models and is based on the Southern Indian Ocean. The basin is closed and stretches from 40°E to 90°E and from 5°S to 35°S. At the western side of the basin, a rectangular island is representing Madagascar (44°E – 48°E; 15°S – 25°S). In the following, the part of the basin west of the island is referred to as the 'channel'. The grid of the models is defined in spherical coordinates. The basin has a flat bottom and is 1000 m deep for all models except for the two layer transient model, in which the equilibrium thicknesses of the layers are $H_1 = 1000$ m and $H_2 = 2000$ m. The models use a Laplacian horizontal friction with $K_h = 500\,m^2/s$ and a kinematic viscosity with $K_v = 1 \cdot 10^{-4}\,m^2/s$. A no-slip boundary condition is applied, and bottom friction is neglected. In this setup, the channel is wide enough (it is almost 15 times the Munk boundary layer) not to obstruct the flow (*Pratt and Pedlosky*, 1998). The water in the basin has a constant density ($\rho_0 = 1030\,kg/m^3$). In the 2-layer transient model, the densities of the layers are $\rho_1 = 1030\,kg/m^3$ and $\rho_2 = 1035\,kg/m^3$, respectively.

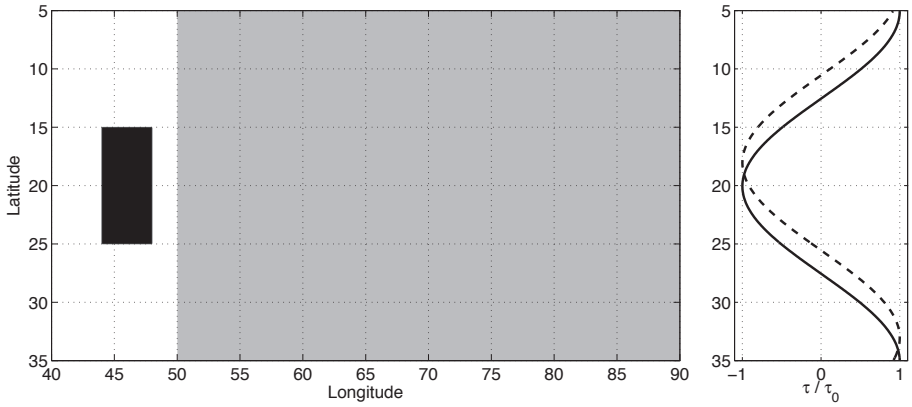

Figure 5.1: *Model setup. The basin measures 50° in longitude and 30° in latitude. An island is placed close to the western boundary of the basin and stretches from $44° - 48°E$ and $15° - 25°S$ (black rectangle). East of $50°E$, wind forcing is applied (gray area). Two different wind profiles have been used (right figure): a symmetrical cosine profile (solid line) and an asymmetrical profile (dashed line), which is similar to the symmetrical profile but shifted 2° to the north. The wind profiles are plotted as a function of their amplitude.*

The models are forced by a steady, zonal wind stress (Figure 5.1). The wind is only applied east of 50°E, and does therefore not interfere directly with the circulation around the island. Two different profiles of the wind stress have been used, both producing a double gyre structure. The observed annual mean zonal wind stress east of Madagascar (e.g. Figure 4 in *Schott and McCreary*, 2001) is almost symmetrical with respect to the island. This symmetry is taken as a base for the first wind profile ('symmetric'), which is a one-period cosine function of the latitude with a maximum westward wind stress at 20°S and a maximum eastward wind stress at the north and south boundary of the basin. The second wind profile is based on the austral winter, when the intertropical convergence zone has a more northward position. This 'asymmetric' wind profile is equal to the 'symmetric' profile, but it is shifted to the north by 2°. The amplitude of both cosine functions τ_0 is varied between 0.01 N/m^2 and 0.4 N/m^2.

5.2.2 Models

The analytical model The linear island rule (LIR, *Godfrey*, 1989) is an analytical model for the transport west of an island. It is based on the Sverdrup balance and neglects nonlinearity and friction. Moreover, it assumes that the ocean has a level of no motion that is situated above the main topographic features. In the case of a basin with a flat bottom, the level of no motion is

the bottom itself. The strength of the LIR is that the western boundary layers, i.e. the most nonlinear parts of the flow, are being avoided in the calculation of the transport. For a configuration with zero meridional windstress, the LIR estimates the transport T in the channel as:

$$T = -\frac{1}{\rho_0(f_N - f_S)} \left(\int_{dS} \tau \, dx - \int_{dN} \tau \, dx \right), \tag{5.1}$$

where f_N and f_S are the Coriolis parameters at the north and south boundary of the island, respectively. $\int_{dS(dN)} \tau \, dx$ is the integrated zonal wind stress τ over a line of equal latitude from the southern (northern) tip of the island to the eastern boundary of the basin.

In the case of the symmetrical wind profile, $\tau(S) = \tau(N)$ and the two integrals almost have the same value but for the distance between the island and the east coast of the basin due to the spherical geometry. The total transport in the channel will therefore be very small.

The steady state model For the steady state simulations, the same barotropic shallow water model is used as in *Dijkstra and De Ruijter* (2001a) and *Palastanga et al.* (2009). The model consists of the shallow water equations in spherical coordinates. A continuation technique based on the pseudoarclength method (*Keller*, 1977) is used to determine the steady state solutions. In this method, a control parameter is continuously varied, which in this study is the wind stress amplidue τ_0. The model uses an Arakawa C-grid with a horizontal grid spacing of 0.2°.

The two transient models The simulations with the two transient models are conducted with the Hallberg Isopycnal Model (HIM, *Hallberg*, 1997). This model uses a time-splitting scheme to solve the hydrostatic primitive equations. We have used a barotropic time step of 30 s and a baroclinic time step of 240 s. Like the steady state model, it uses an Arakawa-C grid in spherical coordinates. Its horizontal grid spacing is 0.1°. The properties of the 1-layer configuration are the same as those of the steady state and analytical models. In the 2-layer configuration, an extra, lower layer is added with a density of $\rho_2 = 1035\, kg/m^3$ and an equilibrium thickness of 2000 m. This makes the total equilibrium depth of the basin in the 2-layer configuration 3000 m. Diapycnal diffusion is not included.

The transient simulations are spun up from rest and are run for 10 years with a 50-day mean output frequency. Typically, the transport in the channel reaches a statistical steady state after approximately three years. This is consistent with the period in which the first baroclinic Rossby wave crosses the

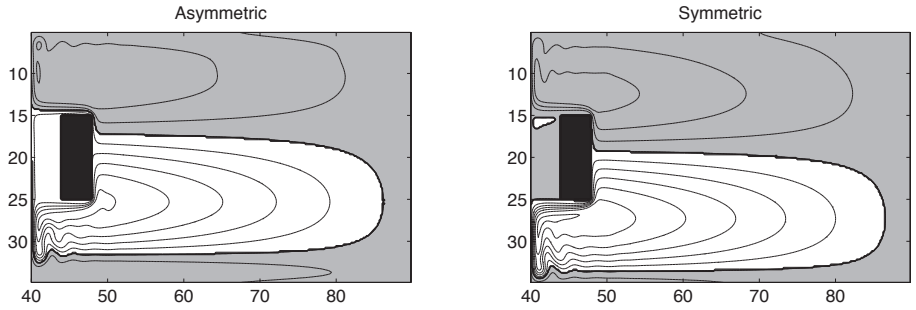

Figure 5.2: *Sea surface height for cases with an asymmetric (left) and symmetric (right) wind profile with the steady state model ($\tau_0 = 0.05\,N/m^2$). Contour interval is 2 cm; gray area has negative values.*

basin at its southern limit (about 620 days). These first three years should therefore be excluded from the analysis. In addition, a relatively long time interval should be chosen to calculate the mean transport, typically more than two years, as the transport fluctuates considerably. Because these values are somewhat different in each simulation, and we wanted to analyze each simulation equally, we have chosen to use the last five years of each simulation for analysis. For section 5.3.2, the simulations of the cases with a symmetric wind stress profile and a wind stress amplitude of $\tau_0 = 0.2\,N/m^2$ were repeated to obtain information on variability at longer and shorter time scales. The first set of simulations covered a period of 100 years with a 50-day mean output frequency. The second set contained restarts of these simulations of 180 days with a daily-mean output frequency.

5.3 Results

As an example of the flow pattern, the sea surface heights of a steady state simulation forced with an asymmetrical wind profile and a symmetrical wind profile ($\tau_0 = 0.05\,N/m^2$) are shown in Figure 5.2. In both plots, a clear double gyre pattern is visible. The sea surface height depends not only on the wind curl, but also on the latitude ϕ, because of a linear dependency on the Coriolis parameter ($\sim \sin\phi$), and the width of the area in which wind forcing takes place ($\sim \cos\phi$). At the latitudes considered in this basin, the scaling with $\sin\phi$ exceeds that of $\cos\phi$, which causes the amplitude of the sea surface height in the southern, anticyclonic gyre to be higher as that in the northern, cyclonic gyre.

The main current dividing the two gyres represents the South Equatorial Current. It impinges the island at 19°S in the symmetric case and at 17°S

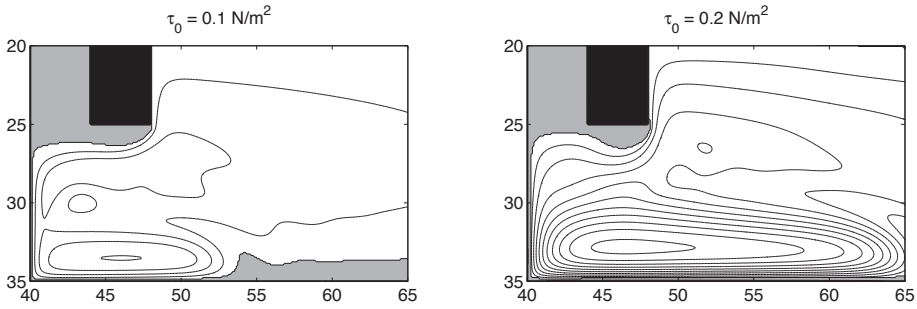

Figure 5.3: *Blow-up of the southern recirculation cell, which is formed at larger values of the wind stress amplitude. Shown is the time-mean sea surface height over the last 5 years of the simulation for the 1-layer simulations with the transient model. The models are forced by a symmetric wind profile with* $\tau_0 = 0.1\,N/m^2$ *(left) and* $\tau_0 = 0.2\,N/m^2$ *(right). Contour interval is 10 cm; gray area has negative values.*

in the asymmetric case. It then splits into two western boundary currents, rounding the north- and southeast corners of the island. The southern gyre of the asymmetric case encloses the island, causing a southward channel transport. In the symmetric case, on the other hand, the channel is not part of one of the gyres and only a very small transport in the channel exists.

For larger values of the wind forcing amplitude, the nonlinearities at the northwest and southwest corner of the basin, that are already visible in Figure 5.2, strengthen. Two recirculation cells develop that have signs equal to the two large gyres (Figure 5.3). For $\tau_0 \geq 0.2\,N/m^2$ (the right panel of the figure), the circulation in the two gyres focusses gradually more to the north and south boundary of the basin, until the gyre and the recirculation cell form one continuous gyre. These recirculation cells do not interact with the island.

5.3.1 Transports in the four models

For each of the four models and for both wind stress patterns, the transport in the channel is determined at 20°S as a function of the wind-stress amplitude (Figure 5.4). In addition, the error E in the estimate of the transport is calculated for the two transient models:

$$E = \sigma_T / \sqrt{N}, \tag{5.2}$$

where σ_T is the standard deviation of the transport time series and N the number of independent elements in the time series. N was found to have an equal value for all the simulations, $N = 37$, which was determined from the 1/e-crossings in the autocorrelation functions of each of the transport time

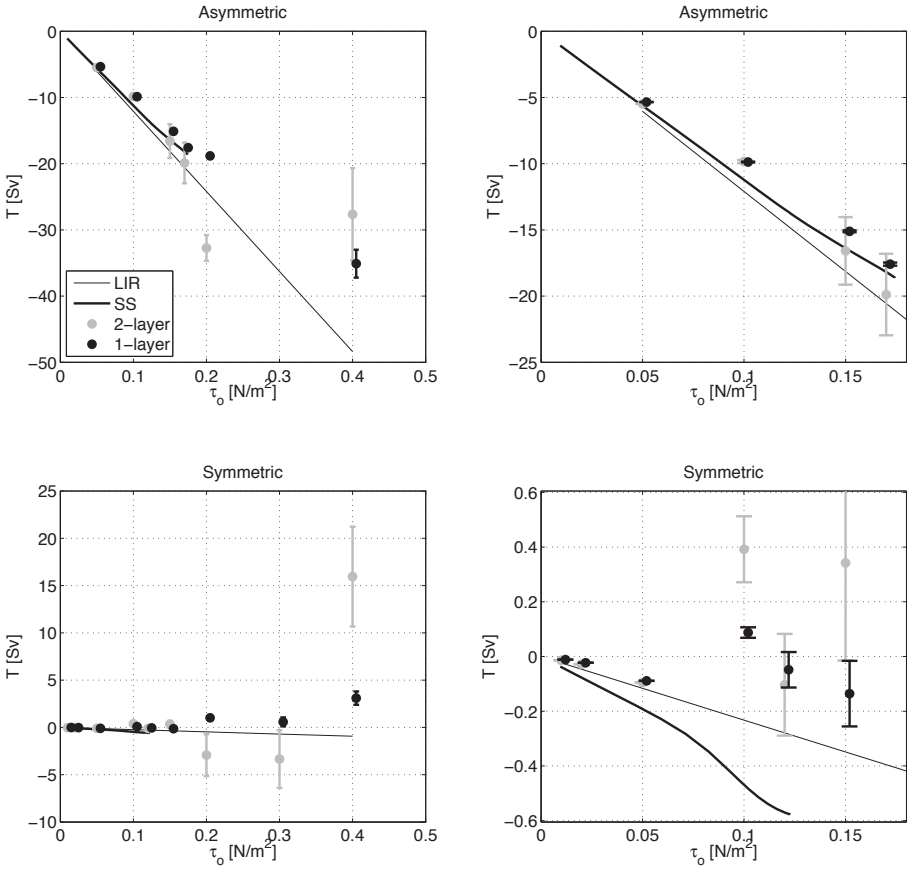

Figure 5.4: *Transport estimates of the different models as a function of the wind stress amplitude. The two upper (lower) figures show the asymmetric (symmetric) case. The two panels at the right hand side are zoomed in to the lower values of τ_0. Estimates from four different models: the Linear Island Rule estimation (LIR, thin line), steady state integration (SS, thick line), transient simulations for the two-layer model (2-layer, gray dots) and for the one-layer model (1-layer, black dots). The error estimates in the transient simulations are based on the standard deviation of the transport (see the text for details), and are roughly one sixth of the standard deviation. Positive values denote northward flow. Especially for higher values of τ_0, the estimates between the different models vary considerably.*

series. This implies that the standard deviation of the transport is roughly six times the length of the error bar shown in the figure.

The transport estimate of the LIR is linearly dependent on the wind forcing amplitude, as all other parameters of the model are fixed by the setup. The resulting estimates in Sverdrups are $T = -121\,\tau_0$ for the asymmetric case and $T = -2.3\,\tau_0$ for the symmetric case, where τ_0 should be given in N/m^2. (Positive values denote northward flow.) As the maximum wind amplitude in our simulations is $0.4\,N/m^2$, this results in a maximum transport of -48.4 Sv and -0.9 Sv, respectively. For both wind patterns, the expected transport is thus southward. When relating these values to the real ocean, a typical wind stress amplitude of $\tau_0 = 0.2\,N/m^2$ should be used (the typical wind stress in the Indian Ocean is $\tau \sim 0.1\,N/m^2$ but the basin width used in this study is about half of the real width of the Indian Ocean). The mean transport according to this model would therefore be 24.2 Sv and 0.5 Sv southward for the asymmetric and symmetric wind forcing, respectively. In reality however, the basin is not closed, and contributions from, e.g., the Indonesian Throughflow (15 Sv, *Sprintall et al.*, 2009) and freshwater input should be added. Thus, the transport in the model forced with a symmetric wind pattern is close to the observed mean transport (16.7 Sv, *Ridderinkhof et al.*, 2009, and Chapter 2).

A linear dependence is also found in the steady state simulations for small amplitudes of the wind stress, as the flow is still stable in this regime. The slope of the dependence is -111 Sv m^2/N and -3.9 Sv m^2/N, for the asymmetric and symmetric case, respectively. The deviation of the LIR to the steady state simulations is thus 9% for the asymmetric cases. This is in agreement with previous studies (*Pedlosky et al.*, 1997; *Pratt and Pedlosky*, 1998; *Firing et al.*, 1999; *Wells and Helfrich*, 2001; *Palastanga et al.*, 2009) who found a maximum deviation of the LIR of 20%, and who accounted most of this deviation to friction. In the symmetric cases on the other hand, the LIR has a deviation of 41% to the steady state simulations, although in absolute values the difference is still very small.

For larger wind stress amplitudes, the deviation between the LIR and steady state simulations widens, as then non-linearities and acompanying friction come into play. The maximum wind stress amplitudes for which steady states could be computed were $0.12\,N/m^2$ and $0.17\,N/m^2$ for the symmetric and asymmetric wind pattern, respectively. Above this value, the continuation technique did not give results, as the outcomes of the iterations did not converge.

The time mean transport estimates of the two transient models differ from the estimates of both the LIR and the steady state simulations, but no consistent relation with the wind strength can be identified. In the asymmetric case for example, the time mean transport in both transient simulations equals the

steady state case for $\tau_0 = 0.05\,N/m^2$. For higher wind strength amplitudes, the 1-layer transient simulations estimate less southward transport than the steady state simulations and the LIR. The 2-layer transient simulations sometimes estimate an equal mean southward transport as the steady state simulations when taking the error into account ($\tau_0 = 0.15\,N/m^2$; $\tau_0 = 0.17\,N/m^2$), sometimes less ($\tau_0 = 0.1\,N/m^2$; $\tau_0 = 0.4\,N/m^2$), and only in one case more ($\tau_0 = 0.2\,N/m^2$).

Similar irregularities can be found in the symmetric case. Because the absolute transport values are so small in these simulations, small absolute deviations can even change the direction of the flow. For example, the direction of the time mean transport in the 1-layer transient case switches from southward to northward to southward flow for $\tau_0 = 0.05\,N/m^2$, $\tau_0 = 0.1\,N/m^2$ and $\tau_0 = 0.15\,N/m^2$, respectively. For $\tau_0 = 0.12\,N/m^2$, the time mean value of the transport is so small that it can both be northward and southward, within the error range. And for $\tau_0 = 0.2\,N/m^2$, the 1-layer case estimates a time mean *northward* transport of 1.0 ± 0.2 Sv while the 2-layer case estimates a time mean *southward* transport of 2.9 ± 2.2 Sv.

From Figure 5.4 also the standard deviations of the transient simulations can be deduced, as a measure of variability. In general, the variability is small for $\tau_0 \leq 0.05\,N/m^2$ and increases for larger τ_0. This is around the same τ_0 as where the nonlinear effects in the steady state simulations come into play. Moreover, the standard deviation of the 2-layer transient simulations is much larger than that of the 1-layer simulations.

In the 2-layer cases, the velocity variability in the lower layer is about the same size as that in the upper layer. This is caused by our choice of the density difference between the two layers, which is relatively small, but realistic: the densities of the two layers are equal to the density in the Mozambique Channel at 20°S at 600 m and 1600 m, respectively. However, the lower layer is about twice the thickness of the upper layer. Therefore, we find that the transport variability of the lower layer is about twice as large as that of the upper layer. The time-mean transport on the other hand, was found to be concentrated in the upper layer.

To assess why the transports of the steady state cases and the transient cases are so different, the mean sea surface heights of the simulations were compared. For each case of the transient simulations, the difference in sea surface height Δ_{SSH} was defined as:

$$\Delta_{\mathrm{SSH}}(\theta,\phi) = \overline{\mathrm{SSH}_{tr}(\theta,\phi,t)} - \mathrm{SSH}_{ss}(\theta,\phi), \tag{5.3}$$

where SSH_{tr} and SSH_{ss} denote the sea surface heights of the transient case and

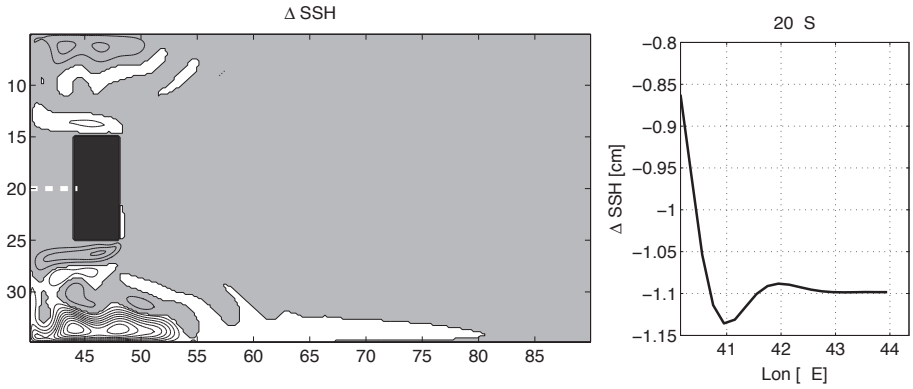

Figure 5.5: *Difference in sea surface height between the 1-layer transient case and steady state case Δ_{SSH} (eq. (5.3)). Used are cases with the symmetrical wind profile and $\tau_0 = 0.1\,N/m^2$. Left: contours over the whole basin; contour interval is 5 cm; gray area has negative values. Right: section through the channel at 20° S (white dashed line in left panel). Similar results for cases with other wind forcings and for 2-layer transient cases.*

the steady state case, respectively, as a function of longitude θ, latitude ϕ and, for the transient SSH, time t. The overbar indicates the time mean. In Figure 5.5, Δ_{SSH} for a 1-layer case with symmetrical wind forcing ($\tau_0 = 0.1\,N/m^2$) is shown. Similar results were found for situations with other wind forcing strengths and profiles, and for the sea surface height difference between the 2-layer transient cases and the steady state cases.

Largest values of Δ_{SSH} are found at the northwest and southwest corners of the basin and at the north and south boundary of the island. In the transient case, the currents south- and northeast of the island have a larger overshoot at the corners of the island than in the steady state case, and therefore are further from the south and north boundary of the island. The sea surface height of the steady state case at for example the southern boundary of the island, is thus more positive than the transient case at these boundaries, and the difference in sea surface height Δ_{SSH} is negative. Also, the recirculation cells in the transient case are stronger, which leads to a positive (negative) Δ_{SSH} in the southwest (northwest) corner. The gradient of Δ_{SSH} between the southwest and northwest corners of the basin causes a zonal gradient of Δ_{SSH} in the western boundary of the channel (right panel of Figure 5.5). From the slope of Δ_{SSH} in the channel and using the geostrophic balance, it can be deduced that the time mean transport in the transient simulation is 0.5 Sv more northward than in the steady state simulation. This is exactly the difference in transport found between the 1-layer transient case and the steady state case for $\tau_0 = 0.1\,N/m^2$ (Figure 5.4).

The main difference between steady state simulation and transient simulation lies thus in the shape of the two gyres, which leads to a different pressure gradient over the channel. In most cases, such as in the above example, the main influence on the channel is caused by differences close to the north and south boundaries of the basin, which leads to an excessive northward transport through the channel. However, not all differences between the transient simulations and the steady state simulations can be explained fully with this result.

5.3.2 The role of rectification

To study the effects of time variability on the mean transport more closely, we will study two cases in more detail. These are the 1-layer and 2-layer transient simulations with a symmetrical wind forcing and $\tau_0 = 0.2\,N/m^2$. These cases were chosen, as the direction of their time-mean channel transport is opposite: northward in the 1-layer case and southward in the 2-layer case (Figure 5.4).

To assess the role of low- and high-frequency variability, the output of simulations with other simulation times and output frequencies were used (section 5.2.2). We have found that the strongest contribution of rectification came from variability with time scales of less than 50 days. Therefore, most results shown in this section have been computed with the data set containing daily-mean output which has a simulation time of 180 days.

The time mean sea surface height of the 2-layer case is different from that of the 1-layer case (Figure 5.6). In the 2-layer case, the southern gyre encloses the island, resulting in a zonal sea surface height gradient in the channel and thus southward geostrophic flow. This is different from the 1-layer case and most other symmetric cases where there is hardly any circulation in the channel (see also Figure 5.2).

The transport time series in the channel of the 2-layer case has a much higher variability than that in the 1-layer case. The standard deviations in the 180-day run are 134.0 Sv and 10.0 Sv, respectively. The variability in both cases is mainly concentrated at a frequency of 17.8/y (a period of 20 ± 1 days, Figure 5.7).

A multi-channel singular-spectrum analysis (MSSA) (*Ghil et al.*, 2000) of the sea surface height time series was performed on a $1^\circ \times 1^\circ$ resolution to identify the dominant modes of variability. The reduction in horizontal resolution was necessary for computational reasons. For each case, the MSSA analysis was carried out both on the sea surface height of the whole basin, and on the sea surface height in a region close to and in the channel ($40^\circ - 46^\circ$E; $13^\circ - 27^\circ$S). The data was preconditioned using a principal component analysis with 10

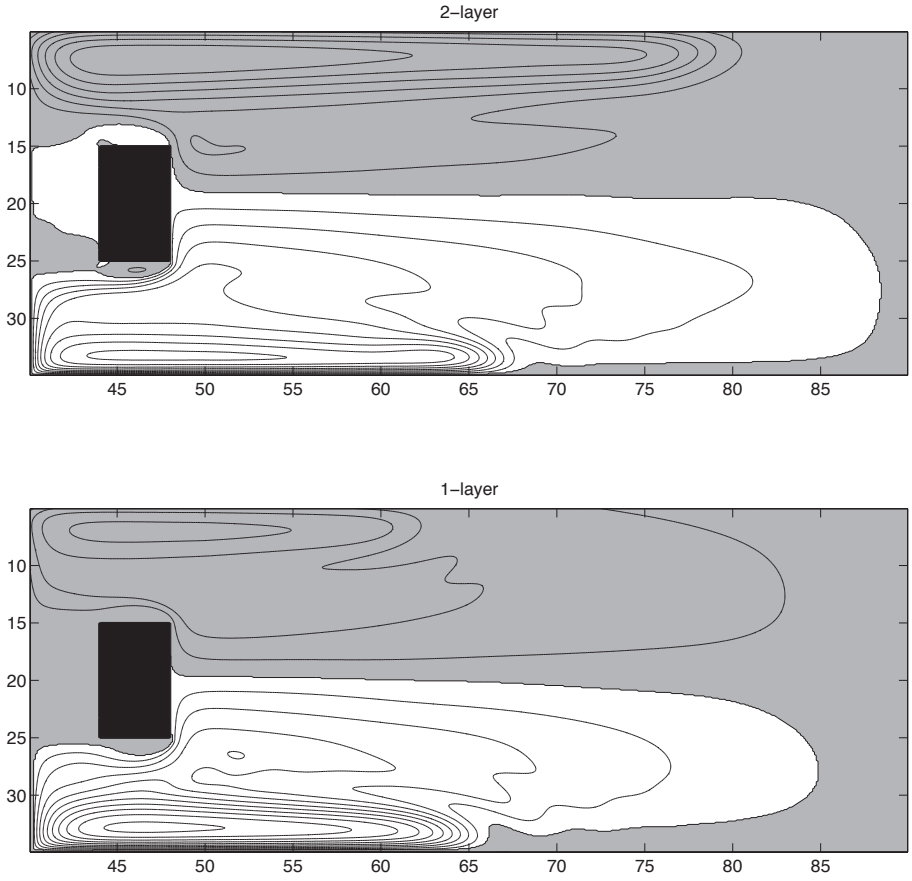

Figure 5.6: *Time mean sea surface height of two transient simulations of 100 years with symmetric wind forcing and $\tau_0 = 0.2\,N/m^2$, for the configuration with 2 layers (upper panel) and 1 layer (lower panel). Contour interval is 10 cm; the gray areas have negative values. The 2-layer case differs from the 1-layer case in that the circulation in the channel is part of the southern gyre.*

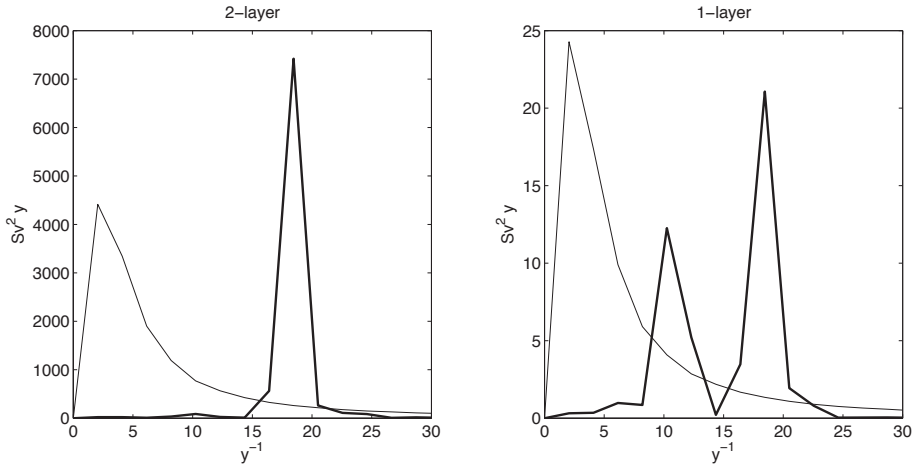

Figure 5.7: *Power spectra of the transport in the channel at 20°S in the two transient cases with symmetric wind forcing and $\tau_0 = 0.2\,N/m^2$, for the configuration with 2 layers (left panel) and 1 layer (right panel). The two simulations were run for 180 days with a daily-mean output frequency. The thin line is the 95% confidence level of an AR(1) spectrum. Note the difference between the vertical axes of the two panels.*

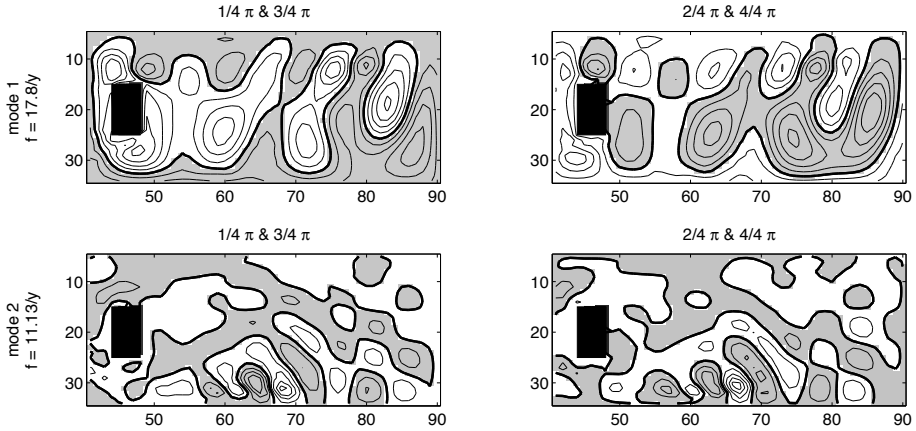

Figure 5.8: *The first two MSSA modes of the sea surface height field in the 2-layer transient case with $\tau_0 = 0.2\,N/m^2$ symmetrical wind forcing. The MSSA analysis was performed on data at a $1° \times 1°$ grid. Contours are drawn each 20% of the maximum absolute value of the mode. The third and forth quarters of the phase of the mode are equal but opposite in sign to the first two quarters. The thick contour denotes zero. The frequency of the modes is written at the left side of the figure. The first mode explains 83% of the variance and the second mode 8%.*

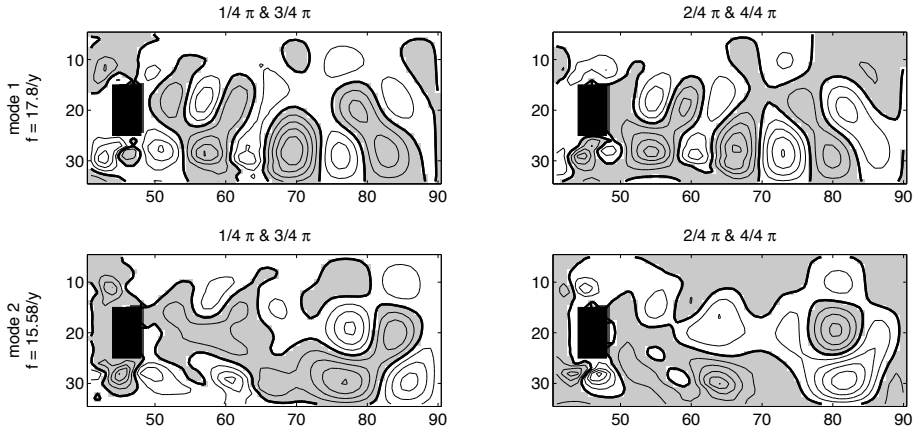

Figure 5.9: *As Figure 5.8 but for the 1-layer transient case with* $\tau_0 = 0.2\,N/m^2$. *The variance explained by the first and second MSSA mode is 51% and 24%, respectively.*

channels. We used a window length of 16 days, and therefore obtain modes with a time series of 165 days. The significance of the modes was checked using a Monte Carlo analysis with a 95% confidence level. The dominant modes of the basin wide variability are shown in Figures 5.8 and 5.9. The first dominant MSSA mode in both cases is a barotropic Rossby basin mode, with a frequency of 17.8/y. In the 2-layer case the barotropicity was confirmed with the passive behaviour of the interphase between the two layers in this mode. The Rossby basin modes explain 83% and 51% of the variance of the 2-layer case and the 1-layer case, respectively. The same patterns were also found in the 100-year long simulations, although here the 50-day output rate of the simulation was too coarse to find the correct frequency. The frequency of this mode is equal to the high frequency variability of the transport in the channel (Figure 5.7). The second mode explains 8% and 24% of the variance respectively. In the 2-layer case (Figures 5.8), the pattern of this mode resembles the pattern of a gyre mode, but its time scale (33 days) is much shorter than the circulation time scale of the gyre, which is roughly 1.5 years.

The barotropic Rossby basin modes clearly have a different character in the two cases. The basin mode in the 2-layer case is strong in the channel (Figure 5.8). This is uphold by the MSSA analysis that was carried out on the sea surface height field in and nearby the channel, as the first mode obtained by this procedure was the same Rossby basin mode. On the other hand, in the 1-layer case, the barotropic Rossby basin mode is strong only outside the channel (Figure 5.9). The power at this frequency in the transport time series (Figure 5.7) is also much stronger in the 2-layer case than in the 1-layer case.

The mode thus probably influences the transport variability in the channel.

The main question is whether the difference in variability also leads to a different mean transport. For this, we start with the potential vorticity equation:

$$\frac{d}{dt}\left(\frac{\zeta + f}{h}\right) = \frac{K_h \nabla^2 \zeta}{h} + \frac{1}{\rho h^2}\frac{\partial \tau}{\partial y}, \tag{5.4}$$

in which ζ and f are the relative and planetary vorticity, respectively, and h is the water depth. K_h is the horizontal friction coefficient. When averaging equation (5.4) in time, the following expression can be found (see also for example *Feron et al.*, 1998):

$$\bar{u}\frac{\partial \bar{\zeta}}{\partial x} + \bar{v}\frac{\partial \bar{\zeta}}{\partial y} + \bar{v}\beta = -\frac{\partial \overline{u'\zeta'}}{\partial x} - \frac{\partial \overline{v'\zeta'}}{\partial y} + \frac{1}{\bar{h}}\overline{\zeta'\frac{\partial h'}{\partial t}} + K_h\overline{\nabla^2\zeta} + \frac{1}{\rho h}\frac{\partial \tau}{\partial y}. \tag{5.5}$$

Here, u and v are the zonal and meridional velocities, and β is the meridional derivative of the planetary vorticity. Overbars denote the time-means and primes denote the anomaly to this mean. This equation shows that the mean state of the circulation (the left side of the equation) is dependent on the variability of the circulation (first three terms at the right hand side). These terms are the divergence of the eddy stresses $\frac{\partial \overline{u'\zeta'}}{\partial x} + \frac{\partial \overline{v'\zeta'}}{\partial y}$ and the stretching term $\frac{1}{\bar{h}}\overline{\zeta'\frac{\partial h'}{\partial t}}$. The friction term depends both on the mean state as on the variabilities.

When estimating the size of each of the terms in equation (5.5) over the full time series, we find that all terms have about the same size, except for the stretching term. This term is a factor 10^6 smaller than the other terms in the 1-layer case and a factor 10^3 smaller in the 2-layer case. In addition, west of 50°E, the wind stress curl is zero. The rectification by the divergence of the eddy stresses is thus the most important variability term close to the island that forces the mean circulation. In Figure 5.10, the absolute size of the divergence term is plotted for the two cases. The divergence of the eddy stresses is largest at the corners of the island, where variability is created in the form of eddies (see Figure 5.11 and for example *Pedlosky et al.*, 1997; *LaCasce and Isachsen*, 2007). The divergence is then advected westward by the mean circulation, and spreads along the north and south boundary of the basin.

In Figure 5.10, it is seen that the divergence of the eddy stresses is much larger in the 2-layer case than in the 1-layer case, especially at the north and south boundary of the basin. Also north and south of the island, this term is much larger (a factor 10) in the 2-layer case. Moreover, we can classify areas in which the rectification by the divergence of the eddy stresses is relevant for the mean circulation. This is roughly in areas where this term is larger than

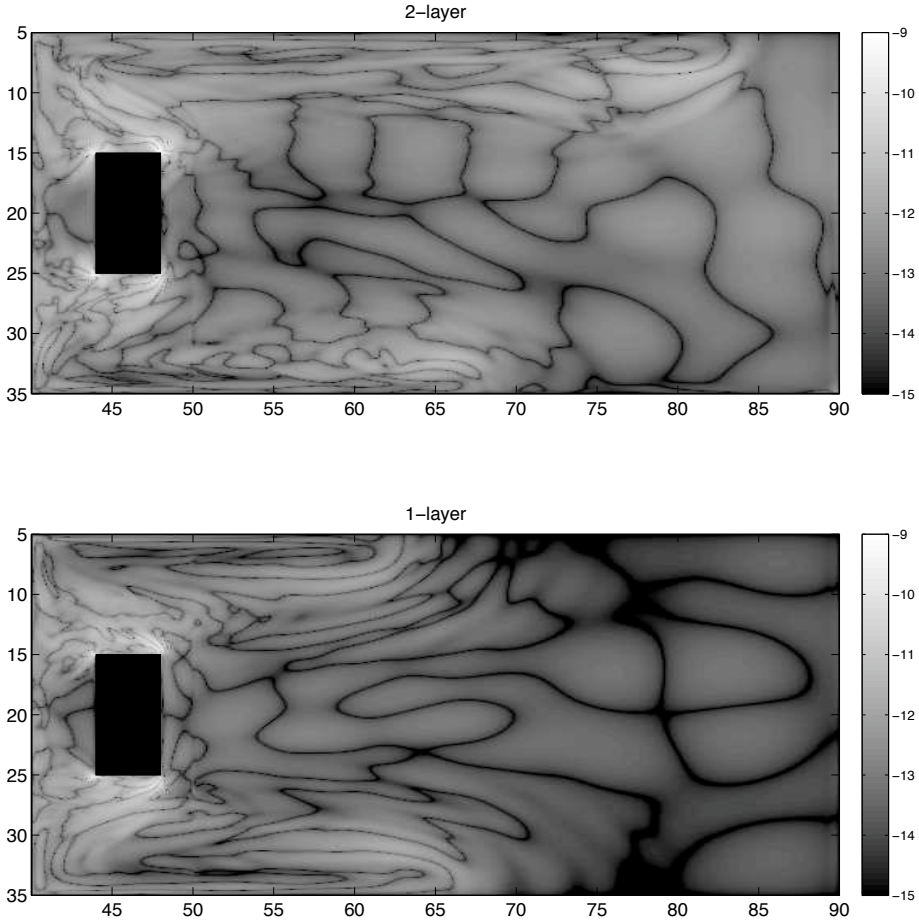

Figure 5.10: *Logarithm of the absolute value of the divergence of the eddy stresses for the two transient simulations with* $\tau_0 = 0.2\,N/m^2$. *The darker, meandering lines appear when the absolute value of the divergence term approaches zero and indicate therefore the borders between areas with positive and negative divergence terms. The divergence of the eddy stresses of the 2-layer case is much stronger than for the 1-layer case.*

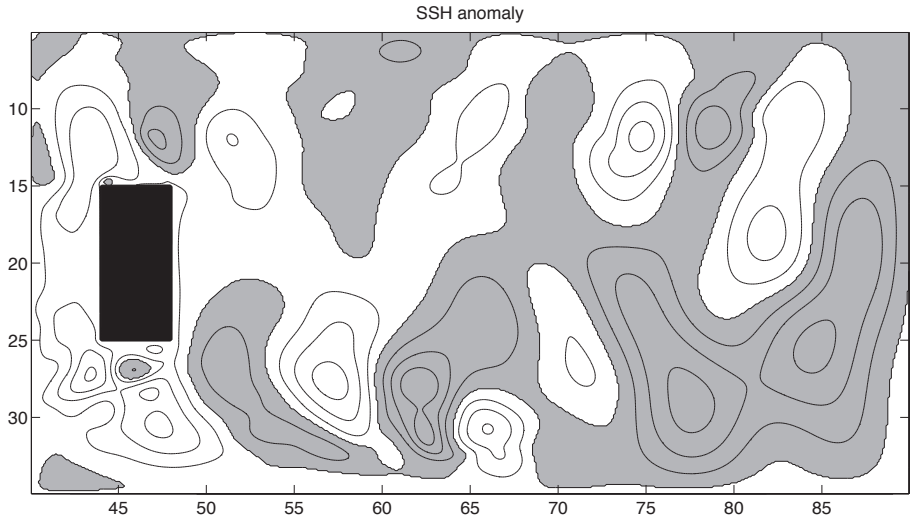

Figure 5.11: *A snapshot of the sea surface height anomaly (relative to the time mean) at day 169 of the 180-days restart of the 2-layer case with symmetrical wind forcing and* $\tau_0 = 0.2\,N/m^2$*. The contour interval is 10 cm and gray areas denote negative values. Eddies are formed north and south of the island.*

$10^{-12}s^{-2}$, which is the same size as the wind-stress term. Moreover, this leads to time-mean velocities in the order of 10 cm/s according to the $\beta\bar{v}$-term in equation (5.5). These areas have been shaded in Figure 5.12. In the 2-layer case, the rectification by the divergence term is relevant in larger areas than in the 1-layer case, especially in the northern half of the basin. North of the island, this area is larger than south of the island, probably because of the asymmetric mean flow field of the 2-layer simulation (Figure 5.6). In the 2-layer case, the divergence term is also relevant in the north-east of the basin. The eddy stresses thus affect the mean circulation in the 2-layer case more than in the 1-layer case.

A similar analysis can be conducted for the barotropic Rossby modes. Then, the velocity and relative vorticity fields that are used in eq. (5.5) should be derived from the sea surface height field. Qualitatively similar results are found when comparing the divergence of the eddy stresses of these modes (Figure 5.13): the largest divergence is found near the corners and north and south boundaries of the island, and the ratio of this term between the 2-layer and 1-layer case is about a factor 10^2 in regions close to the island. For the Rossby basin modes, the divergence of the eddy stresses is very weak, compared to the divergence of the eddy stresses of the total variability field. This term is only relevant near the corners of the island. The strengths of the divergence of the

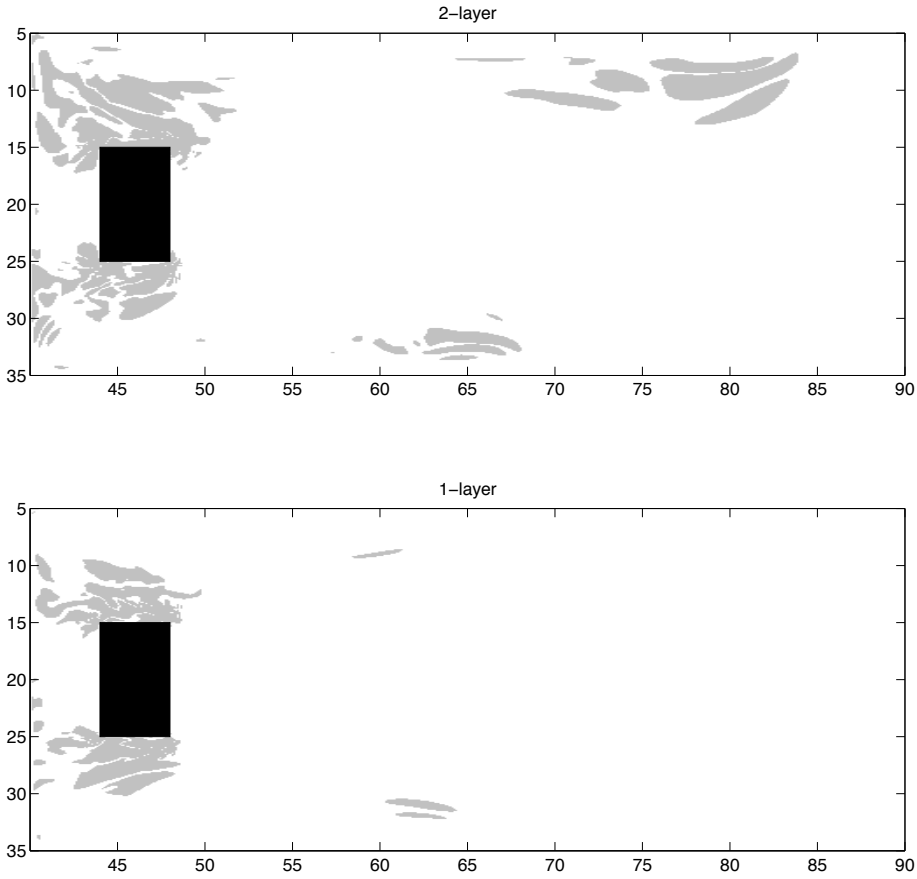

Figure 5.12: *Areas in which the absolute value of the divergence of the eddy stresses (Figure 5.10) is larger than $10^{-12}s^{-2}$. In these areas, the rectification of the velocities is in the order of 10 cm/s. The 2-layer case has a much larger region where the divergence of the eddy stresses is relevant than the 1-layer case, especially north of the island and in the northeastern corner of the basin.*

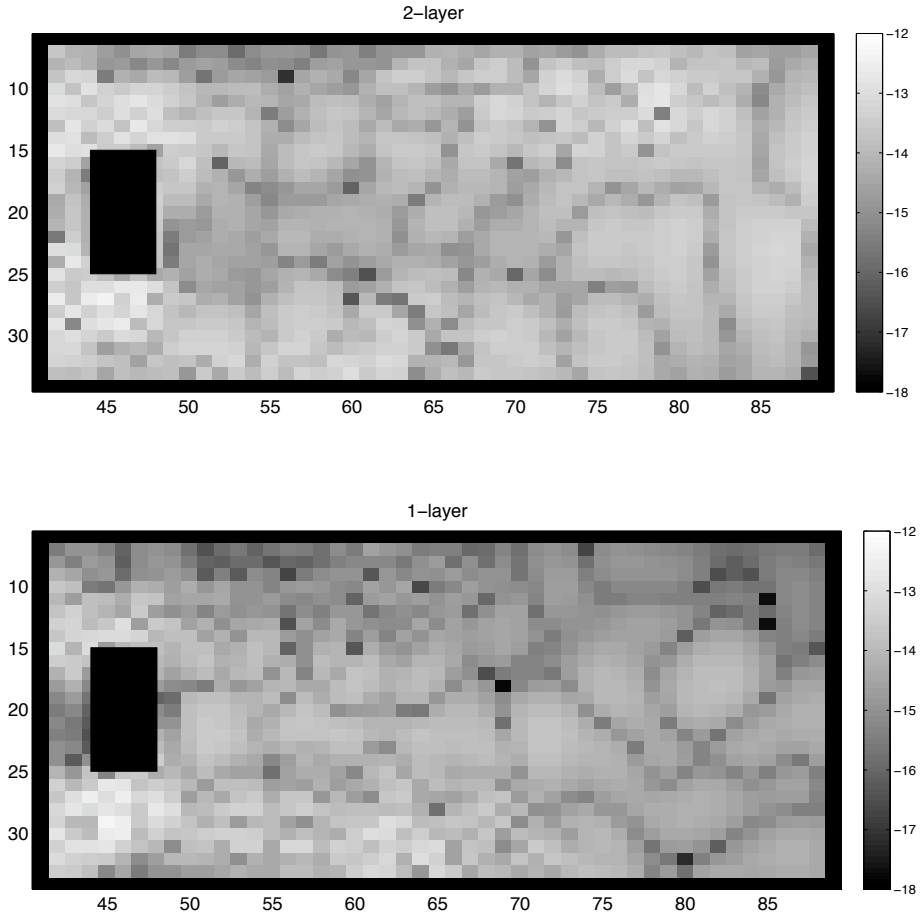

Figure 5.13: *Logarithm of the absolute value of the divergence of the eddy stresses for the first MSSA modes of the two transient simulations with* $\tau_0 = 0.2\,N/m^2$*. MSSA modes were computed from simulations with a length of 180 days and a daily-mean output frequency with sea surface height data at a* $1^\circ \times 1^\circ$ *grid. The stresses in the channel of the 2-layer case are a factor 100 stronger than for the 1-layer case. At the boundaries, the eddy stresses were not calculated.*

eddy stresses of the gyre-like modes was of the same size as the Rossby basin mode of the 1-layer case.

5.4 Conclusions and discussion

In this work, we have studied the effect of rectification on the time mean Mozambique Channel transport. A hierarchy of four models was used with increasing complexity, ranging from an analytical steady state model, to models simulating non-linear processes and barotropic and baroclinic variability. It was found that the transport in the 'channel' was very sensitive to the model type and the forcing strength. For the most realistic wind forcing (a symmetrical profile with $\tau_0 = 0.2\,N/m^2$), the time-mean volume transport estimates of the different models had a range of 3.9 ± 2.4 Sv. In this case, even the direction of the mean flow in the channel was not uniform between the models.

Most of the transport difference between the steady state model and the transient models was found to be related to differences in the circulation close to the north and south boundary of the basin. These lead to differences in the zonal pressure gradient in the channel and thereby to a different transport. It is not clear to what extent this mechanism is present in simulations in ocean general circulation models, as the north and south boundary in the simple set-up are not based on the real bathymetry, but on the equator and subtropical-subpolar front.

More importantly, we have also found large differences in the variability between the transient models, which might explain their different estimates of the time-mean volume transport in the channel. When comparing two transient simulations with a symmetrical wind forcing and $\tau_0 = 0.2\,N/m^2$ (a 1-layer case and a 2-layer case), we found that the channel in the 2-layer case was much more affected by a barotropic Rossby basin mode than the 1-layer case. This basin mode had a frequency of 17.8/y and influenced the sea surface height field of the channel. It is very probable that the main variability of the channel transport, which also has a frequency of 17.8/y, is caused by this basin mode. The pattern of the barotropic Rossby basin mode in the 1-layer case, on the other hand, did not occupy the channel, and the variability of the transport in the channel at this frequency was also much smaller.

Moreover, the divergence of the eddy stresses was much stronger in the 2-layer case than in the 1-layer case (a factor 10 close to the island) and these stronger stresses also occupied a larger area. The rectification by this term was found to be the most important term in the time-mean vorticity balance to affect the mean circulation. It is therefore very likely that the extra southward transport in the 2-layer case is caused by this rectification. The contribution of

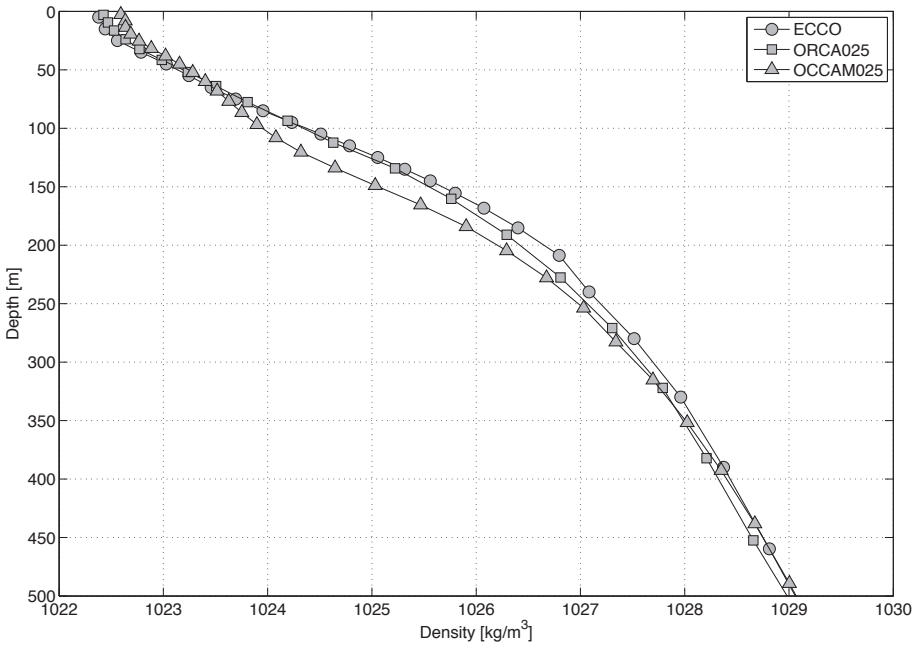

Figure 5.14: *Time- and zonal-mean density profiles of three ocean general circulation models in the Mozambique Channel at 16.5°S. The density profiles of the ECCO and ORCA025 simulations are relatively similar, while the density of OCCAM025 between 100 m and 200 m is about 0.6 kg/m^3 less. At depths deeper than 500 m, the density profiles of the three models are similar. Markers denote the depth levels of the models.*

the Rossby basin modes to the total rectification is very small. It is therefore more likely that small scale variability contributes most to the extra southward transport. The rectification is strongest north and south of the island, which is the location where eddies are formed. This is in agreement with observations of the region around Madagascar, and with other numerical models, where most of the variability is also produced at the north and south corner of the island (*Pedlosky et al.*, 1997; *Biastoch and Krauss*, 1999; *Schouten et al.*, 2003; *Palastanga et al.*, 2007; *LaCasce and Isachsen*, 2007). Further study is required to estimate the quantitative effect of the rectification on the mean transport in the channel.

An important question for further study is how the results of this study with a simplified setup are translated to more complex numerical models, such as ocean general circulation models. In the introduction of this chapter, it was shown as an example that the Mozambique Channel transport estimate of OCCAM025 was much lower than that of ECCO and ORCA025. There are many probable causes for this difference, such as for example differences in the

representation of the Indonesian Throughflow, but a difference in rectification of variability may be one of them. The OCCAM025 simulation differs from the other two simulations on some important points. First, the OCCAM025 model uses Laplacian horizontal friction, while the other two models use a biharmonic horizontal diffusion. This influences the damping of variability. Second, it was remarked in Chapter 3, that only in the OCCAM025 simulation, Mozambique Channel eddies were simulated in the Channel at 16.5°S. These eddies probably rectify the mean flow, because in this study, the areas of highest divergence of the eddy stresses were found at locations where eddies were formed. Last, the density gradient of the OCCAM025 simulation differs slightly from the other two simulations. Between 100 m and 200 m depth, the time- and zonal-mean density in the Mozambique Channel at 16.5°S is about $0.6\,kg/m^3$ lower in OCCAM025 than in the two other models, which makes the layer with relatively low densities about 30 m thicker (Figure 5.14). This difference at least influences the effect of the wind on the variability of the top layers.

The above results suggest that the range in time-mean transport estimates in the ocean general circulation models might be caused by rectification of variability. However, the variability in these models should be quantified to verify this statement. Moreover, the quantitative effect of the variability should be calculated to show whether rectification can explain the deviation of the estimated time-mean transport in the models to the observed value.

6

Summary and Outlook

The aim of this dissertation was to study the variability of the Mozambique Channel throughflow in the range from eddy to interannual time scales and to investigate the origin of this variability. The 4.2-year time series obtained by a mooring array in the Mozambique Channel at 17°S as part of the LOCO project was the main object of study, together with output from (ocean general circulation) models and satellite observations. In this last chapter, a summary will be given of the main results. Also, some of the main issues that should be addressed in future studies will be discussed.

6.1 Variability at a range of time scales

Thus far, the LOCO project obtained a successful data series for assessing the mean and variability of the Mozambique Channel throughflow. Over the length of the time series, the mean volume transport has been estimated at 16.7 Sv southward, with daily values ranging between 45 Sv northward and 65 Sv southward (section 2.4.1).

The throughflow is highly variable on a large range of time scales. Interannual variability was observed both in volume transport and in the subsurface salinity in the Mozambique Channel. The amplitude of these variations was found to be large, in the order of 9 Sv for the transport time series (section 2.4.2) and about 0.2 PSU for a salinity anomaly (section 4.2).

The interannual variability of the transport time series has a dominant period of two years and is related to the Indian Ocean Dipole (IOD) index. If the phase of the IOD is negative, the tropical gyre strengthens, which in its turn strengthens the South Equatorial Current. The southward volume transport in the Mozambique Channel is positively correlated to the westward transport

in the South Equatorial Current with a lag of about 8 – 9 months (section 2.4.3). Because previous studies (*Schouten et al.*, 2002b; *Palastanga et al.*, 2006) also found a relation between the IOD index and the eddy activity in the Channel (section 1.3.1), it can thus be concluded that the IOD variability in the equatorial Indian Ocean is of great importance to the Mozambique Channel throughflow.

The salinity anomaly in the years 2000 – 2001 was found to be related to the strength of the South Equatorial Current as well (section 4.4). In three ocean general circulation models (ECCO, OCCAM and POP), a low-frequency increase of the salinity in the Mozambique Channel is correlated to the weakening of the northern part of the South Equatorial Current. This results in a reduced flow of tropical, relatively fresh waters towards Madagascar. The salinity anomaly in the models propagated southward into the Agulhas Current and northward along the African coast. It is also correlated to a salinity anomaly found in the Southeast Madagascar Current (section 4.5, *Nauw et al.*, 2008).

In the volume transport, also a seasonal cycle was observed, where none was found in the salinity concentration of the upper layers. The seasonal cycle of the transport has an amplitude of about 5 Sv and originates from upstream variability in the wind forcing west of the Mid Indian Ridge (sections 2.4.3 and 3.3.2). When the seasonal cycle and the interannual variability of the volume transport are in phase, some very large variations in the transport may arise (section 2.4.2). The seasonal cycle in the transport time series is overshadowed by variability at other frequencies, and therefore it was not detected in previous research. In ocean general circulation models on the other hand, this frequency dominates the throughflow, as these models underrepresent variability at other, especially higher, frequencies (section 3.3).

Variability at the eddy time scale (5/y – 6/y) is very strong in the observed volume transport time series. In section 3.4, it is suggested that this is due to the formation of Mozambique Channel eddies, which happens frequently around the location of the mooring section. The alternation between a strong southward current and the eddies formed out of this current is causing a strong 5/y – 6/y signal. In the eddy resolving ocean general circulation models, this signal is much weaker, although the velocity structure of the eddies in these models are quite well simulated. However, the eddies are formed further upstream and therefore no alternation takes place at the mooring section. The simulation of a signal at the 5/y – 6/y frequency in the volume transport is thus very subtle and locally generated. A correct simulation of intra-annual variability in the sea surface height of the Indian Ocean basin (section 1.3.1) does not imply that the intra-annual variability in the Mozambique Channel

transport is correctly simulated as well.

It is very important to correctly simulate the variability in the Indian Ocean. Not only to assess the role of the Mozambique Channel throughflow variability in the global ocean circulation, but also to simulate the mean state of the throughflow. In Chapter 5, it was shown that the estimated transport through the channel is sensitive to the model setup and the simulation of barotropic and / or baroclinic variability. Rectification of the mean flow by this variability was found to be strongest along the north and south boundary of the island. Also, the amount of rectification was found to be sensitive to the basin setup. This sensitiveness is a probable explanation for large differences in the estimation of the mean volume transport in numerical models.

6.2 Remaining questions

Many aspects of the variability in the Mozambique Channel throughflow still need to be clarified. First, there is still a large uncertainty in the variability of the Mozambique Channel throughflow at long time scales due to the relative short time series. Second, many questions remain on the formation of Mozambique Channel eddies. Last, and most importantly, we need to understand how variability in the Mozambique Channel influences the Agulhas region and thereby the inter-ocean exchange around South Africa.

It is very probable that transport variability at frequencies lower than the quasi-biennial frequency will be found in a longer time series. Important periods that can be expected are 3 – 5 years, because of the El Niño / Southern Oscillation variability, and trends because of the variability in the overturning circulation (section 1.3.2). An indication for this is that a southward increasing trend in the low-frequency variability band of the transport has already been observed (Figure 2.10). Also, a low-frequency oscillation in the salinity of the upper layers in the Mozambique Channel is possible, of which the salinity anomaly described in Chapter 4 is part. An additional advantage of a longer time series is that the estimate of the mean volume transport will be more precise. Finally, a longer time series could be beneficial for the correlation between the Indian Ocean Dipole index and the volume transport, which had to be derived indirectly via a correlation with the South Equatorial Current in section 2.4.3. It is hoped that a longer time series will improve the direct correlation between the two timeseries to a significant level.

The mooring section in the Mozambique Channel is being maintained until at least late 2011, which leads to a total time series at the end of the project with a length of over 8 years. This time length is just enough to proof the direct correlation between the IOD and the transport through the Mozambique

Channel at an 80% confidence level: when assuming that the correlation coefficient between the two time series and its lag is well measured in the 4.2-year time series, a time series length of at least 7.7 years is needed. This length probably also suffices to measure the influence of the El Niño / Southern Oscillation variability on the Mozambique Channel transport, as then more than one period of this cycle has passed. When the time series has captured a full cycle of the El Niño / Southern Oscillation, this also improves the estimate of the mean transport.

Another important question in the context of interannual variability is why the numerical models studied in Chapter 3 underestimate the variability of the transport at long time scales (Figure 3.4). The simulation times in all of these models is much longer than the time series length of the LOCO program, so these models should simulate at least several periods of the IOD cycle. Because the IOD signal is found both in the ocean and in the atmosphere (section 1.3.2), it should be part of the atmospheric forcing of the numerical models. Moreover, the effects of the IOD on the temperature fields in the tropical Indian Ocean have been simulated by several models (*Vinayachandran et al.*, 2007; *Sasaki et al.*, 2008, both MOM based). There are several possible reasons why the correlation between the IOD and the transport in the Mozambique Channel is different in the numerical models. The numerical models might simulate the sea surface anomalies related to the IOD wrongly. Alternatively, the correlation between the strength of the SEC and the volume transport in the Mozambique Channel might be differently simulated in the models. It is important to study this connection in numerical models, as we might want to predict the influence of the IOD on the Mozambique Channel transport in, for example, a changing climate.

Most of the present knowledge of Mozambique Channel eddy formation has been deduced from the two-dimensional LOCO mooring section and from sea surface altimetry measurements. This leaves many questions unanswered, as the formation mechanism is three-dimensional and takes partly place close to the Mozambican coast where the altimetry measurements are unreliable. The formation mechanism as proposed by *Ridderinkhof and De Ruijter* (2003) and *Harlander et al.* (2009) is very probable, but could not be proven thus far. It is also possible that not all eddies are formed similarly. One indication for this is the varying amplitude of the variability at the eddy time scale. As noted in section 2.4.1, the 5/y – 6/y signal of the volume transport in the first deployment period was stronger than that of the second and third period. Nevertheless, no clear shift in the formation area of eddies was observed over the time series. It is not understood why the strength of the signal at this frequency fluctuates, but one possible explanation could be related to a varying formation

mechanism of the eddies.

To understand the formation mechanism of the eddies, it is important to study the flow just north of the mooring section. What kind of instability can be found in the southward current flowing along the Mozambican coast? Is the eddy formation related to the dissolving eddies at the northern entrance of the Channel (section 3.4)? Why are the northerly eddies in the observations dissolving and why does this not happen in the numerical models? These questions are best answered by hydrographic measurements of the velocity structure in the southward current along the Mozambican coast and of eddies in the northern part of the Mozambique Channel. In this context, it is a large drawback that the state-of-the-art numerical models simulate eddy formation so differently from the real ocean so that we cannot use them in answering these questions.

Part of these questions might also be assessed more indirectly by investigating the properties of the eddies. A classification system of eddies should be developed, by which eddies are sorted on their strength, shape and water mass characteristics. This classification should then be compared to periods with high and low amplitudes of the 5/y – 6/y variability. Are the eddies in periods with high 5/y – 6/y variability significantly different from eddies in periods with low 5/y – 6/y variability? And can their properties be related to their formation? For example, if the eddies in periods of high and low 5/y – 6/y variability differ mainly in strength and / or shape, the varying strength of the 5/y – 6/y variability might be mainly due to the strength of the southward current. On the other hand, if these eddies differ mainly in water mass characteristics, the origin of the instability of the southward current that forms the eddy might be the difference. The periods with high and low 5/y – 6/y variability should be deduced from the transport time series by wavelet analysis. Unfortunately in the present time series, periods with strong 5/y – 6/y variability are found only at the beginning of the time series. In a longer observational transport time series, periods with high 5/y – 6/y variability will occur more often and a better correlation between these periods and eddy characteristics can be made.

The last set of questions concerns the influence of the variability in the Mozambique Channel throughflow on the inter-ocean exchange around South Africa. Is the strength of the Agulhas Current correlated to the transport through the Mozambique Channel? Or is this influence negligible, because of a probable anti-correlation between the different sources of the Agulhas Current, for example between the Mozambique Channel transport and the Southeast Madagascar Current strength. If the Mozambique Channel transport is correlated to the Agulhas Current strength, is the latter then also related to the quasi-biennial IOD index? Because the inter-ocean exchange is inversely

correlated to the Agulhas Current strength (*Van Sebille et al.*, 2009b), this would infer that the variability in the inter-ocean exchange is related to large scale patterns in the tropical Indian Ocean. Also, it should be studied which part of the inter-ocean exchange originates from the Mozambique Channel and whether salinity and temperature anomalies, such as the salinity anomaly of 2000 – 2001, propagate towards the South Atlantic Ocean or if they return to the Indian Ocean via the Agulhas Return Current. In this context it is also important to study the correlation between the salinity or temperature and the transport in the Mozambique Channel.

In the near future, new data sets will be available to answer most of these questions. A mooring array will be placed in the Agulhas Current (*L. M. Beal, personal communication*, 2009), with which its velocity structure will be measured. The mooring array itself will be operational for three years, and a longer time series is tried to be achieved by correlating the mooring array data with a track of Topex/Poseidon altimetry. The correlation between this data and the LOCO section will show the possible connection between the large-scale variability in the circulation of the tropical Indian Ocean and the inter-ocean exchange. The Agulhas mooring array will not contain temperature and salinity measurements. This is quite unfortunate, as this means data from this new mooring array cannot be used to assess the correlation between the water mass characteristics in the Mozambique Channel and the Agulhas Current. However, the number of Argo floats in the Southwestern Indian Ocean increases, and thereby the density of salinity and temperature profiles, which could be an alternative to assess this correlation.

The role of ocean general circulation models in answering the questions on the inter-ocean exchange is not sure. As discussed above, these models underrepresent the low- and high-frequency variability in the Mozambique Channel transport. It is therefore probable that also the variability downstream in the Agulhas Current in these models is underrepresented, but this has to be verified with observational data, possibly from the future Agulhas Current mooring section. Data assimilation applied for example on the sea surface height fields might improve the low-frequency variability in the circulation of numerical models. In the ECCO model, which applies data assimilation amongst others on the sea surface height field, already a small peak in the variability at the quasi-biennial time scale in the Mozambique Channel transport can be found (Figure 3.4). This is a hopeful result, as the ECCO model has a relatively low horizontal resolution compared to the Mozambique Channel width. It would also be very interesting to apply data assimilation on the velocity, salinity and temperature data of the LOCO section, as this could improve the representation of the heat and salt fluxes in the OGCMs.

Although the eddies in the high-resolution models are formed at the wrong location (section 3.4), their strength and shape is quite well simulated. According to a numerical study by *Biastoch et al.* (2008b), their influence on the inter-ocean exchange volume flux is also sufficiently simulated. However, variability in strength, shape and number of eddies in the models should be compared with observations to be able to assess the influence of this kind of variability on downstream processes. Therefore, when using ocean general circulation models to study the influence of the variability in the Southwest Indian Ocean on the global ocean circulation, one should validate not only the mean state of the models but also the simulated variability. It is hoped that the models will be improved accordingly.

Bibliography

Alves, M. L. G. R., and A. Colin de Verdiere, Instability dynamics of a subtropical jet and applications to the Azores Front Current System: Eddy-driven mean flow, *J. Phys. Oceanogr.*, *29*(5), 837–864, doi:10.1175/1520-0485, 1999.

Beal, L. M., and H. L. Bryden, Observations of an Agulhas Undercurrent, *Deep-Sea Res. I*, *44*(9-10), 1715–1724, 1997.

Beal, L. M., T. K. Chereskin, Y. D. Lenn, and S. Elipot, The sources and mixing characteristics of the Agulhas Current, *J. Phys. Oceanogr.*, *36*(11), 2060–2074, doi:10.1175/JPO2964.1, 2006.

Behera, S. K., J.-J. Luo, and T. Yamagata, Unusual IOD event of 2007, *Geophys. Res. Lett.*, *35*(L14S11), doi:10.1029/2008GL034122, 2008.

Bendat, J. S., and A. G. Piersol, *Random Data, analysis and measurement procedures, Second Edition*, John Wiley and Sons, 1986.

Berloff, P., A. M. Hogg, and W. Dewar, The turbulent oscillator: A mechanism of low-frequency variability of the wind-driven ocean gyres, *J. Phys. Oceanogr.*, *37*, 2363–2386, doi:10.1175/JPO3118.1, 2007.

Biastoch, A., and W. Krauss, The role of mesoscale eddies in the source regions of the Agulhas Current, *J. Phys. Oceanogr.*, *29*, 2303–2317, 1999.

Biastoch, A., C. J. C. Reason, J. R. E. Lutjeharms, and O. Boebel, The importance of flow in the Mozambique Channel to seasonality in the greater Agulhas Current system, *Geophys. Res. Lett.*, *26*(21), 3321–3324, 1999.

Biastoch, A., C. W. Böning, and J. R. E. Lutjeharms, Agulhas leakage dynamics affects decadal variability in Atlantic overturning circulation, *Nature*, *456*, 489–492, doi:10.1038/nature07426, 2008a.

Biastoch, A., J. R. E. Lutjeharms, C. W. Böning, and M. Scheinert, Mesoscale perturbations control inter-ocean exchange south of Africa, *Geophys. Res. Lett.*, *35*(L20602), doi:10.1029/2008GL035132, 2008b.

Biastoch, A., L. M. Beal, J. R. E. Lutjeharms, and T. G. D. Casal, Variability and coherence of the Agulhas Undercurrent in a high-resolution ocean general circulation model, *J. Phys. Oceanogr.*, *39*, 2417–2435, doi:10.1175/2009JPO4184.1, 2009.

Brodeau, L., B. Barnier, T. Penduff, A. M. Treguier, and S. Gulev, An ERA40 based atmospheric forcing for global ocean circulation models, *Ocean Modelling, submitted*, 2009.

Bryden, H. L., E. L. McDonagh, and B. A. King, Changes in ocean water mass properties: Oscillations or trends, *Science*, *300*, 2086–2088, 2003.

Cai, W., A. Sullivan, and T. Cowan, How rare are the 2006–2008 positive Indian Ocean Dipole events? An IPCC AR4 climate model perspective, *Geophys. Res. Lett.*, *36*(L08702), doi:10.1029/2009GL037982, 2009.

Cane, M. A., and D. W. Moore, A note on low-frequency Equatorial basin modes, *J. Phys. Oceanogr.*, *11*(11), 1578–1584, 1981.

Chelton, D. B., R. A. DeSzoeke, M. G. Schlax, K. El Naggar, and N. Siwertz, Geographical variability of the first baroclinic Rossby radius of deformation, *J. Phys. Oceanogr.*, *28*, 433–460, 1998.

Conkright, M. E., R. A. Locarnini, H. E. Garcia, T. D. O'Brien, T. P. Boyer, C. Stephens, and J. I. Antonov, *World Ocean Atlas 2001: Objective Analyses, Data Statistics and Figures, CD-ROM Documentation*, National Oceanographic Data Center, 2002.

Coward, A. C., and B. A. de Cuevas, The OCCAM 66 level model: Physics, initial conditions and external forcing, *Tech. Rep. 99*, SOC, 2005.

Cunningham, S., et al., Temporal variability of the Atlantic Meridional Overturning Circulation at 26.5°N, *Science*, *317*, 935–937, 2007.

De Ruijter, W. P. M., A. Biastoch, S. S. Drijfhout, J. R. E. Lutjeharms, R. P. Matano, T. Pichevin, P. J. Van Leeuwen, and W. Weijer, Indian-Atlantic interocean exchange: Dynamics, estimation and impact, *J. Geophys. Res.*, *104*(C9), 20,885–20,910, 1999.

De Ruijter, W. P. M., H. Ridderinkhof, J. R. E. Lutjeharms, M. W. Schouten, and C. Veth, Observations of the flow in the Mozambique Channel, *Geophys. Res. Lett.*, *29*(10,1502), doi:10.1029/2001GL013714, 2002.

De Ruijter, W. P. M., H. M. Van Aken, E. J. Beier, J. R. E. Lutjeharms, R. P. Matano, and M. W. Schouten, Eddies and dipoles around South Madagascar: formation, pathways and large-scale impact, *Deep-Sea Res. I*, *51*, 383–400, 2004.

De Ruijter, W. P. M., H. Ridderinkhof, and M. W. Schouten, Variability of the southwest Indian Ocean, *Phil. Trans. R. Soc. A*, *363*, 63–76, 2005.

Dijkstra, H. A., *Nonlinear Physical Oceanography: A Dynamical Systems Approach to the Large Scale Ocean Circulation and El Niño*, Atmospheric and Oceanographic Sciences Library, 2nd ed., Springer Dordrecht, 2005.

Dijkstra, H. A., and W. P. M. De Ruijter, On the physics of the Agulhas Current: Steady retroflection regimes, *J. Phys. Oceanogr.*, *31*, 2971–2985, 2001a.

Dijkstra, H. A., and W. P. M. De Ruijter, Barotropic instabilities of the Agulhas Current system and their relation to ring formation, *Journal of Marine Research*, *59*(4), 517–533, 2001b.

DiMarco, S. F., P. Chapman, W. D. Nowlin Jr., P. Hacker, K. Donohue, M. Luther, G. C. Johnson, and J. Toole, Volume transport and property distributions of the Mozambique Channel, *Deep-Sea Res. II*, *49*(7-8), 1481–1511, doi:10.1016/S0967-0645(01)00159-X, 2002.

Drbohlav, H.-K. L., S. Gualdi, and A. Navarra, A diagnostic study of the Indian Ocean Dipole Mode in El Niño and non-El Niño years, *J. of Climate*, *20*, 2961–2977, 2007.

Dukowicz, J. K., and R. D. Smith, Implicit free-surface method for the Bryan-Cox-Semtner ocean model, *J. Geophys. Res.*, *99*(C4), 7991–8014, 1994.

Duncan, C. P., The Agulhas Current, Ph.D. thesis, University of Hawaii, 1970.

Feng, M., and G. Meyers, Interannual variability in the tropical Indian Ocean: A two-year time-scale of Indian Ocean Dipole, *Deep-Sea Res. II*, *50*, 2263–2284, doi:10.1016/S0967-0645(03)00056-0, 2003.

Feron, R. C. V., W. P. M. De Ruijter, and D. Oskam, Ring shedding in the Agulhas Current System, *J. Geophys. Res.*, *97*(C6), 9467–9477, 1992.

Feron, R. C. V., W. P. M. De Ruijter, and P. J. Van Leeuwen, A new method to determine the mean sea surface dynamic topography from satellite altimeter observations, *J. Geophys. Res.*, *103*(C1), 1343–1362, 1998.

Ffield, A., J. Toole, and D. Wilson, Seasonal circulation in the South Indian Ocean, *Geophys. Res. Lett.*, *24*(22), 2773–2776, 1997.

Firing, E., B. Qiu, and W. Miao, Time-dependent island rule and its application to the time-varying North Hawaiian Ridge Current, *J. Phys. Oceanogr.*, *29*, 2671–2688, 1999.

Franzese, A. M., S. R. Hemming, and S. L. Goldstein, Use of strontium isotopes in detrital sediments to constrain the glacial position of the Agulhas Retroflection, *Paleoceanography*, *24*(PA2217), doi:10.1029/2008PA001706, 2009.

Ganachaud, A., C. Wunch, J. Marotzke, and J. M. Toole, Meridional overturning and large-scale circulation of the Indian Ocean, *J. Geophys. Res.*, *105*(C11), 26,117–26,134, 2000.

Gent, P. R., and J. C. McWilliams, Isopycnal mixing in ocean circulation models, *J. Phys. Oceanogr.*, *20*(1), 150–155, doi:10.1175/1520-0485, 1990.

Ghil, M., et al., Advanced spectral methods for climatic time series, *Rev. Geophys.*, *40*(1), 3.1–3.41, doi:10.1029/2000GR000092, 2000.

Godfrey, J. S., A Sverdrup model of the depth-integrated flow for the world ocean allowing for island circulations, *Geophys. Astrophys. Fluid Dynamics*, *45*, 89–112, 1989.

Gordon, A. L., Indian-Atlantic transfer of thermocline water at the Agulhas retroflection, *Science*, *227*(4690), 1030–1033, doi:10.1126/science.227.4690.1030, 1985.

Gordon, A. L., Interocean exchange of thermocline water, *J. Geophys. Res.*, *91*(C4), 5037–5046, 1986.

Gordon, A. L., S. Ma, D. B. Olson, P. Hacker, A. Ffield, L. D. Talley, D. Wilson, and M. Baringer, Advection and diffusion of Indonesian throughflow water within the Indian Ocean South Equatorial Current, *Geophys. Res. Lett.*, *24*(21), 2573–2576, 1997.

Gordon, A. L., R. D. Susanto, and A. Ffield, Throughflow within Makassar Strait, *Geophys. Res. Lett.*, *26*(21), 3325–3328, 1999.

Griffies, S. M., et al., Coordinated ocean-ice reference experiments (COREs), *Ocean Modelling*, *26*(1-2), 1–46, doi:10.1016/j.ocemod.2008.08.007, 2008.

Hallberg, R., Stable split time stepping schemes for large-scale ocean modeling, *J. of Computational Physics*, *135*(CP975734), 54–65, 1997.

Harlander, U., H. Ridderinkhof, M. W. Schouten, and W. P. M. De Ruijter, Long term observations of transport, eddies, and Rossby waves in the Mozambique Channel, *J. Geophys. Res.*, *114*(C02003), doi:10.1029/2008JC004846, 2009.

Harris, T. F. W., Sources of the Agulhas Current in the spring of 1964, *Deep-Sea Res.*, *19*, 633–650, 1972.

Hermes, J. C., C. J. C. Reason, and J. R. E. Lutjeharms, Modeling the variability of the greater Agulhas Current system, *J. of Climate*, *20*, 3131–3146, doi:10.1175/JCLI4154.1, 2007.

Horii, T., H. Hase, I. Ueki, and Y. Masumoto, Oceanic precondition and evolution of the 2006 Indian Ocean dipole, *Geophys. Res. Lett.*, *35*(L03607), doi:10.1029/2007GL032464, 2008.

Johns, W. E., T. N. Lee, D. Zhang, R. Zantopp, C. T. Liu, and Y. Yang, The Kuroshio east of Taiwan: Moored transport observations from the WOCE PCM-1 array, *J. Phys. Oceanogr.*, *31*, 1031–1051, 2001.

Karstensen, J., and D. Quadfasel, Variability of water mass transformation and formation in the Southern Hemisphere, *Exchanges*, *22*, 2001.

Karstensen, J., and D. Quadfasel, Water subducted into the Indian Ocean subtropical gyre, *Deep-Sea Res. II*, *49*(7-8), 1441–1457, doi:10.1016/S0967-0645(01)00160-6, 2002a.

Karstensen, J., and D. Quadfasel, Formation of Southern Hemisphere thermocline waters: Water mass conversion and subduction, *J. Phys. Oceanogr.*, *32*, 3020–3038, 2002b.

Karstensen, J., and M. Tomczak, Ventilation processes and water mass ages in the thermocline of the southeast Indian Ocean, *Geophys. Res. Lett.*, *24*(22), 2777–2780, 1997.

Katsman, C. A., H. A. Dijkstra, and S. S. Drijfhout, The rectification of wind-driven flow due to its instabilities, *Journal of Marine Research*, *56*(3), 559–587, doi:10.1357/002224098765213586, 1998.

Keller, H. B., *Applications of Bifurcation Theory*, chap. Numerical solution of bifurcation and nonlinear eigenvalue problems, pp. 359–384, Academic Press, 1977.

Kistler, R., et al., The NCEP-NCAR 50-year reanalysis: Monthly means CD-ROM and documentation, *Bulletin of the American Meteorological Society*, *82*(2), 247–267, 2001.

KNMI, Indian Ocean: Oceanographic and meteorological data, *Atlas 135*, Koninklijk Nederlands Meteorologisch Instituut, 1952.

LaCasce, J. H., and P. E. Isachsen, On Sverdrup discontinuities and vortices in the southwest Indian Ocean, *J. Phys. Oceanogr.*, *37*, 2940–2950, doi:10.1175/2007JPO3652.1, 2007.

Large, W. G., J. C. McWilliams, and S. C. Doney, Oceanic vertical mixing: A review and a model with a non-local boundary layer parameterzation., *Reviews of Geophysics*, *32*(4), 363–403, 1994.

Lee, T., Decadal weakening of the shallow overturning ciruclation in the South Indian Ocean, *Geophys. Res. Lett.*, *31*(L18305), doi:10.1029/2004GL020884, 2004.

Lee, T., and M. J. McPhaden, Decadal phase change in large-scale sea level and winds in the Indo-Pacific region at the end of the 20th century, *Geophys. Res. Lett.*, *35*(L01605), doi:10.1029/2007GL032419, 2008.

Liu, Z., L. Wu, and E. Bayler, Rossby Wave-Coastal Kelvin Wave interaction in the extratropics. Part I: Low-frequency adjustment in a closed basin, *J. Phys. Oceanogr.*, *29*, 2382–2404, 1999a.

Liu, Z., L. Wu, and H. Hurlburt, Rossby Wave-Coastal Kelvin Wave interaction in the extratropics. Part II: Formation of island circulation, *J. Phys. Oceanogr.*, *29*, 2405–2418, 1999b.

Lutjeharms, J. R. E., *The Agulhas Current*, Springer-Verlag Berlin, 2006.

Lutjeharms, J. R. E., and R. C. Van Ballegooyen, The retroflection of the Agulhas Current, *J. Phys. Oceanogr.*, *18*(11), 1570–1583, doi:10.1175/1520-0485, 1988.

Madec, G., NEMO ocean engine, Tech. rep. 27, *Tech. rep.*, Institut Pierre Simon Laplace (IPSL), France, 2006.

Maltrud, M. E., and J. L. McClean, An eddy resolving global $1/10^{\circ}$ ocean simulation, *Ocean Modelling*, *8*, 31–54, doi:10.1016/j.ocemod.203.12.001, 2005.

Marshall, J., A. Adcroft, C. Hill, L. Perelman, and C. Heisey, A finite-volume, incompressible Navier Stokes model for studies of the ocean on parallel computers, *J. Geophys. Res.*, *102*(C3), 5753–5766, 1997.

Masumoto, Y., T. Horii, I. Ueki, H. Hase, K. Ando, and K. Mizuno, Short-term upper-ocean variability in the central equatorial Indian Ocean during 2006 Indian Ocean Dipole event, *Geophys. Res. Lett.*, *35*(L14S09), doi:10.129/2008GL033834, 2008.

Matano, R. P., E. J. Beier, P. T. Strub, and R. Tokmakian, Large-scale forcing of the Agulhas variability: The seasonal cycle, *J. Phys. Oceanogr.*, *32*, 1228–1241, 2002.

Matano, R. P., E. J. Beier, and P. T. Strub, The seasonal variability of the circulation in the South Indian Ocean: Model and observations, *Journal of Marine Systems*, *74*(1-2), 315–328, doi:10.1016/j.jmarsys.2008.01.007, 2008.

McDonagh, E. L., H. L. Bryden, B. A. King, R. J. Sanders, S. A. Cunningham, and R. Marsh, Decadal changes in the South Indian Ocean thermocline, *J. of Climate*, *18*, 1575–1590, 2005.

Menemenlis, D., I. Fukumori, and T. Lee, Using Green's functions to calibrate an ocean general circulation model, *Monthly Weather Review*, *133*, 1224–1240, 2005.

Meyers, G., P. McIntosh, L. Pigot, and M. Pook, The years of El Niño, La Niña, and interactions with the tropical Indian Ocean, *J. of Climate*, *20*, 2872–2880, doi:10.1175/JCLI4152.1, 2007.

Murtugudde, R., S. Signorini, J. Christian, A. Busalacchi, and C. McClain, Ocean color variability of the tropical Indo-Pacific basin observed by SeaWiFS during 1997-98, *J. Geophys. Res.*, *104*(18), 351–18 366, 1999.

Nauw, J. J., and H. A. Dijkstra, The origin of low-frequency variability of double-gyre wind-driven flows, *Journal of Marine Research*, *59*, 567–597, 2001.

Nauw, J. J., H. M. Van Aken, J. R. E. Lutjeharms, and W. P. M. De Ruijter, Intrathermocline eddies in the Southern Indian Ocean, *J. Geophys. Res.*, *111*(C03006), doi:10.1029/2005JC002917, 2006.

Nauw, J. J., H. M. Van Aken, A. Webb, J. R. E. Lutjeharms, and W. P. M. De Ruijter, Observations of the southern East Madagascar Current and undercurrent and countercurrent system, *J. Geophys. Res.*, *113*(C08006), doi:10.1029/2007JC004639, 2008.

Pacanowski, R. C., and S. M. Griffies, *The MOM 3 Manual*, GFDL Ocean Group Technical Report No.4, Princeton, NJ, NOAA/Geophysical Fluid Dynamics Laboratory, 680pp. ed., 1999.

Palastanga, V., P. J. Van Leeuwen, and W. P. M. De Ruijter, A link between low frequency meso-scale eddy variability around Madagascar and the large-scale Indian Ocean variability, *J. Geophys. Res.*, *111*(C09029), doi:10.1029/2005JC003081, 2006.

Palastanga, V., P. J. Van Leeuwen, and W. P. M. De Ruijter, Flow structure and variability in the subtropical Indian Ocean: Instability of the South Indian Ocean Countercurrent, *J. Geophys. Res.*, *112*(C01001), doi:10.1029/2005JC003395, 2007.

Palastanga, V., H. A. Dijkstra, and W. P. M. De Ruijter, Inertially induced connections between subgyres in the South-Indian Ocean, *J. Phys. Oceanogr.*, *39*, 465–471, doi:10.1175/2008JPO3872.1, 2009.

Pedlosky, J., *Geophysical Fluid Dynamics*, second ed., Springer-Verlag New York Inc., 1987.

Pedlosky, J., L. J. Pratt, M. A. Spall, and K. R. Helfrich, Circulation around islands and ridges, *Journal of Marine Research*, *55*, 1199 – 1251, 1997.

Penduff, T., DRAKKAR: Hiérarchie de modèles glace-océan pour l'étude du climat, *La lettre trimestrielle Mercator Océan*, (16), 2–3, 2005.

Penven, P., J. R. E. Lutjeharms, and P. Florenchie, Madagascar: A pacemaker for the Agulhas Current system?, *Geophys. Res. Lett.*, *33*(L17609), doi:10.1029/2006GL026854, 2006.

Phillips, H. E., S. E. Wijffels, and M. Feng, Interannual variability in the freshwater content of the Indonesian-Australian Basin, *Geophys. Res. Lett.*, *32*(L03603), doi:10.1029/2004GL021755, 2005.

Pratt, L., and J. Pedlosky, Barotropic circulation around islands with friction, *J. Phys. Oceanogr.*, *28*, 2148–2162, 1998.

Quadfasel, D. R., and J. C. Swallow, Evidence for 50-day period planetary waves in the South Equatorial Current of the Indian Ocean, *Deep-Sea Res.*, *33*(10), 1307–1312, 1986.

Quartly, G. D., and M. A. Srokosz, Eddies in the southern Mozambique Channel, *Deep-Sea Res. II*, *51*, 69–83, doi:10.1016/j.dsr2.2003.03.001, 2004.

Rahmstorf, S., Ocean circulation and climate during the past 120,000 years, *Nature*, *419*, 207–214, doi:10.1038/nature01090, 2002.

Rao, S. A., S. K. Behera, Y. Masumoto, and T. Yamagata, Interannual subsurface variability in the Tropical Indian Ocean with a special emphasis on the Indian Ocean Dipole, *Deep-Sea Res. II*, *49*, 1549–1572, 2002.

Reason, C. J. C., R. J. Allan, J. A. Lindesay, and T. J. Ansell, ENSO and climatic signals across the Indian Ocean Basin in the global context: Part I, Interannual composite patterns, *International Journal of Climatology*, *20*(11), 1285–1327, doi: 10.1002/1097-0088, 2000.

Redi, M. H., Oceanic isopycnal mixing by coordinate rotation, *J. Phys. Oceanogr.*, *12*(10), 1154–1158, doi:10.1175/1520-0485, 1982.

Ridderinkhof, H., RSS Discovery cruise report: Cruise D289B - Mozambique Channel, 26 February – 15 March 2005, *Tech. rep.*, Royal NIOZ, 2005.

Ridderinkhof, H., FS METEOR cruise report: Cruise M75-1B - Mozambique Channel, 19 january – 4 february 2008, *Tech. rep.*, Royal NIOZ, 2008.

Ridderinkhof, H., and W. P. M. De Ruijter, Moored current observations in the Mozambique Channel, *Deep-Sea Res. II*, *50*, 1933–1955, 2003.

Ridderinkhof, H., and G. D. Quartly, RSS Discovery cruise report: Cruise D301B and D302 - Indian Ocean, 20 March – 11 April 2006, *Tech. rep.*, Royal NIOZ and NOC, 2006.

Ridderinkhof, H., P. M. Van der Werf, J. Ullgren, P. J. Van Leeuwen, H. M. Van Aken, and W. P. M. De Ruijter, Seasonal and interannual variability in the Mozambique Channel from moored current observations, *J. Geophys. Res. submitted*, 2009.

Rouault, M., P. Penven, and B. Pohl, Warming in the Agulhas Current system since the 1980's, *Geophys. Res. Lett.*, *36*(L12602), doi:10.1029/2009GL037987, 2009.

Saetre, R., and A. Jorge da Silva, The circulation of the Mozambique Channel, *Deep-Sea Res.*, *31*(5), 485–508, 1984.

Saji, N. H., B. N. Goswami, P. N. Vinayachandran, and T. Yamagata, A dipole mode in the tropical Indian Ocean, *Nature*, *401*, 360–363, 1999.

Sasaki, H., M. Nonaka, Y. Masumoto, Y. Sasai, H. Uehara, and H. Sakuma, An eddy-resolving hindcast simulation of the quasiglobal ocean from 1950 to 2003 on the Earth Simulator, in *High Resolution Numerical Modelling of the Atmosphere and Ocean*, edited by K. Hamilton and W. Ohfuchi, chap. 10, pp. 157–185, Springer Science+Business Media, 2008.

Schott, F., M. Fieux, J. Kindle, J. Swallow, and R. Zantopp, The boundary currents east and north of Madagascar 2. Direct measurements and model comparisons, *J. Geophys. Res.*, *93*(C5), 4963–4974, 1988a.

Schott, F. A., Shallow overturning circulation of the Western Indian Ocean, *Phil. Trans. R. Soc. A*, *363*, 2005.

Schott, F. A., and J. P. McCreary, The monsoon circulation of the Indian Ocean, *Progress in Oceanography*, *51*, 1–123, 2001.

Schott, F. A., T. N. Lee, and R. Zantopp, Variability of structure and transport of the Florida Current in the period range of days to seasonal, *J. Phys. Oceanogr.*, *18*, 1209–1230, 1988b.

Schott, F. A., M. Dengler, and R. Schoenefeldt, The shallow overturning circulation of the Indian Ocean, *Progress in Oceanography*, *53*, 2002.

Schott, F. A., S.-P. Xie, and J. P. McCreary Jr, Indian Ocean circulation and climate variability, *Rev. Geophys.*, *47*(RG1002), doi:10.1029/2007RG000245, 2009.

Schouten, M. W., W. P. M. De Ruijter, and P. J. Van Leeuwen, Upstream control of Agulhas Ring shedding, *J. Geophys. Res.*, *107*(C8, 3109), doi:10.1029/2001JC000804, 2002a.

Schouten, M. W., W. P. M. De Ruijter, P. J. Van Leeuwen, and H. A. Dijkstra, An oceanic teleconnection between the equatorial and southern Indian Ocean, *Geophys. Res. Lett.*, *29*(16, 1812), doi:10.1029/2001GL014542, 2002b.

Schouten, M. W., W. P. M. De Ruijter, P. J. Van Leeuwen, and H. Ridderinkhof, Eddies and variability in the Mozambique Channel, *Deep-Sea Res. II*, *50*, 1987–2003, 2003.

Schouten, M. W., W. P. M. De Ruijter, and H. Ridderinkhof, A seasonal intrusion of subtropical water in the Mozambique Channel, *Geophys. Res. Lett.*, *32*(L18601), doi:10.1029/2005GL023131, 2005.

Sheinbaum, J., J. Candela, A. Badan, and J. Ochoa, Flow structure and transport in the Yucatan Channel, *Geophys. Res. Lett.*, *29*(3), 1040, doi:10.1029/2001GL013990, 2002.

Siedler, G., M. Rouault, and J. R. E. Lutjeharms, Structure and origin of the subtropical South Indian Ocean Countercurrent, *Geophys. Res. Lett.*, *33*(L24609), doi:10.1029/2006GL027399, 2006.

Smith, R. D., M. E. Maltrud, F. O. Bryden, and M. W. Hecht, Numerical simulation of the North Atlantic Ocean at 1/10°, *J. Phys. Oceanogr.*, *30*, 1532–1561, 2000.

Smith, S. D., Wind stress and heat flux over the ocean in gale force winds, *J. Phys. Oceanogr.*, *10*, 709–726, 1980.

Song, Q., A. L. Gordon, and M. Visbeck, Spreading of the Indonesian Throughflow in the Indian Ocean, *J. Phys. Oceanogr.*, *34*, 772–792, 2004.

Speich, S., B. Blanke, and G. Madec, Warm and cold water routes of an OGCM conveyor belt, *Geophys. Res. Lett.*, *28*(2), 311–314, 2001.

Speich, S., B. Blanke, and W. Cai, Atlantic meridional overturning circulation and the Southern Hemisphere supergyre, *Geophys. Res. Lett.*, *34*(L23614), doi:10.1029/2007GL031583, 2007.

Sprintall, J., S. Wijffels, R. Molcard, and I. Jaya, Direct estimates of the Indonesian Throughflow entering the Indian Ocean, *J. Geophys. Res.*, *114*(C07001), doi:10.1029/2008JC005257, 2009.

Stammer, D., C. Wunsch, R. Giering, C. Eckert, P. Heimbach, J. Marotzke, A. Adcroft, C. Hill, and J. Marshall, Volume, heat, and freshwater transports of the global ocean circulation 1993–2000, estimated from a general circulation model constrained by World Ocean Circulation Experiment (WOCE) data., *J. Geophys. Res.*, *108*(C13007), doi:10.1029/2001JC001115, 2003.

Stramma, L., and J. R. E. Lutjeharms, The flow field of the subtropical gyre of the South Indian Ocean, *J. Geophys. Res.*, *102*(C3), 5513–5530, 1997.

Susanto, R. D., A. L. Gordon, and Q. Zheng, Upwelling along the coasts of Java and Sumatra and its relation to ENSO, *Geophys. Res. Lett.*, *28*(8), 1599–1602, 2001.

Swallow, J., M. Fieux, and F. Schott, The boundary currents east and north of Madagascar 1. Geostrophic currents and transports, *J. Geophys. Res.*, *93*(C5), 4951–4962, 1988.

Talley, L. D., and J. Sprintall, Deep expression of the Indonesian Throughflow: Indonesian Intermediate Water in the South Equatorial Current, *J. Geophys. Res.*, *110*(C10009), doi:10.1029/2004JC002826, 2005.

Uppala, S. M., et al., The ERA-40 re-analysis, *Quarterly Journal of the Royal Meteorological Society*, *131*(612), 2961–3012, doi:10.1256/qj.04.176, 2005.

Valsala, V. K., and M. Ikeda, Pathways and effects of the Indonesian Throughflow Water in the Indian Ocean using particle trajectory and tracers in an OGCM, *J. of Climate*, *20*, 2994–3017, 2007.

Van Aken, H. M., *The Oceanic Thermohaline Circulation - An Introduction*, Springer Science+Business Media, 2007.

Van Aken, H. M., H. Ridderinkhof, and W. P. M. De Ruijter, North Atlantic Deep Water in the south-western Indian Ocean, *Deep-Sea Res. I*, *51*(6), 755–776, doi:10.1016/j.dsr.2004.01.008, 2004.

Van Leeuwen, P. J., W. P. M. De Ruijter, and J. R. E. Lutjeharms, Natal pulses and the formation of Agulhas Rings, *J. Geophys. Res.*, *105*, 6425–6436, 2000.

Van Sebille, E., and P. J. Van Leeuwen, Fast northward energy transfer in the Atlantic due to Agulhas Rings, *J. Phys. Oceanogr.*, *37*, 2305–2315, doi:10.1175/JPO3108.1, 2007.

Van Sebille, E., C. N. Barron, A. Biastoch, P. J. Van Leeuwen, F. C. Vossepoel, and W. P. M. De Ruijter, Relating Agulhas leakage to the Agulhas Current retroflection location, *Ocean Science Discussions*, *6*, 1193–1221, 2009a.

Van Sebille, E., A. Biastoch, P. J. Van Leeuwen, and W. P. M. De Ruijter, A weaker Agulhas Current leads to more Agulhas leakage, *Geophys. Res. Lett.*, *36*(L03601), doi:10.1029/2008GL036614, 2009b.

Van Sebille, E., P. J. Van Leeuwen, A. Biastoch, and W. P. M. De Ruijter, On the fast decay of Agulhas rings, *J. Geophys. Res. in press*, 2009c.

Vinayachandran, P. N., J. Kurian, and C. P. Neema, Indian Ocean response to anomalous conditions in 2006, *Geophys. Res. Lett.*, *34*(L15602), doi:10.1029/2007GL030194, 2007.

Vranes, K., A. L. Gordon, and A. Ffield, The heat transport of the Indonesian Throughflow and implications for the Indian Ocean heat budget, *Deep-Sea Res. II*, *49*(7-8), 1391–1410, doi:10.1016/S0967-0645(01)00150-3, 2002.

Webb, D. J., B. A. de Cuevas, and A. C. Coward, The first main run of the OCCAM global ocean model, *Tech. Rep. 34*, Southampton Oceanography Centre, 1998.

Webster, P. J., A. M. Moore, J. P. Loschnigg, and R. R. Leben, Coupled ocean-atmosphere dynamics in the Indian Ocean during 1997-98, *Nature*, *401*, 356–360, 1999.

Weijer, W., W. P. M. De Ruijter, H. A. Dijkstra, and P. J. Van Leeuwen, Impact of interbasin exchange on the Atlantic overturning circulation, *J. Phys. Oceanogr.*, *29*, 2266–2284, 1999.

Wells, J. R., and K. R. Helfrich, Circulation around a thin zonal island, *J. Fluid Mech.*, *437*, 301–323, 2001.

Wyrtki, K., *Oceanographic atlas of the International Indian Ocean expedition*, National Science Foundation, 1971.

Wyrtki, K., An equatorial jet in the Indian Ocean, *Science*, *181*(4096), 262–264, 1973.

Yamanaka, G., T. Yasuda, Y. Fujii, and S. Matsumoto, Rapid termination of the 2006 El Niño and its relation to the Indian Ocean, *Geophys. Res. Lett.*, *36*(L07702), doi: 10.1029/2009GL037298, 2009.

You, Y., Seasonal variations of thermocline circulation and ventilation in the Indan Ocean, *J. Geophys. Res.*, *102*, 10,391–10,422, 1997.

You, Y., and M. Tomczak, Thermocline circulation and ventilation in the Indian Ocean derived from water mass analysis, *Deep-Sea Res. I*, *40*(1), 13–56, 1993.

Zhou, L., R. Murtugudde, and M. Jochum, Dynamics of the intraseasonal oscillations in the Indian Ocean South Equatorial Current, *J. Phys. Oceanogr.*, *38*, 121–132, 2008.

Samenvatting

Oceaanstromingen spelen een grote rol in het klimaatsysteem van de aarde, doordat ze ongeveer de helft van het warmtetransport tussen de evenaar en de polen voor hun rekening nemen. Ook zijn ze belangrijk voor veel lokale klimaten aan de rand van continenten. De gemiddelde temperatuur in Noordwest-Europa is bijvoorbeeld hoger dan je op basis van de ligging zou verwachten. Dit komt, doordat in de Noord-Atlantische Oceaan het transport van warm water in de richting van de Noordpool groter is dan in de Stille Oceaan. In de noordelijke randzeeën van de Atlantische Oceaan koelt dit water af en krijgt het een grote dichtheid, geholpen door het feit dat het water er erg zout is. Het zware water spreidt zich uit over de oceaanbodem en komt uiteindelijk weer aan de oppervlakte in de Stille en Indische Oceaan en rondom Antarctica. Vanaf hier stroomt het terug in de richting van de Atlantische Oceaan, deels via Indonesië en het zuidwesten van de Indische Oceaan. Deze circulatie wordt ook wel de 'transportband' genoemd en heeft een tijdschaal van meer dan duizend jaar. Door te bestuderen wat er in de zuidwestelijke Indische Oceaan gebeurt, proberen we een stukje van de transportband te begrijpen. Hierbij is het vooral belangrijk te weten hoeveel water er van de Indische naar de Atlantische Oceaan stroomt en hoe warm en zout dat water is.

Het transport tussen de twee oceanen vindt plaats door het afscheiden van water in de retroflectie van de Agulhasstroom. De Agulhasstroom loopt via de kust van zuidelijk Afrika naar het zuidwesten en keert ten zuiden van Zuid-Afrika terug in de richting van de Indische Oceaan. Ongeveer vier tot vijf keer per jaar scheidt een enorme wervel zich bij dit retroflectiepunt af en vloeit dan de Atlantische Oceaan in. De vorming van de wervels, en dus ook het totale transport van water, zout en warmte, wordt beïnvloed door variabiliteit bovenstrooms.

Eén van de bronnen van de Agulhasstroom is de stroming door het Mozambique Kanaal, het onderwerp van dit proefschrift. Van deze stroming is er inmiddels een mooie dataset verzameld met observaties van de snelheden, temperaturen en zoutgehaltes, die het uitgangspunt vormt voor dit onderzoek. De keuze om te meten in het Mozambique Kanaal in plaats van in de andere

bronnen, zoals de stroming ten oosten van Madagascar, is gebaseerd op twee argumenten. Ten eerste verwacht men dat variaties in de stroming door het Mozambique Kanaal een grote invloed hebben op de variaties in de transportband, omdat het Mozambique Kanaal een verbinding vormt tussen een tropische en een subtropische regio. Ten tweede is het relatief iets gemakkelijker de metingen te verrichten in een kanaal dan in een stroming langs een kust, omdat een kanaal begrensd is.

De metingen in het Mozambique Kanaal zijn een onderdeel van het LOCO-project (Long-term Ocean Climate Observations – lange-termijn oceaan klimaat observaties). Ze bestrijken inmiddels meer dan vier jaar, zodat er onderzoek kan worden gedaan naar de variabiliteit in het transport. De tijdschalen die in dit proefschrift bestudeerd worden, zijn een paar maanden tot een paar jaar groot. Het quantificeren van de variabiliteit is niet genoeg. We moeten ook begrijpen waar de variabiliteit vandaan komt, zodat we kunnen inschatten of de variabiliteit in de toekomst gelijk blijft.

De meetapparatuur van het LOCO-programma bestaat uit een set van zeven kabels met snelheidsmeters en temperatuur-zout-druk sensoren, die ongeveer op 17°S in het kanaal zijn geplaatst (zie bijvoorbeeld Figuur 2.1). De kabels zitten op de oceaanbodem vast met een gewicht en worden omhoog gehouden door grote boeien. De meeste van deze boeien bevinden zich nog zo'n 500 meter onder het zeeoppervlak, zodat de kans op beschadigingen door bijvoorbeeld vissersboten erg klein is. Elke anderhalf tot twee jaar moeten de instrumenten worden opgehaald om te worden uitgelezen en opgeknapt en worden ze teruggezet. De instrumenten zijn voor het eerst uitgezet in november 2003 en voor het laatst teruggezet in januari 2008. Dit levert dus een totale tijdsduur van 4.2 jaar op.

Een andere grote bron van observaties die gebruikt wordt in dit proefschrift, zijn metingen door satellieten. Vanuit de ruimte kunnen we de oppervlaktetemperatuur van het water meten, de windsnelheid bepalen door de hoeveelheid golven te meten en de hoogtevariaties in het oppervlak bepalen. Door de Corioliskracht zeggen de laatste iets over de variaties in de stroming.

Observaties alleen geven dus een vrij beperkt beeld van de Indische Oceaan: een aantal ver uit elkaar gelegen meetstations met kabels (waaronder LOCO) en het oceaanoppervlak. Een ander nadeel van de observaties is, dat er alleen informatie is over de meetperiode zelf en niet over bijvoorbeeld de periode daarvoor. Ook is het lastig met observaties afzonderlijke processen te bestuderen, doordat er zoveel tegelijkertijd gebeurt.

In dit proefschrift wordt daarom ook gebruik gemaakt van numerieke oceaanmodellen. Deze modellen lossen de bewegings- en dichtheidsvergelijkingen van de oceaan op. De stromingen in de modellen worden aangedreven door

de atmosfeer. Soms, zoals in hoofdstuk 3 en 4, zijn de modellen zo realistisch mogelijk. Maar in hoofdstuk 5 gebruiken we juist een model met een heel simpele topografie en atmosfeer, zodat het veel makkelijker is de verschillende processen te herkennen.

Het proefschrift begint in hoofdstuk 2 met een gedetailleerde beschrijving van de snelheidsmetingen in het LOCO-project. Ook wordt er de tijdserie van het volumetransport bepaald die in dit proefschrift wordt gebruikt. In de totale tijdserie van november 2003 tot januari 2008 bedraagt het gemiddelde zuidwaartse transport door het Mozambique Kanaal 16.7 Sv (1 Sv (*Sverdrup*) is een miljard liter per seconde ($1 \cdot 10^6\, m^3/s$), wat ongeveer gelijk is aan de hoeveelheid water die per seconde door alle rivieren op aarde stroomt). Zoals hiervoor al aangegeven is dit transport niet constant; er zijn enorme uitschieters gevonden met extremen van 45 Sv noordwaarts transport tot 65 Sv zuidwaarts transport. Het gemiddelde zoutgehalte van de bovenste lagen van het water is ongeveer 35.1 PSU (1 PSU is ongeveer 1 gram zout per kilogram water) met een afwijking van soms wel 0.2 PSU (hoofdstuk 4).

De oorsprong van deze afwijkingen wordt in dit proefschrift onderzocht per tijdschaal. Hiervoor worden de observaties en modeldata vaak eerst gefilterd, om alleen die tijdschalen over te houden waarin we geïnteresseerd zijn. In het vervolg van deze samenvatting zal ik per tijdschaal beschrijven welke variabiliteit er aanwezig was in de metingen en waar deze variabiliteit vandaan komt.

Er zijn twee signalen gevonden met een tijdschaal langer dan een jaar: één in de transportreeks en één in het zoutgehalte. Beide hebben hun oorsprong in grootschalige fluctuaties in de Indische Oceaan. Het signaal in het transport heeft een periode van zo'n twee jaar, en is dus maar twee keer voorgekomen gedurende de meetperiode. Zijn amplitude is 9 Sv en is daarmee van dezelfde orde van grootte als de gemiddelde stroming zelf (hoofdstuk 2). Deze variatie heeft te maken met de sterkte van de Indische Oceaan Dipool. Dit is een patroon in de Indische Oceaan dat wordt bepaald door hoge en lage oppervlaktetemperaturen in het westen en oosten van de tropische oceaan en dat wel wat lijkt op El Niño. De dipool beïnvloedt ook de lokale winden en stromingen. Bij een positive dipool wordt de tropische gyre verzwakt, waardoor ook de sterkte van de zuidequatoriaalstroom (de SEC in Figuur 1.3) afneemt. Aangezien de zuidequatoriaalstroom de belangrijkste toestroom van water in de richting van Madagascar is, neemt uiteindelijk ook het transport door het kanaal af. Het signaal doet er een jaar over om zich van de tropische oceaan naar het Mozambique Kanaal te verplaatsen. In die tijd is het teken van de dipool omgeklapt, zodat het net lijkt of de verzwakte stroming samengaat met een negatieve dipool.

De afwijking in het zoutgehalte is gevonden in 2000 en 2001, toen het pi-

lotproject voor LOCO plaatsvond. Het water tussen 50 en 200 meter diepte was toen 0.2 PSU zouter dan in de gehele periode 2003 tot 2008. In hoofdstuk 4 wordt uitgezocht waar dit extra zout vandaan komt. Hiervoor worden numerieke modellen gebruikt waarin eenzelfde soort afwijking voorkomt. We kunnen deze afwijking begrijpen, als we het water in het Mozambique Kanaal beschouwen als een mix van zoeter en zouter water van verschillende oorsprong. Door veranderingen in de sterkte van de zuidequatoriaalstroom nam de hoeveelheid tropisch, zoeter water af, waardoor de totale mix in 2000 en 2001 zouter werd. De modellen geven bovendien aan dat één van de oorspronkelijke bronnen zouter was geworden, waardoor het zoutgehalte van de totale mix ook toenam. Echter, elk model wijst hiervoor een andere bron aan, zodat we niet zeker kunnen zijn over dit mechanisme.

Een jaarlijks signaal is alleen gevonden in het volumetransport en niet in het zoutgehalte van het water. Het windpatroon over de zuidelijke Indische Oceaan verandert met de seizoenen en daarmee veranderen ook de belangrijkste stromingen. De positie van de zuidequatoriaalstroom verschuift in de noord-zuid richting, waardoor er soms meer en soms minder water het Mozambique Kanaal instroomt. De amplitude van dit jaarlijkse signaal is ongeveer 5 Sv.

Soms kunnen er grote veranderingen in het totale transport ontstaan als het jaarlijkse en het interjaarlijkse signaal in fase zijn. In mei 2006 bijvoorbeeld nam het transport met zowel de interjaarlijkse als de jaarlijkse frequentie toe. Hierdoor versterkte het totale transport extra snel. In oktober 2005 gebeurde precies het tegenovergestelde (hoofdstuk 2).

Het jaarlijkse signaal valt niet op in de tijdreeks van het transport, doordat die veel signalen op andere tijdschalen bevat met grote amplitudes. Hierin verschillen de numerieke modellen, die juist een heel duidelijke jaarlijkse variatie laten zien in het transport. Men dacht eerst, dat dat kwam doordat de modellen een veel te sterk jaarlijks signaal simuleren. Uit hoofdstuk 3 blijkt echter, dat de jaarlijkse signalen in de observaties en in de modellen zo goed als gelijk zijn. Wat wel verschilt, is dat de signalen op andere frequenties in de modellen veel te klein zijn, waardoor het jaarlijks signaal veel meer opvalt.

In hoofdstuk 3 wordt daarom onderzocht waarom die signalen, vooral die met een werveltijdschaal (5 tot 6 keer per jaar), ondervertegenwoordigd zijn in de numerieke modellen. Er zijn zes modellen onderzocht. Al deze modellen worden door oceanografen gebruikt om het zuidwesten van de Indische Oceaan te bestuderen. In elk ervan is de variabiliteit op de werveltijdschaal zwaar ondervertegenwoordigd. Wel doen modellen waarvan het rooster fijn genoeg is om wervels actief te simuleren, het enigszins beter dan modellen met grovere roosters. De wervels zien er in deze hogeresolutiemodellen betrouwbaar uit. De Mozambique Kanaalwervels draaien van boven gezien tegen de klok in, zijn net

zo breed als het Mozambique Kanaal (350 km) en reiken tot 1500 meter diepte of verder. Door de Corioliskracht vormen ze een bolling op het wateroppervlak van ongeveer 30 cm, die waar te nemen is met satellieten.

In observaties nemen we waar, dat de meeste wervels gevormd worden dichtbij de LOCO meetsectie. Ze worden gevormd doordat een zuidwaartse stroming die langs de Mozambiquaanse kust stroomt, instabiel wordt. Waarschijnlijk 'krult' deze stroom dan om naar het noorden en vormt er zich een ronddraaiende stroming. Een wervel zelf draagt niet veel bij aan een verandering in het transport, doordat in een wervel ongeveer evenveel water naar het zuiden stroomt als naar het noorden. Maar door de afwisseling van wervels en zuidwaartse stromingen verandert het transport wel en ontstaat er een signaal in het transport met dezelfde frequentie als die van de vorming van wervels (5 tot 6 keer per jaar). In de numerieke modellen worden de wervels meer stroomopwaarts gevormd en vervolgens meegevoerd door de meetsectie. Het transport is daardoor veel gelijkmatiger en het signaal op de werveltijdschaal veel kleiner.

Uit dit voorbeeld blijkt dat de metingen van LOCO niet alleen inzicht geven in de stroming op 17°S. We kunnen er nu ook een veel betere inschatting van maken wat de numerieke modellen goed simuleren en waar ze er compleet naast zitten. Dit is van belang, omdat er verder in de zuidwestelijke Indische Oceaan (nog) maar heel weinig metingen zijn die variabiliteit bepalen. Kennis daarover moet dus voornamelijk uit numerieke modellen komen. We hopen dat de ontwikkelaars van oceaanmodellen hun modellen kunnen verbeteren met de conclusies van dit onderzoek.

Het bestuderen van de variabiliteit in de zuidwestelijke Indische Oceaan is niet de enige reden waarom variabiliteit in de modellen goed gesimuleerd moet zijn. Soms kan variabiliteit namelijk ook de *tijdsgemiddelde* stroming beïnvloeden. Dit wordt 'rectificatie' genoemd. Men vermoedt dat in sommige modellen het gemiddelde transport door het Mozambique Kanaal afwijkt van de werkelijke waarde, doordat de modellen de variabiliteit, en dus de daardoor veroorzaakte rectificatie, niet goed kunnen simuleren. In hoofdstuk 5 wordt de invloed van rectificatie door variabiliteit gedemonstreerd. Hiervoor wordt een heel simpel model gebruikt, waarvan de situatie op die in de zuidwestelijke Indische Oceaan lijkt.

Er zijn vier soorten experimenten uitgevoerd, waarin steeds meer natuurkundige processen zijn meegenomen: wrijving, niet-lineaire circulaties en variaties in de tijd, zowel constant in de diepte als verschillend in twee horizontale lagen. Voor elk van de experimenten is het transport in het kanaal gemeten, waaruit blijkt dat het transport erg afhankelijk is van de processen die zijn gesimuleerd. Vooral de invloed van de aanwezigheid van variabiliteit in twee verschillende lagen is erg groot. Het grootste deel van de variabiliteit wordt

dichtbij het eiland gevormd en de hoeveelheid variabiliteit is hoogstwaarschijnlijk ook gerelateerd aan de hoeveelheid extra transport door het kanaal.

Het doel van dit proefschrift was de variabiliteit van het transport in het Mozambique Kanaal op verschillende tijdschalen te beschrijven. We hebben gezien dat bijna alle variabiliteit door bovenstroomse processen wordt veroorzaakt. Hiermee is een stukje van de transportband beter beschreven. Maar hieruit volgt direct ook de belangrijkste vraag voor verder onderzoek: wat gebeurt er met deze variabiliteit benedenstrooms? Oftewel: wat is de invloed van de variabiliteit in het Mozambique Kanaal op de hoeveelheid en de eigenschappen van het water dat naar de Atlantische Oceaan stroomt? In het laatste hoofdstuk van het proefschrift, hoofdstuk 6, wordt hiervoor een aantal mogelijke onderzoeksvragen en -methoden aangestipt.

Bedankt!

Gelukkig bevat elk proefschrift een plek om mensen te bedanken! Veel personen hebben namelijk direct of indirect bijgedragen aan mijn onderzoek. Op deze pagina's neem ik hier dan ook graag de gelegenheid voor.

Allereerst mijn promotoren: Will en Peter Jan. Dank jullie wel voor mijn omscholing van vloeistoffysicus-op-aquariumschaal tot oceanograaf! Het was even wennen, met die Corioliskracht en continenten, maar wel enorm interessant! Ik heb het altijd erg prettig gevonden, dat ik zomaar bij jullie binnen kon lopen met een vraag of iets niet-natuurkundigs. Peter Jan, dank je wel voor je enthousiasme! De GFD berekeningen, die we samen vaak maakten en die meestal uitliepen op enkele A4-tjes vol formules, hebben me geleerd veel sneller uit een probleem te komen. Will, door onze discussies over mijn onderzoek heb ik geleerd om me veel preciezer en logischer uit te drukken. Dank je wel!

Hoofdstuk 5 zou niet tot stand gekomen zijn zonder de hulp van Henk. Dank je wel voor je enthousiaste reactie op de resultaten, vooral als die mij wat tegenvielen!

In dit project heb ik veel samen gewerkt met de oceanografen van het NIOZ. Herman en Hendrik, bedankt voor al jullie vragen en opmerkingen over mijn onderzoek. Het merendeel ervan heeft de bewijsvoering een stuk verbeterd. Onder leiding van Herman mocht ik in maart 2006 mee op een LOCO-expeditie naar het Mozambique Kanaal. Daar hebben we de meetinstrumenten uitgelezen en hun batterijen vervangen. Herman, Graham, Mathijs, Theo en vele anderen: dank jullie wel voor het beantwoorden van mijn vele vragen over de techniek, het meten en de oceaan! Ik heb er heel veel van geleerd.

Jenny, Mathijs en Uwe, dank jullie wel voor jullie hulp met het interpoleren en filteren van de LOCO data! Jenny, ik vond het erg fijn om met je samen te werken in het onderzoek dat uiteindelijk hoofdstuk 2 is geworden.

I am in great debt to everyone who willingly shared his/her data. Many times, I have used freely available satellite data from AVISO/Cnes (SSHA) and NASA (QuikSCAT wind field). Thanks for making it available. Moreover, I have received output from many numerical models. Dr. Tony Lee, Dr. Dimitris Menemenlis and Dr. Hong Zhang (NASA Jet Propulsion Laboratory,

USA) suggested the use of the ECCO model output and made its data available. The ORCA025 was provided by Dr. Camiel Severijns from KNMI, the Netherlands. The data transfer of this model by bicycle had the direct advantage that we could discuss its usage. Dr. Arne Biastoch (IFM-GEOMAR, Germany) offered me data from his AG01-R model run. I enjoyed our discussions on the implications of the observations-model intercomparison. Dr. Andrew Coward and Dr. Beverly de Cuevas (NOC, UK) supported me in the use of the OCCAM output. I have downloaded the OCCAM data frequently, because of its easy accessibility. Thanks for that! The OFES data was given to me by Dr. Yukio Masumoto (University of Tokyo and JAMSTEC, Japan). Finally, the POP data was provided by Dr. Mathew Maltrud (LANL, USA), who sometimes had to face enormous amounts of bureaucracy due to my requests.

Het verwerken van al die gegevens was niet gelukt zonder de hulp van Marcel, Peter-Paul en Michael. Dank jullie wel voor de computerondersteuning! Yvonne, Sandra, Inge en Wanda, ook bedankt voor jullie goede zorgen!

De afgelopen vier jaar was Erik mijn vaste kamergenoot. Zonder hem was ik nooit zo snel wegwijs geraakt op deze universiteit. Daarnaast was ik erg blij met zijn uitleg over de basisbegrippen van de oceanografie en allerhande computerweetjes. Maar vooral: dank je wel voor de gezelligheid! We hebben in de afgelopen jaren liters thee weggedronken, en onze oceanografische en politieke discussies vond ik altijd erg leuk en interessant.

Het IMAU is een fijne plek om te werken. Ik voelde me er erg thuis door de prettige werkbesprekingen van de oceaangroep en de gezellige thee- en lunchpauzes. Bedankt Janneke, Leela, Selma, Jojanneke, Rianne en alle anderen! De spelletjesavonden en bioscoopbezoeken met Willem Jan, Arjen, Erik Bernsen en Guy waren altijd erg gezellig. Yvonne, je bent een super bovenbuurvrouw! Dank je wel voor je spontane acties! Mirjam, thanks for all our conversations. I have enjoyed my visits to Orlando and Kiel a lot!

En dan was er nog de aanmoediging van vrienden en familieleden. Marike, Esther, Sytse, Eric, Koos en Manda en anderen, dank jullie wel voor jullie interesse in mijn onderzoek! Rob en Marijn, ik vond het super fijn om onze promotie-ervaringen uit te wisselen. Dank jullie wel voor jullie vriendschap! Pap en Mam, jullie waren een fantastisch klankbord. Jullie waren vaak net zo blij als ik wanneer ik weer een stapje verder was. Het was ook erg fijn om met jullie over onderwijskundige trucjes te praten. Dirkjan, ik ben zo blij met jou! Je hebt me de afgelopen vier jaar vaak enorm geholpen door soms heel simpele dingen te doen. Dank je wel voor al je steun, relativeringen en energie!

Curriculum Vitae

Petra van der Werf werd op 19 mei 1981 in Zwolle geboren. Daar groeide ze ook op en volgde ze het gymnasium op het Carolus Clusius College. In 1999 vertrok ze naar Enschede om daar Technische Natuurkunde aan de Universiteit Twente te studeren. Tijdens haar studie was ze onder andere actief bij studievereniging Arago en in de onderwijscommissie en faculteitsraad. Tijdens haar stage bij de Universidade Federal do Paraná in Curitiba, Brazilië, onderzocht ze met Ernani de Lima Nascimento de gevoeligheid van convectieve stormen voor de achtergrond stratificatie. Voor haar afstudeeronderzoek bestudeerde Petra het verband tussen de snelheid en temperatuur van convectieve structuren in Rayleigh-Bénard convectie. Ze studeerde in 2005 af onder leiding van Detlef Lohse en Francisco Fontenele Araujo. Aansluitend begon ze een promotieonderzoek bij Peter Jan van Leeuwen en Will de Ruijter aan de Universiteit Utrecht naar de variabiliteit van de stroming door het Mozambique Kanaal. De resultaten van dit onderzoek zijn beschreven in dit proefschrift.

Petra van der Werf was born in Zwolle on 19 May 1981. There, she also attended the Carolus Clusius College (gymnasium). In 1999, she moved to Enschede to study Applied Physics at Twente University. Amongst others, she participated as a member of the board of study association Arago, of the educational advisory committee of Applied Physics and of the faculty council of Science and Technology. During her internship at the Universidade Federal do Paraná in Curitiba, Brazil, she studied the sensitivity of convective storms to the background environment with Ernani de Lima Nascimento. She performed her master thesis research on the correlation between the velocity and temperature of convective structures in Rayleigh-Bénard convection under supervision of Detlef Lohse and Francisco Fontenele Araujo. In 2005, she moved to Utrecht University to study the variability of the Mozambique Channel throughflow under supervision of Peter Jan van Leeuwen and Will de Ruijter. The research performed within the context of this Ph.D. project is the subject of this thesis.